Advances in Polymer Technology

Emerging Development of Sustainable Bioproducts from Renewable Natural Polymers

Lead Guest Editor: Changlei Xia
Guest Editors: Sheldon Q. Shi, Jianzhang Li, and Changtong Mei

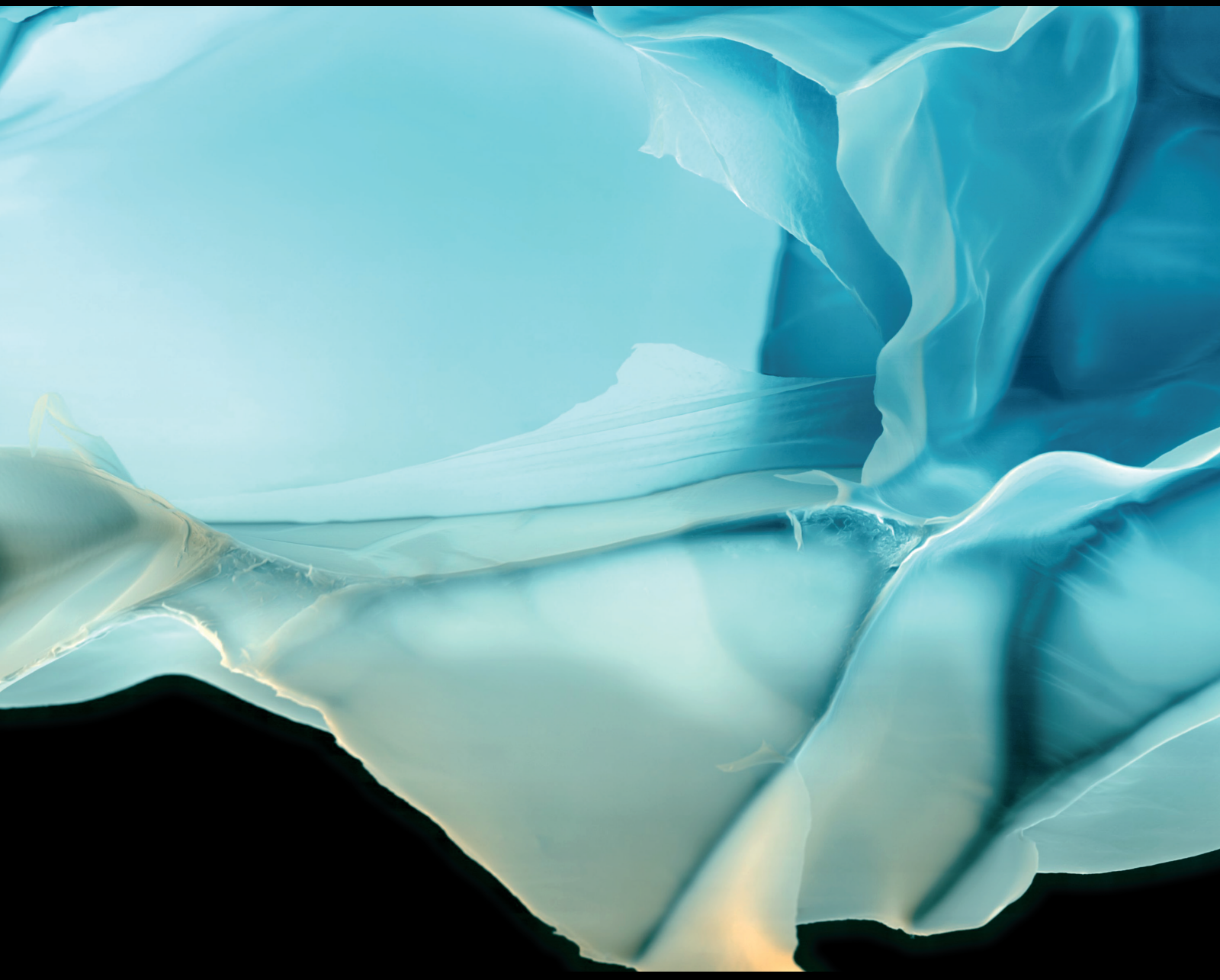

Emerging Development of Sustainable Bioproducts from Renewable Natural Polymers

Advances in Polymer Technology

Emerging Development of Sustainable Bioproducts from Renewable Natural Polymers

Lead Guest Editor: Changlei Xia
Guest Editors: Sheldon Q. Shi, Jianzhang Li, and Changtong Mei

Contents

Hindawi
Advances in Polymer Technology
Volume 2019, Article ID 6252013, 10 pages
https://doi.org/10.1155/2019/6252013

Research Article

Effects of Xylanase Pretreatment on the Quality of Refiner Mechanical Mulberry Branch Fibers

Wenjuan Tao, Lifang Guo, Aojie Meng, Lizhen Wang, Hao Ren, and Huamin Zhai

Jiangsu Provincial Key Lab of Pulp and Paper Science and Technology, Nanjing Forestry University, China

Correspondence should be addressed to Huamin Zhai; hzhai@njfu.edu.cn

Received 31 March 2019; Revised 2 June 2019; Accepted 3 July 2019; Published 15 July 2019

Academic Editor: Sheldon Q. Shi

We performed xylanase pretreatment prior to mechanical refining in the production of mulberry branch fibers, with the objective of saving energy and studying the effects of such pretreatment on the quality of the fibers. To determine the effects of the enzyme action, we analyzed the energy required for refining, related yield, and the dimension, deformation, and morphology of the fibers. We found that, with the xylanase pretreatment, the refining energy was reduced by 4%, with the yield of fibers being maintained at >85%. In addition, the fiber bundles were defibered further, resulting in reduced average length of the fiber. Furthermore, the fiber widths increased because of the improved swelling effect of the xylanase pretreatment. However, in some instances, the fine elements were reduced. With a low enzyme dosage, the fiber coarseness decreased remarkably and, because of the swelling and softening effects of the xylanase pretreatment on the mulberry branches, the fiber kink ratios and curl were reduced. Additionally, the mulberry branch tissue was loosened, facilitating fiber separation. In view of these findings, the biomechanical process could be a potentially green and efficient process for the manufacturing of mulberry branch fibers.

1. Introduction

As public awareness of the effects of economic growth and the attendant need for environmental protection increases, research interest in the utilization of renewable lignocellulosic biomass has increased [1, 2]. One such biomass species is mulberry (*Morus alba* L), which belongs to the genus *Morus* of the family Moraceae [3] that is grown widely in China, Southern Europe, North America, East Asia, Southeast Asia, and Australia [4]. A mulberry branch comprises phloem (~27%), xylem (~72%), and pith (~1%), with a density of approximately 0.49 kg/m^3 [5]. Its main chemical components are cellulose, hemicellulose, lignin, pectin, and ash [6]. As mulberry branches are one of the by-products of the silkworm industry, using these branches as a fiber resource could represent significant added value.

The xylanolytic enzyme system comprises three synergistic biological enzymes, namely, endo-β-1,4-xylanase, exo-β-1,4-xylanase, and β-xylosidase [7], which are crucial enzymes in the hydrolysis of the β-1,4-xylosidic bond of the xylan polymer backbone. Xylanase has been used in various industrial processes, including the pulp and paper industry, textile processing, biofuel industry, organic waste treatment, and the food and feed industries [8]. In the treatment of lignocellulosic biomasses, xylanase is able not only to catalyze the hydrolysis of hemicellulose but also to remove an amount of lignin by degradation of the lignin-carbohydrate complex (LCC) [9]. In addition, xylanase treatment can be considered a modification method for lignocellulosic materials, as it can modify the physical and chemical structures of such materials by degradation of xylan and, thereby, can affect their performance in various applications [10–12].

Thermomechanical pulping (TMP) is a fiber refining process whereby pulp is generated by a high-temperature high-pressure steam treatment prior to mechanical refining. Although this process is well developed and produces high yields, its energy consumption is relatively high [13]. In addition to its application in the pulp industry, TMP has been used widely in studies involving wood-plastic composites and biomass conversion, among others [14–17]. Over the past few decades, significant research efforts have focused on optimizing the TMP process to reduce energy consumption, such as chemical pretreatment, extrusion before pulping, and high-temperature refining [18]. However, challenges related to the

fiber quality and energy consumption remain. Therefore, improving the degree of fibrillation and the proportions of the long fibers is vital to improving the TMP technology [19]. As the fibrous tissue of wood is a complex biocomposite material, such issues will remain unsolved if the fibers were refined only by mechanical actions. Biopulping is the fungal or enzymatic pretreatment of wood chips for the production of mechanical or chemical pulps. It is an environmentally friendly technology that increases mill throughput substantially or reduces electrical energy consumption at the same throughput in conjunction with mechanical pulping [20]. In comparison with the widely studied degradation of wood fiber using white-rot fungi, enzymatic treatment appears to be a more rapid and efficient process [21]. Xylanase can diffuse into the interior of the fiber cell walls and act on both the fiber surface and the fiber interior [22]. The pretreatment of lignocellulosic biomass using heat- and alkali-resistant xylanase can activate and relax the fibers, which can enhance the swelling capacity and fibrillation of the fibers [23]. Consequently, the energy consumption required for pulping can be reduced and the pulp reaction performance can be improved [24–27]. As the mulberry fibers have a loose structure and high xylan content, xylanase pretreatment could be considered a promising solution to the problems mentioned [28, 29].

Fiber qualities are commonly characterized in terms of fiber length, width, coarseness, kinks, and curls. The fiber length and width are the most important indicators of fiber properties. Fiber coarseness is defined as the mass of fiber per unit length, and it is affected by the relative density, cell wall thickness, and the lumen size of the fiber. Fiber deformation is reflected by the curl and kinks in the fibers. These fiber morphology characteristics affect the softness, binding force, and water filtration performance of the fibers that, ultimately, affect the tearing strength, permeability, air permeability, and smoothness of any synthesized materials [18]. For example, when fibers are used in wood-plastic composites, fiber morphology plays a significant role in determining the properties of the composite materials [13]. Wood fibers can be subjected to physical, chemical, biological, or joint actions, which result in morphological changes that can further affect the structures and the mechanical and optical properties of the fiber products. Therefore, investigation of the effects of xylanase pretreatment on the morphological changes in mechanically refined mulberry fibers is of particular importance.

In this study, we report our investigation into the effects of xylanase pretreatment on the characteristics of refined mulberry branch fibers. More specifically, we investigate the effects of the xylanase pretreatment on the energy required for such mechanical refining, the fiber quality, and the fiber morphology in detail. The aim of the study is to determine how much energy can be saved in mechanical refining with xylanase pretreatment, as well as the effect of the enzyme pretreatment on the fiber dimension, coarseness, deformation, and morphology. We used various enzyme dosages to explore the full potential of xylanase pretreatment and we studied the changes in the fiber quality to determine the enzyme actions in the process. We expect that our findings will provide a theoretical basis for the green production of fibers from the entire stem of the mulberry branch using this combined biomechanical technique.

2. Materials and Methods

2.1. Materials. Mulberry (*Morus alba* L) tree branches were collected from Nantong City, Jiangsu Province, China. After the removal of impurities (sand, dust, and the like), the mulberry branches were cut into strips of 20–25 mm in length and 5–8 mm in width. The chemical components present in the mulberry branches are outlined in Table 1.

The xylanase (Pulpzyme HC 2500) used in our experiment was provided by Novozymes (USA). The preferred operating conditions are a temperature range of 40–60°C and a pH range of 7–9.5. At pH 8.0 (citric acid/sodium citrate buffer solution) and 50°C, the enzyme activity of xylanase was 1631 U/mL, without cellulase or laccase.

2.2. Xylanase/Disc-Refining Process for the Production of Mulberry Branch Fibers. The experimental procedure used in the study is outlined schematically in Figure 1.

2.2.1. Screw Extrusion. The wood chips were screened, immersed in tap water at approximately 25°C for 24 h, and then subjected to spiral extrusion using a roll crusher (Andritz-Bauer 6″ MSD press impregnator, Austria) at a compression ratio of 4:1. Following screw extrusion, the obtained materials were air dried at approximately 25°C prior to use.

2.2.2. Hot Water Pretreatment. The air-dried raw material (oven-dried mass = 200 g) was placed in a plastic bag and sealed. Boiled deionized water was added at a solid/liquid ratio of 1:6 (wood:deionized water). After uniform mixing, the mixture was placed in a water bath at a constant temperature of 100°C for 30 min.

2.2.3. Xylanase Pretreatment. After the thermal pretreatment, the mulberry branch samples (oven-dried mass = 200 g) were placed in a plastic bag and sealed. Deionized water was subsequently added at a solid/liquid ratio of 1:10 (wood:deionized water). The pH was adjusted to approximately 9.0 using a solution of 0.1 mol/L NaOH and, subsequently, the desired quantity of the enzyme solution was added. The resulting substance was mixed uniformly and placed in a water bath at a constant temperature of 55°C for 60 min. The bag was rubbed every 15 min to ensure uniform mixing. After this time, the mixture was dehydrated up to a dryness of ~30 wt% by using a centrifuge.

Our control samples were subjected to water pretreatment without the addition of xylanase. The remainder of the process was identical.

2.2.4. Presteaming. Presteaming was carried out in a high-pressure steam sterilizer (Shanghai Boxun Industry & Commerce Co., Ltd., China) at 125°C for 10 min.

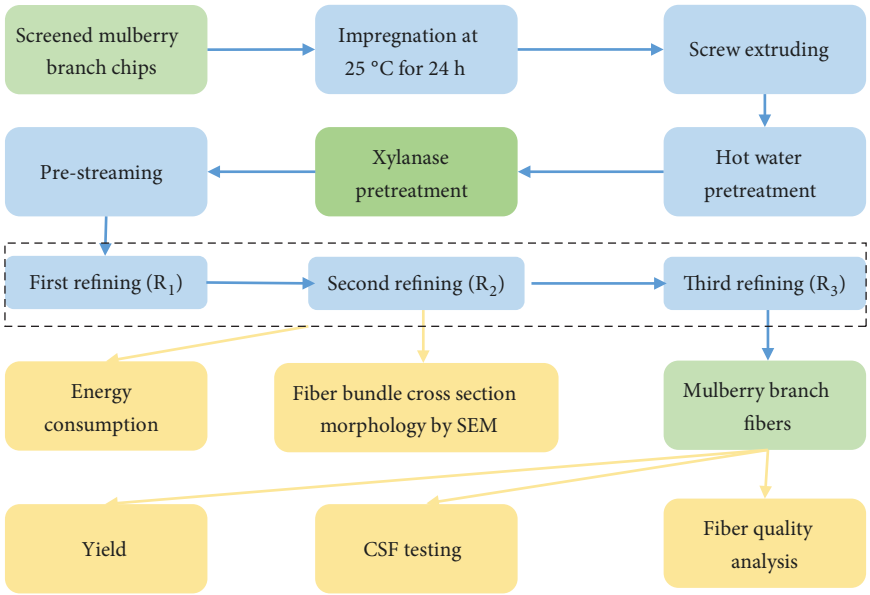

Figure 1: Experimental procedure.

2.2.5. Fiber Refining. The fiber refining process was carried out using a disc-refiner (RK85, Shaanxi Science and Technology Machinery Factory, China) at atmospheric pressure. The dry mass of each set of raw materials was 200 g. The refining process was divided into three stages. In the first (R_1) stage, the stock concentration was 25%, and the disc gap setting was 0.25 mm. In the second (R_2) stage, the concentration was 20%, and the disc gap setting was 0.15 mm, whereas in the third (R_3) stage, the concentration was 20%, and the disc gap setting was 0.15 mm.

2.3. Measurement of Energy Consumption. The precision of measuring the energy consumption during disc refining was 0.01 kW·h. The specific energy consumed for pulping was calculated using the following equation:

$$\text{Specific energy consumed for pulping}\left(\frac{\text{kW}\cdot\text{h}}{\text{t}}\right) = \frac{\text{Total energy consumed for pulping} - \text{Energy consumed during idling}}{\text{Oven dry weight of pulp stock}} \quad (1)$$

2.4. Freeness Measurements. The Canadian standard freeness (CSF) was measured using an appropriate tester (Canadian Standard Freeness Tester, P41510, PTI, Austria) according to the standard TAPPI T-227.

2.5. Fiber Quality Analysis (FQA). A sample, equivalent to an oven-dried stock weight of 40 mg, was weighed accurately, and the pulp was placed in a standard pulp disintegrator (PTI, Austria) for standardized disintegration to ensure that the interlaced fibers were freed in the pulp stock and were present as single fibers. Following pulp disintegration, the concentration was adjusted to 0.004 wt%. The samples were analyzed using a fiber quality analyzer (FQA, Morfi, THCHPAP, France), and the distributions of the fiber fines and fiber mean length, as well as the mean kink and curl indices, were calculated based on data from approximately 5 000 fibers. Fiber fines were defined as the fiber portion with a length of 70–200 μm, and the fiber length was determined over a range of 0.2–10.0 mm. The aspect ratio was calculated by the ratio of the corresponding length and width. Two measurements were performed in parallel.

2.6. Scanning Electron Microscopy (SEM). Samples of the freeze-dried fiber were embedded, sliced, and mounted on the sample stage using conductive adhesive. Prior to morphological analysis, a layer of platinum-palladium (Pt/Pd) alloy, with a thickness of 3 nm, was deposited on the surfaces of all the samples using ion sputter coating (Hitachi E-1010, Japan). The sample morphology was examined using scanning electron microscopy (SEM, FEI Quanta 200, USA) at an accelerating voltage of 25.0 kV.

3. Results and Discussions

3.1. Effect of Xylanase Pretreatment on the Pulp Yield. Mulberry branches were treated with different xylanase dosages (i.e., 0, 4, 10, and 20 U/g), and the untreated sample (i.e.,

Table 1: Chemical components in the whole stem of mulberry branch.

Components		Content (%)
Extractions		
	Benzene/alcohol	1.98 ± 0.02
	Hot water	7.44 ± 0.09
	1% NaOH	29.3 ± 0.2
Lignin		
	Klason lignin	23.5 ± 0.2
	Acid-soluble lignin	3.17 ± 0.04
	Total	26.7 ± 0.2
Holocellulose		74.9 ± 1.1
Hemicellulose		26.8 ± 0.2
Ash		2.76 ± 0.03

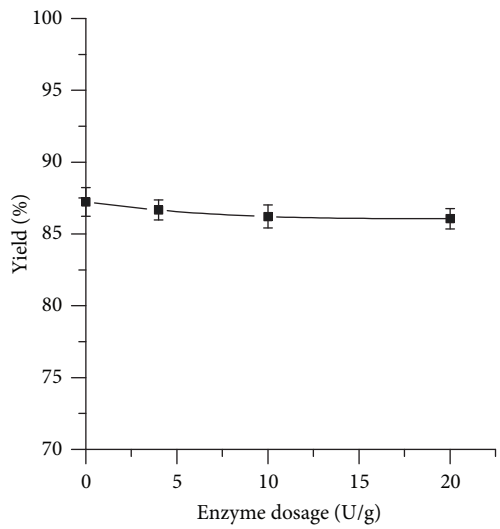

Figure 2: Effect of xylanase pretreatment on the yield of refiner mechanical fibers.

0 U/g) was used as the blank control. All other conditions were kept constant. The effect of the xylanase pretreatment on the pulp yield using whole stems of mulberry branches is shown in Figure 2. The figure indicates that increasing the enzyme dosage results in decreased pulp yield. When the enzyme dosage is 20 U/g, the pulp yield is 86.0%, which is a decrease of 1.3% compared with the control sample. The removal of xylan using xylanase results in loosened structures and increased porosity [30]. As the xylanase dosage is increased, the reaction between xylanase and xylan is promoted. The hemicellulose-carbohydrate complex (LCC) that is linked to the hemicellulose is degraded and detached by the xylanase actions. In addition, the dissolution of other components increases [24]. Therefore, all the factors result in lower yields. However, in our study, the raw materials used were mulberry branch slices with potentially limited accessible surface areas [31, 32], and, therefore, no significant decreases in yield were observed.

3.2. Effect of Xylanase Pretreatment on Energy Consumption. The dissociation of fibers by disc refining is divided generally into three steps, namely, crushing (the stock state changes from wood chips to matchstick-shaped small wood strips), rough grinding (the stock state changes from matchstick-shaped small wood strips to needle-shaped wood wire, and then further to fiber bundles and some single fibers), and fine grinding (the fibrillation of fibers) [33, 34]. In the pulping process, energy is consumed mainly in the defibering and refining processes, with the refining stage consuming the most energy. The energy consumption of the refining stage is related to the swelling and softening state of the fibers [34, 35]. The effect of the xylanase pretreatment on the energy required for the pulping of whole stems of mulberry branches is shown in Figure 3. As the enzyme dosage increases, the energy consumption decreases. For example, with an enzyme dosage of 4 U/g, the energy consumption is reduced by 3% compared with the blank control sample. The change in energy consumption is less pronounced at higher enzyme dosages. The freeness of pulp is employed commonly to evaluate the degree of fiber dissociation [36]. As shown in Figure 2, the freeness increases by increasing the xylanase dosage. At an enzyme dosage of 4 U/g, the freeness increases from 205 mL (the blank control sample) to 245 mL. This change is less noticeable at higher enzyme dosages, similar to the finding on the change in energy consumption. In fiber cell walls, hemicellulose acts as the "binder" between cellulose and lignin. As the enzyme dosage is increased, the removal of hemicellulose increases, and the structures become loose, which is favorable to defibering. Consequently, the energy required for fiber refining is reduced [36]. However, the xylanase pretreatment increases the fiber freeness, which means an increase in fiber filtration capacity. This probably resulted from the degree of fiber dissociation, the content of fine fiber, and/or the degree of fibrillation. However, as indicated in Section 3.3 (changes in fiber quality and morphology) below, the degree of fiber dissociation does not decrease, whereas the fines content does decrease. Therefore, the reduction in energy consumption is probably related to the reduction in energy consumption in the refining stage after the xylanase treatment.

3.3. Effect of Xylanase Pretreatment on Fiber Quality

3.3.1. Fiber Length, Width, and Distribution. The effect of xylanase treatment on the fiber size is shown in Figure 4. With increasing xylanase dosage, the fiber length decreases, compared with the blank sample. At an enzyme dosage of 4 U/g, the fiber length (0.44 mm in the control sample) is reduced to 0.43 mm, i.e., by 2.3%. At an enzyme dosage of 10 U/g, the fiber length is reduced to 0.40 mm, i.e., a reduction of 9.1% compared with the control. At an enzyme dosage of 20 U/g, the fiber length is 0.39 mm, i.e., a decrease of 11.4% compared with the control. As shown in the fiber length distribution pattern (Figure 5), an increase in the enzyme dosage results in a significant decrease in the portion of fiber length measuring 0.20–0.29 mm, whereas the portion measuring 0.29–0.84 mm increases significantly, and the proportion of fibers measuring >0.84 mm declines. As regards fibers with a length of >0.84 mm, including relatively long fibers and fiber bundles, the higher the enzyme dosage is the

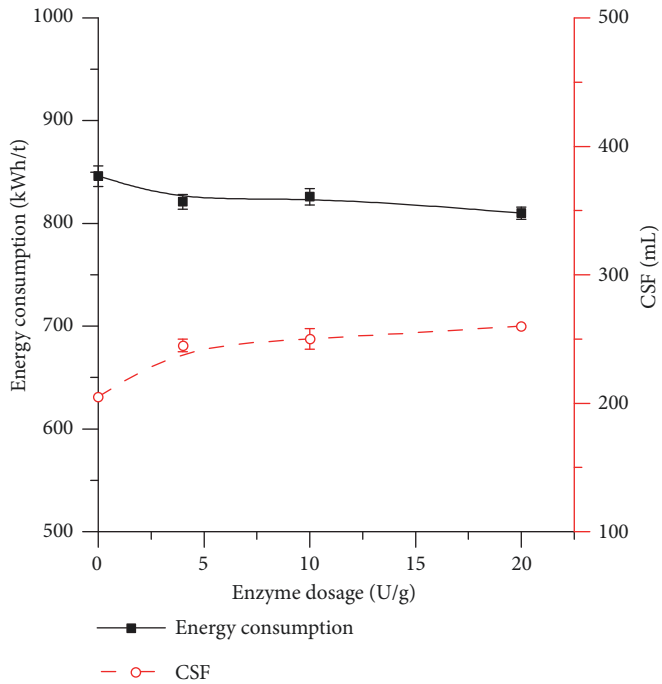

Figure 3: Effect of xylanase pretreatment on the mechanical refining of mulberry branches and the required energy consumption.

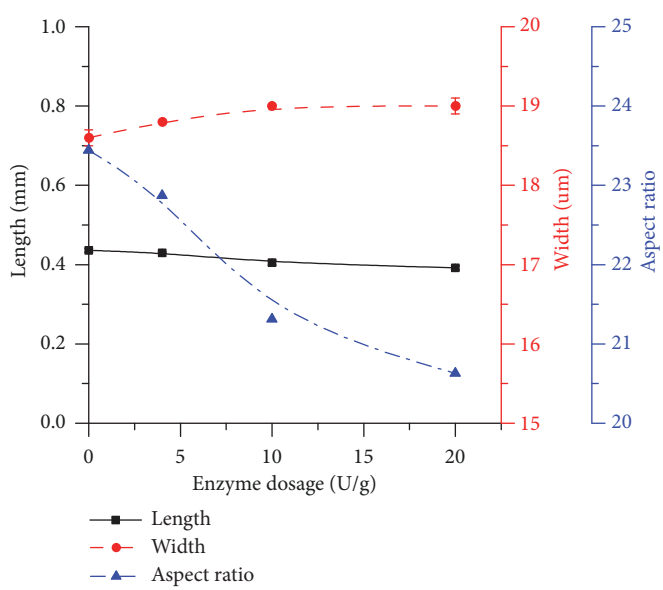

Figure 4: Effect of xylanase treatment on the length and width of refiner mechanical fibers.

lower would be the proportion of such fibers. This indicates that the xylanase treatment was beneficial to defibering and the higher the dosage is, the better would be the effect. As regards the portions of fiber measuring 0.41–0.84 mm, including single long fibers and fiber bundles, the proportion in the xylanase-treated sample increases to a certain extent compared with the control. However, it decreases with an increase in the enzyme dosage. This can be ascribed probably to the two types of changes occurring simultaneously with the xylanase pretreatment. The defibration of the longer fibers (>0.84 mm) leads to an increase in the proportion of shorter fibers (0.41–0.84 mm) and the xylanase treatment contributes to defibering this portion even further. When the enzyme dosage is higher, more bundles are defibered into single fibers, which results in a significant increase in the proportion measuring 0.29–0.41 mm. As regards the portion of fibers measuring 0.29–0.41 mm, i.e., almost single fibers, this proportion increases with the increasing enzyme dosage. However, as regards the portion measuring 0.20–0.29 mm, i.e., shorter fibers and broken fiber fragments, this proportion decreases. These results suggested that the reduction in fiber length could be ascribed to a decrease in

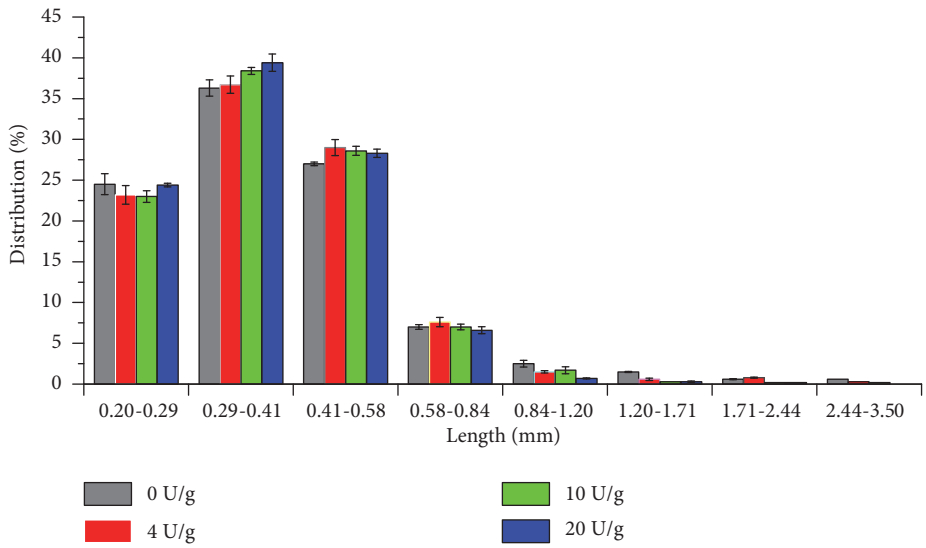

Figure 5: Effect of xylanase treatment on the length distribution of refiner mechanical fibers.

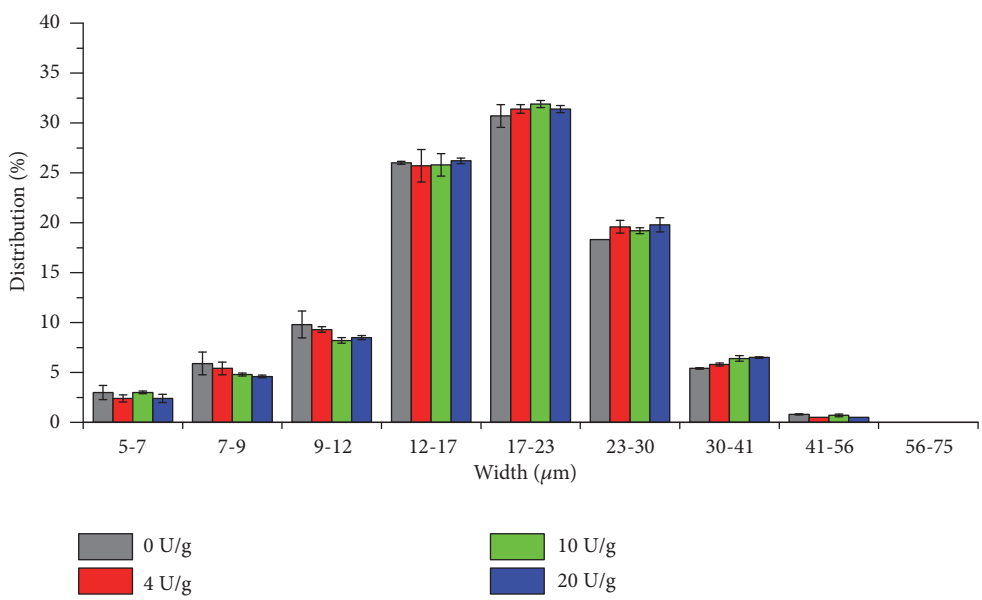

Figure 6: Effect of xylanase treatment on the width distribution of refiner mechanical fibers.

the number of fiber bundles and not to the cutting of the fibers.

The effects of the xylanase pretreatment on the average fiber widths are shown in Figure 4. With an increase in the enzyme dosage from 0 to 10 U/g, the average fiber width increases from 18.6 μm (the blank control sample) to 19.0 μm (i.e., an increase of 2.2%). When the enzyme dosage increases from 10 to 20 U/g, no significant changes in the fiber width are observed. Therefore, as shown in the fiber width distribution pattern presented in Figure 6, an increase in the enzyme dosage results in a decrease in the percentage of fiber with a width range of 5–17 μm (mainly the single fiber width range). This is attributed to the xylanase pretreatment improving the water absorption and swelling capability of the fibers. However, the percentage of the fiber width in the range 41–56 μm (i.e., the fiber bundle range) decreases, which further confirms that the enzymatic treatment facilitates the dissociation of fiber bundles. In addition, the corresponding aspect ratio decreases with the increase in the enzyme dosage because of the change in fiber length and width.

3.3.2. Fiber Coarseness. The effect of the xylanase treatment on the coarseness of the refiner mechanical fibers is shown in Figure 7. An increase in the xylanase dosage results in an initial decrease in the coarseness of the fibers, followed by a subsequent increase. When the enzyme dosage increases from 0 to 4 U/g, the fiber coarseness decreases significantly. As previously discussed in relation to Figure 3, no significant changes in the fiber length were detected under these conditions, and it was assumed, therefore, that further refining

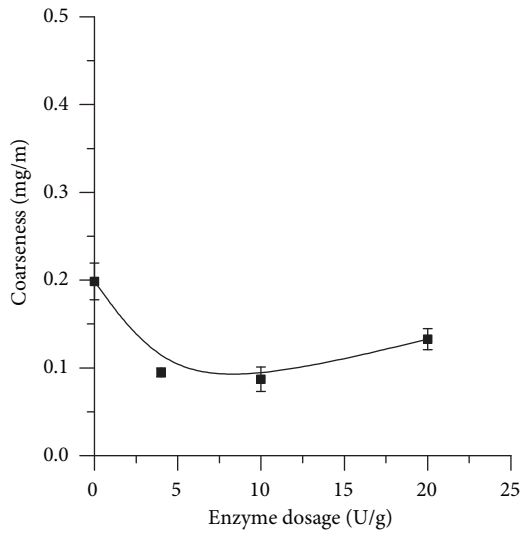

Figure 7: Effect of xylanase treatment on the coarseness of refiner mechanical fibers.

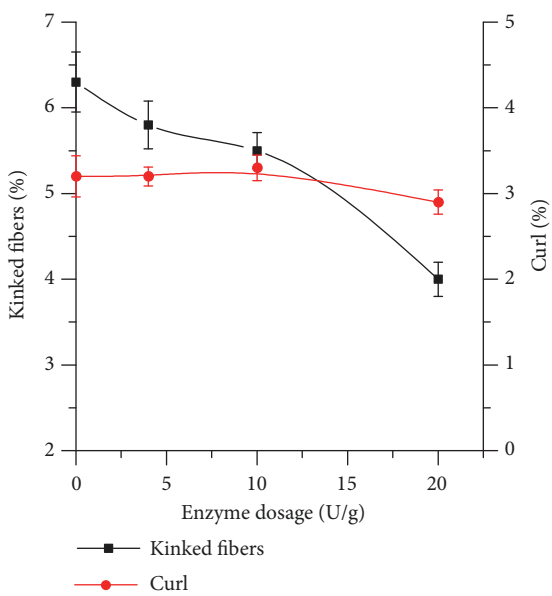

Figure 8: Effect of xylanase pretreatment on the fiber kinks and curls.

of the fiber bundles was taking place. With an increase in the enzyme dosage from 4 to 10 U/g, no significant changes in the fiber coarseness are observed, although the fiber length decreases significantly (Figure 4), suggesting further fibrillation occurring during this refining process. Furthermore, an increase in the enzyme dosage from 10 to 20 U/g results in a significant increase in the fiber coarseness, which is in agreement with the results presented in Figure 4. However, this observation seemed counterintuitive. As shown in Figure 4, the fiber length and the pulp yield do not change significantly, whereas the fiber aspect ratio decreases. It was concluded, therefore, that the fibers flocculated at this stage because of more pronounced enzymolysis at the high xylanase dosages. However, no further relevant details are available, and the issue is currently under investigation.

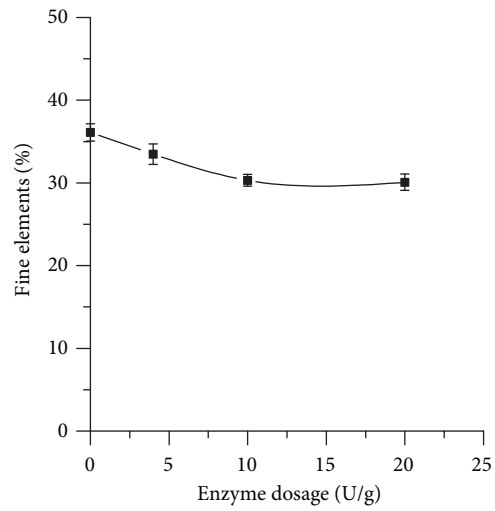

Figure 9: Effect of xylanase treatment on the fine element contents of the fibers.

3.3.3. Fiber Kinks and Curls. When fibers are subjected to stresses, such as shearing force, compressive force, friction, or distortion, deformation takes place to various degrees, which are characterized mainly as fiber curls and kinks [37]. Fiber curl refers to the gradual and continuous curvature of a fiber, whereas fiber kinks are abrupt bending changes in the fiber curvature. The observation of such fiber deformations suggests that the local ultrastructure of the fiber cell walls has been altered (i.e., in the secondary 2 layer (S_2) in the fiber wall). During the pulping process at high concentrations, the heat and twisting arising from the gear grinding process result in the fibers being subjected to high thermal and mechanical stresses, which, in turn, lead to the formation of fiber kinks and curls. The effect of xylanase treatment on the kinks and curls present in the mechanically refined fibers is shown in Figure 8. More specifically, by increasing the enzyme dosage from 0 (the control sample) to 20 U/g, the percentage of fiber curls decreases from 3.2 to 2.8%, and the percentage of kinked fibers decreases from 6.3 to 3.8%. Xylanase can diffuse through the fiber cell wall into the cell interior, thereby affecting both the fiber surface and the fiber interior [22]. Because of the degrading of hemicellulose to a certain degree, the fiber structure is loosened, which leads to improved water absorption and swelling capabilities of the fibers. Therefore, a higher enzyme dosage aids in reducing the appearance of curls and kinks in the fibers.

3.3.4. Fine Elements. A part of the fine components from the high-yield pulp was formed by the separation of the parenchyma cells and the vessel elements during pulping, while the other part, including fine fibers and microfibers, was detached from the fiber surface (length <0.2 mm, width <5 μm) [38]. Figure 9 shows the effect of the xylanase treatment on the composition percentage of fine elements. It is clear that, at an enzyme dosage of <10 U/g, the fine element contents decrease significantly. However, a plateau is reached with enzyme dosages >10 U/g. These results suggested that

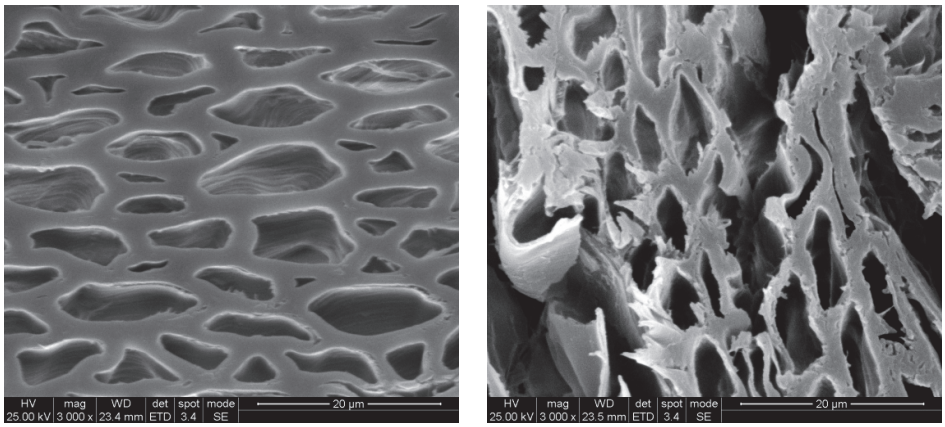

(a) (b)

Figure 10: SEM images of the cross-sectional surfaces of mulberry branch fibers without and with xylanase pretreatment. (a) Control sample (without xylanase pretreatment). (b) Sample with xylanase pretreatment (enzyme dosage, 20 U/g).

the xylanase treatment could reduce the cutting of fibers significantly.

3.4. Effect of Xylanase Pretreatment on the Fiber Cross-Sectional Morphology. SEM images of the cross-sectional surface of the materials with and without xylanase pretreatment after second-stage refining (R_2) are presented in Figure 10. As this figure indicates, when the xylanase treatment is not applied, the cross-section of the fibers shows a compacted structure without damage or cracks. However, with the xylanase treatment (Figure 10(b)), the fiber cross-section shows loosened structures, indicating that xylanase can degrade the xylan present in the mulberry branch and break the connections between xylan and lignin, thereby facilitating lignin dissolution. The result is that the fibers have loose structures, high porosity, and good swelling capability. After the xylanase treatment, the wood tissue becomes porous, which facilitates dissociation of the fibers, thereby reducing energy consumption. The xylanase treatment softened and loosened the fiber tissue, which could reduce the fiber cutting in the grinding process. Therefore, the treatment is conducive to increasing the proportion of medium and long fibers and improving the fiber quality. This finding is consistent with the results mentioned above. In addition, these observations are in agreement with those of previous studies [31].

4. Conclusion

In this study, the yield, energy consumption, fiber quality, and fiber cross-sectional changes during the mechanical refining of whole stems of mulberry branches with xylanase treatment were analyzed systematically. We found that the xylanase treatment could facilitate significant loosening of the tissues and fibers, thereby aiding defibration in the subsequent mechanical refining process. The xylanase treatment could save approximately 4% of energy at an enzyme dosage of 20 U/g in the subsequent mechanical refining process for producing fibers. The yield did change slightly and was maintained at >85%. The average fiber length was reduced after mechanical refining with the xylanase pretreatment, which was attributed to the treatment effectively decreasing the long fiber bundles. Furthermore, we found that the xylanase treatment had no effect on fiber curl, whereas the fiber kink ratio and the fine element content decreased. This method therefore represents a promising protocol for the efficient and environmentally friendly production of fibers using whole stem mulberry branches. In further study, in an effort to improve fiber quality, we will investigate the influence of different xylanase processing procedures on fiber properties.

Data Availability

The data used to support the findings of this study are included within the article.

Conflicts of Interest

The authors declare no conflicts of interest.

Acknowledgments

This research was funded by the National Natural Science Foundation of China (Grant no. 31070524) and the Major State Basic Research Development Program of China (Grant no. 2010CB732205).

References

[1] R. Kumar, S. Singh, and O. V. Singh, "Bioconversion of lignocellulosic biomass: biochemical and molecular perspectives," *Journal of Industrial Microbiology and Biotechnology*, vol. 35, no. 5, pp. 377–391, 2008.

[2] A. Zucaro, A. Fierro, and A. Forte, *A Review on Potential Candidate Lignocellulosic Feedstocks for Bio-energy Supply Chain*, Springer, Cham, Switzerland, 2019.

[3] S. Ercisli and E. Orhan, "Chemical composition of white (*Morus alba*), red (*Morus rubra*) and black (*Morus nigra*) mulberry fruits," *Food Chemistry*, vol. 103, no. 4, pp. 1380–1384, 2007.

[4] X. He, J. Fang, Y. Ruan et al., "Structures, bioactivities and future prospective of polysaccharides from Morus alba (white mulberry): A review," *Food Chemistry*, vol. 245, pp. 899–910, 2018.

[5] Z. Guo, I. Yu-Xiu, L. Lei, and Y. Fang, "A comparative study on the morphology and basic density of raw fiber in mulberry,eucommia and recycled materials," *Journal of Northwest Forestry University*, vol. 32, no. 5, pp. 202–207, 2017.

[6] R. Prithivirajan, P. Balasundar, R. Shyamkumar et al., " Characterization of cellulosic fibers from *Morus alba* L. stem ," *Journal of Natural Fibers*, vol. 16, no. 4, pp. 503–511, 2018.

[7] Q. K. Beg, M. Kapoor, L. Mahajan, and G. S. Hoondal, "Microbial xylanases and their industrial applications: a review," *Applied Microbiology and Biotechnology*, vol. 56, no. 3-4, pp. 326–338, 2001.

[8] V. Kumar, A. K. Dangi, and P. Shukla, "Engineering thermostable microbial xylanases toward its industrial applications," *Molecular Biotechnology*, vol. 60, no. 2, pp. 1–10, 2018.

[9] R. Gupta and Y. Y. Lee, "Mechanism of cellulase reaction on pure cellulosic substrates," *Biotechnology and Bioengineering*, vol. 102, no. 6, pp. 1570–1581, 2009.

[10] S. Nie, K. Zhang, X. Lin et al., "Enzymatic pretreatment for the improvement of dispersion and film properties of cellulose nanofibrils," *Carbohydrate Polymers*, vol. 181, pp. 1136–1142, 2018.

[11] S. Nie, C. Zhang, Q. Zhang et al., "Enzymatic and cold alkaline pretreatments of sugarcane bagasse pulp to produce cellulose nanofibrils using a mechanical method," *Industrial Crops and Products*, vol. 124, pp. 435–441, 2018.

[12] Y. Liu, M. Liu, H. Li, B. Li, and C. Zhang, "Characteristics of high yield pulp fibers by xylanase treatment," *Cellulose*, vol. 23, no. 5, pp. 1–9, 2016.

[13] O. Mertens, J. Gurr, A. Krause et al., "The utilization of thermomechanical pulp fibers in WPC: a review," *Journal of Applied Polymer Science*, vol. 134, no. 31, Article ID 45161, 2017.

[14] V. J. J. Prasad and P. Suresh Kumar, "A review of recent developments in natural fiber composites and their mechanical, thermal & machinabilty properties," *Advanced Materials Research*, vol. 1148, pp. 61–71, 2018.

[15] G. Cave and P. Fatehi, "Adsorption optimization of a biomass-based fly ash for treating thermomechanical pulping (TMP) pressate using definitive screening design (DSD)," *The Canadian Journal of Chemical Engineering*, vol. 96, no. 8, pp. 1663–1673, 2018.

[16] J. Park, B. Jones, B. Koo et al., "Use of mechanical refining to improve the production of low-cost sugars from lignocellulosic biomass," *Bioresource Technology*, vol. 199, pp. 59–67, 2016.

[17] R. Gonzalez, H. Jameel, H.-M. Chang, T. Treasure, A. Pirraglia, and D. Saloni, "Thermo-mechanical pulping as a pretreatment for agricultural biomass for biochemical conversion," *Bioresources*, vol. 6, no. 2, pp. 1599–1614, 2011.

[18] P. Bajpai, *Basic Overview of Pulp and Paper Manufacturing Process*, Springer, Cham, Switzerland, 2015.

[19] M. J. Sabourin and P. W. Hart, "Enhanced fiber quality of black spruce (picea mariana) thermomechanical pulp fiber through selective enzyme application," *Industrial & Engineering Chemistry Research*, vol. 49, no. 12, pp. 5945–5951, 2010.

[20] P. Bajpai, "Biotecnnology for pulp and paper processing," in *Biopulping*, Springer, Singapore, 2018.

[21] R. L. Giles, E. R. Galloway, G. D. Elliott, and M. W. Parrow, "Two-stage fungal biopulping for improved enzymatic hydrolysis of wood," *Bioresource Technology*, vol. 102, no. 17, pp. 8011–8016, 2011.

[22] S. Shuddhodana, M. N. Gupta, and V. S. Bisaria, "Stable cellulolytic enzymes and their application in hydrolysis of lignocellulosic biomass," *Biotechnology Journal*, vol. 13, no. 6, Article ID 1700633, 2018.

[23] X. Lin, Z. Wu, C. Zhang, S. Liu, and S. Nie, "Enzymatic pulping of lignocellulosic biomass," *Industrial Crops & Products*, vol. 120, pp. 16–24, 2018.

[24] A. Walia, S. Guleria, P. Mehta, A. Chauhan, and J. Parkash, "Microbial xylanases and their industrial application in pulp and paper biobleaching: a review," *3 Biotech*, vol. 7, p. 11, 2017.

[25] K. Zhang, Y. Zhang, D. Yan, C. Zhang, and S. Nie, "Enzyme-assisted mechanical production of cellulose nanofibrils: thermal stability," *Cellulose*, vol. 25, no. 9, pp. 5049–5061, 2018.

[26] S. Grönqvist, T. K. Hakala, T. Kamppuri et al., "Fibre porosity development of dissolving pulp during mechanical and enzymatic processing," *Cellulose*, vol. 21, no. 5, pp. 3667–3676, 2014.

[27] J. J. Kaschuk, T. M. Lacerda, V. Coma, and E. Frollini, "Enzymatic hydrolysis of mercerized and unmercerized sisal pulp," *Cellulose*, vol. 24, no. 6, pp. 2437–2453, 2017.

[28] K. Wong, J. Richardson, and S. Mansfield, "Enzymatic treatment of mechanical pulp fibers for improving papermaking properties," *Biotechnology Progress*, vol. 16, no. 6, pp. 1025–1029, 2000.

[29] P. W. Hart, D. M. Waite, L. Thibault et al., "Selective enzyme impregnation of chips to reduce specific refining energy in alkaline peroxide mechanical pulping," *Holzforschung*, vol. 63, no. 4, pp. 418–423, 2009.

[30] X. Lei, Y. Zhao, K. Li, and A. Pelletier, "Improved surface properties of CTMP fibers with enzymatic pretreatment of wood chips prior to refining," *Cellulose*, vol. 19, no. 6, pp. 2205–2215, 2012.

[31] K. Buzała, P. Przybysz, J. Rosicka-Kaczmarek, and H. Kalinowska, "Comparison of digestibility of wood pulps produced by the sulfate and TMP methods and woodchips of various botanical origins and sizes," *Cellulose*, vol. 22, no. 4, pp. 2737–2747, 2015.

[32] A. Pelletier, K. Li, Y. Zhao, G. Court, J. Luo, and M. Frith, "Improvement of enzyme transport in wood chips for thermomechanical pulp refining," *Carbohydrate Polymers*, vol. 95, no. 1, pp. 25–31, 2013.

[33] P. Bajpai, *Green Chemistry and Sustainability in Pulp and Paper Industry*, Springer, Cham, Switzerland, 2015.

[34] E. Cannel, "Mechanical pulping technologies focus on reducing refning energy," *Pulp & Paper*, vol. 73, no. 5, pp. 63–70, 1999.

[35] J. S. Tolan, "Enzymes, pulp and paper processing," in *Encyclopedia of Bioprocess Technology*, Wiley, New York, NY, USA, 2002.

[36] D. Fougere, K. Clarke, Y. Zhao, and K. Li, "Chemical–mechanical pretreatment of wood: reducing downsizing energy and increasing enzymatic digestibility," *Biomass & Bioenergy*, vol. 80, pp. 17–29, 2015.

[37] D. H. S. Page, R. S. Jordan, and B. D. M. C. Barbe, "Curl, crimps, kinks and micro-compressions in pulp fibers—their origin, measurements and significance. Papermaking raw materials: their interaction with the production process and their effect on paper properties," in *Proceedings of the Transactions of the 8th Fundamental Research Symposium*, pp. 183–227, Oxford, Punton, London, UK, 1985.

[38] N. H. Kamaludin, A. Ghazali, and R. W. D. Wan, "Characterisation of mechanical pulp fines from alkaline peroxide pulping of EFB," *Iranian Red Crescent Medical Journal*, vol. 1482, no. 10, pp. 296–301, 2012.

Hindawi
Advances in Polymer Technology
Volume 2019, Article ID 2723191, 10 pages
https://doi.org/10.1155/2019/2723191

Review Article

Progress of Bamboo Recombination Technology in China

Yuxiang Huang, Yue Qi, Yahui Zhang, and Wenji Yu

Research Institute of Wood Industry, Chinese Academy of Forestry, Haidian 100091, Beijing, China

Correspondence should be addressed to Yahui Zhang; zhangyhcaf@163.com

Received 15 April 2019; Accepted 2 June 2019; Published 14 July 2019

Guest Editor: Changlei Xia

At present, China is the world's largest producer of bamboo resource possessor and bamboo processing. The main processing method of bamboo recombination technology is rolling and compaction, by which a reconstituted material with bamboo fibrotic veneer as matrix and phenolic resin as reinforcement is prepared. It has excellent physical and mechanical properties and can replace high-quality wood to manufacture various engineering structural materials and building decoration materials. This paper reviewed the research process and progress of bamboo recombination technology, the existing technical problems and prospects, in order to provide references for future research on bamboo recombination theory and production practice. In recent years, as a new material with controllable properties, designable structures, and adjustable dimensions, bamboo reconstituted materials have been comprehensively studied from the aspects of pressing process parameters, physicochemical mechanical properties evaluation system, and microstructure characterization, but the research is not comprehensive and has not in-depth view. In the future, the relationship between microstructure and performance should be emphatically studied to clarify the law of mechanical performance change and ultimate mechanical performance under synergistic enhancement effect, as well as the performance change and interface formation of the resin during the entire molding process. Meanwhile, the reliability and relevance of applied research should be further expanded, and the integration of natural and artificial aging environment, process and performance, and macro- and microscales should be strengthened.

1. Introduction

Bamboo, as an important ecological, industrial, and cultural resource, has become the green and sunrise industry of modern forestry in China. At present, the output value of China's bamboo industry is 200 billion yuan, with more than 10 000 kinds of products. It plays a major role in developing green low-carbon economy, coping with climate change, achieving precise poverty alleviation, and promoting employment and income increase for farmers. With the increase of the demand for ecological products in China, the comprehensive stop of commercial logging in natural forests, and the enhancement of environmental awareness, the forestry industry will face the contradiction between the increase in market demand and the shortage of resource supply. How to fully exploit the abundant bamboo resources and make up for the shortage of high-quality timber resources has become the focus of forestry industry development and research in China.

Bamboo wood-based panel is one of the effective ways to realize the industrialization, scale, and high value utilization of bamboo. The main products include bamboo plywood [1–3], bamboo particleboard [4], bamboo fiberboard [5], bamboo glulam [6], and laminated bamboo lumber [7]. The above-mentioned boards are mainly made of bamboo strips and other basic units by planning, cutting, milling, etc. and there are a series of problems such as low utilization rate of bamboo resources, low production efficiency, and low added value. The recombination technology is mainly based on roller compaction and defibering, by which bamboo bundles or bamboo fiber mats are obtained. After the resin impregnation, parallel lay-up, the mats are hot pressed into boards or cold pressed (hot curing) into square-edged timer. This has greatly improved the utilization of raw materials and realized the structural designability and the controllability of the board properties, making the bamboo-based panels leap from the application fields of indoor floor, furniture, and cement to wind power blades with higher strength,

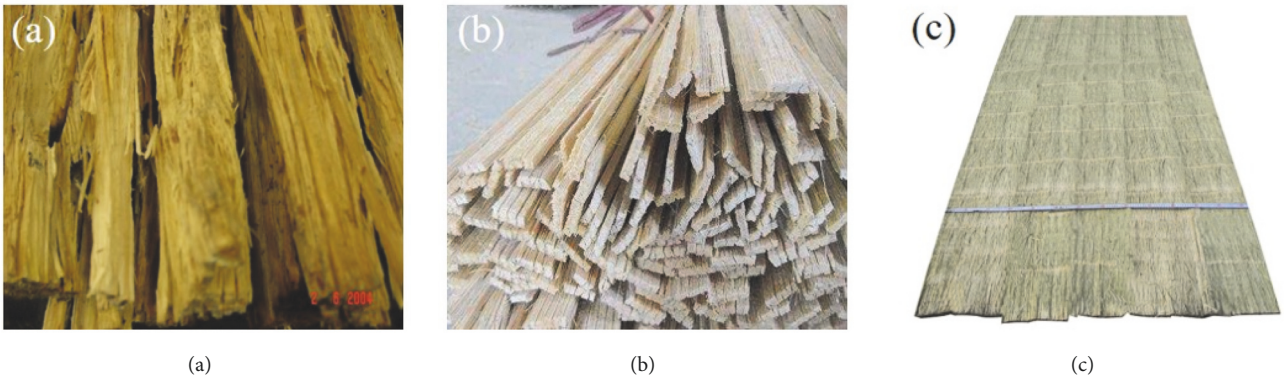

Figure 1: Research and development of bamboo scrimber unit. (a) Wood bundles for scrimber in Australia. (b) The first generation of bamboo recombination technology: bamboo bundles. (c) The second generation of bamboo recombination technology: bamboo fiber mats.

outdoor materials with high water resistance, and other high value-added fields [8]. This paper mainly introduced the research and development process of bamboo recombination technology in China, analyzed the current research status and main problems of key science and technology, and put forward some useful suggestions for the sustainable development of bamboo recombination industry and the improvement of product performance. Also, it hopes that it could serve as a reference for the theoretical research and practical application of bamboo recombination technology in the future.

2. Development Process and Research Progress of Bamboo Recombination Technology in China

2.1. Development Process of Bamboo Recombination Technology in China. The recombination technology originated in Australia. Low grade wood with small diameter, thinned wood, and brand wood were used as raw materials and processed into wood bundles by rolling. Then they were used as the basic units to develop a product similar to natural wood (Figure 1(a)). The development of recombinant technology had caused a great sensation in the world's wood-based panel industry. However, due to the inaccurate control of the recombination unit in the process of reorganization, it is difficult to effectively control the quality and realize large-scale industrialized production. The subsequent related personnel continued to study the technology of timber reorganization, but the breakthrough has not been made. Later, relevant personnel continued to study the wood recombination technology, but no breakthrough has been achieved.

At the end of 1980s, drawing on the manufacturing process and principle of wood scrimber, low quality bamboo with small diameter was used as raw materials and processed into strip-shaped bamboo bundles by rolling and flattening [9, 10]. Then they were compressed into bamboo scrimber after resin impregnation. Nevertheless, due to the tedious process, the relevant research was limited to the experimental stage. In the late 1990s, bamboo enterprises in Anji of Zhejiang first utilized waste bamboo silk from bamboo curtain processing to produce bamboo scrimber through resin impregnation and mold pressing, and the products were favored by the market. Based on the above, the bamboo strips after removing the outer part and inner part were used as raw materials by related enterprises and researchers. Strips were machined into transverse, unbroken, and longitudinal unconsolidated bamboo bundles by means of mechanical rolling (Figure 1(b)). After carbonization, resin impregnation and drying, the recombined bamboos were prepared according to the CIS slabs, hot pressing (or cold pressing), and the first generation of bamboo recombination technology was developed. The first generation of bamboo scrimber products has the characteristics of large density and beautiful pattern and is widely used in furniture, interior decoration, architecture, etc. The production enterprises were mainly distributed in Zhejiang, Fujian, Sichuan, and Anhui province. However, as for the first generation of bamboo recombination technology, the outer part and inner part of bamboo could not be utilized and the utilization rate of bamboo was only 50-60%. In addition, the inhomogeneous resin impregnation and high unit pressure requirements caused by incomplete defibering of material unit ultimately led to high production costs and the performance of bamboo scrimber cannot meet the requirements of the outdoor products [8].

In recent years, on the basis of fully summarizing the characteristics of bamboo recombination technology mentioned above, Research Institute of Wood Industry, Chinese Academy of Forestry, has completed the development of rolling and defibering technology, which integrates controllable separation of bamboo, veneer flattening, and minimally invasive treatment of the outer part and inner part of bamboo. Using this technology, the basic unit of bamboo fibrotic veneer was formed (see Figure 1(c)), which was loose and was interlaced in the longitudinally and was not broken horizontally. The technology platform of bamboo recombination was constructed (see Figure 2), and the upgrading of bamboo recombination technology was realized. Compared with the traditional bamboo basic unit such as bamboo strips and bamboo bundles, the new recombination unit has solved the technical problem of the difficult gluing of the outer part and inner part of bamboo through the destruction of the bamboo

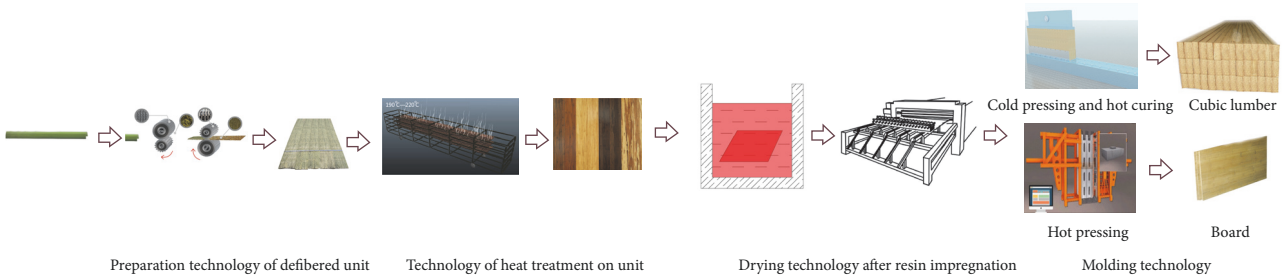

Figure 2: Process flowchart of production of bamboo scrimber.

cells and the opening of the dotted/linear crack channels. It also has broken through the problem of size limitation of bamboo processing and utilization and realized the utilization ratio of bamboo that increased from 50% to 90%. Currently, the innovative technology of bamboo recombination has been widely spread all over the country, and its products are widely used in the fields of wind power materials, outdoor materials, structural materials, and decoration materials. At present, the main market of reconstituted materials is aiming at outdoor areas, manly for parks and nature reserves. The products include outdoor pavements, railings, and garden landscapes with market capacity ranging from 500 to 700 million m^3. The technology of bamboo recombination aboard is mainly concentrated in India, Vietnam, and Myanmar in Southeast Asia, Brazil in America, and Ethiopia in Africa. Among them, India, Vietnam, and Ethiopia mainly imported the first generation of processing equipment for production of bamboo scrimber from China. In 2015, Brazil docked with the Ministry of Science and Technology of China to establish the Science and Technology Assistance Project for Developing Countries 'China Provides Bamboo Breeding and Efficient Utilization Technologies to Brazil.' Then second-generation recombination technology was introduced to Brazil for bamboo processing and utilization.

2.2. Research Progress of Bamboo Recombination Technology in China

2.2.1. Preparation Technology of Defibered Unit. The preparation technology of defibered unit mainly focuses on the defibering process and its evaluation system as well as the adaptability of bamboo species. In recent years, new research contents have emerged, such as the mechanism of defibering and separation, the morphological characteristics of the defibering unit, and the continuous and efficient unit processing. The fibrotic bamboo veneer, as the basic unit for bamboo scrimber, is prepared through the tooth cutting and transmission friction of the roller in which the bamboo unit is extruded, rubbed, and cut. At the macrolevel, a deep and shallow fissure is formed along the radial direction of the outer part and inner part of bamboo. There is a certain angle between the cracking direction and the bamboo surface, and part of the siliceous and waxy layers on the surface falls off and forms dotted or linear cracks on the surface where the extramedullary tissues fall off and are destroyed [11]. At the microlevel, the parenchyma cells fall off and are crushed and broken, the catheter wall is cut and broken, and the fiber cells are fractured and torn longitudinally and radially, of which the number of vascular bundles included in the unit sections is about 1 to 4 [12]. In terms of performance, the tensile strength of the unit decreased [13] and the surface area increased [14]. Through the preparation technology of defibered unit, the cortex that is difficult to glue falls off. The separation of fiber, vessel, and ground tissue maximally preserves the strength of bamboo fiber. The internal growth stress is released, and the permeation passage of the resin was greatly increased, which provides the foundation for the high-performance bamboo scrimber.

The morphological characteristics of the unit affect the strength of the substrate and the penetration of the adhesive, resulting in changes in the properties of the material. From the view of unit fracture morphology, the length, depth, ratio, and angle of the crack determined the effect of thinning [15]. The water absorption and the dipping amount can be used as the evaluation index [16]. Judging from the shedding of the outer part and the inner part of bamboo, the unit morphology was mainly aimed at the width of the shedding, the depth of damage, and the rate of shedding [14, 15, 17]. As seen from the morphology of the end face, the width, area, circumference, and the number of vascular bundles determined the uniformity of the unit [15, 18]. The establishment of the evaluation system of unit morphological characteristics objectively and comprehensively reflects the essential characteristics of the evaluated materials and promotes the scientific development of bamboo timber recombination technology.

The maximum width of fibrotic bamboo veneer after defibering is up to 500 mm, and its length depends on the length of bamboo. This breaks through the problem of size limitation of bamboo processing and realizes the scale industrialization utilization of clumping bamboo, *Miscellaneous* bamboo and moso bamboo [19]. At present, nearly 17 kinds of bamboo such as *Phyllostachys pubescens*, *Bambusa distegia*, *Neosinocalamus affinis*, *Phyllostachys bissetii McClure*, *Phyllostachys bambusoides f shouzhu Yi*, *Phyllostachys viridis*, *Phyllostachys glauca McClure*, *Phyllostachys praecox f. pervernalis*, *Dendrocalamus oldhamii*, *Dendrocalamus latiflorus Munro*, *Bambusa pervariabilis McClure* × *Dendrocalamus*, *Dendrocalamus sinicus*, *Dendrocalamus albonudus*, *Dendrocalamus tomentosus*, and *Bambusa burmanica Gamble* have been studied for the adaptability of bamboo unit. The differences of properties and anatomical structure of

different bamboo species ultimately affect the properties of bamboo scrimber [12, 16, 20–25]. In recent years, with the continuous maturity of industrial production technology of bamboo recombination, the technology of unit preparation and veneer lengthening provides a technical reference for the manufacture of large-span and large-size bamboo scrimber [26–28]. Usually, overlapping method is used to lengthen veneers to prepare bamboo scrimber with different specifications [29]. The technical parameters of veneer lengthening affect the mechanical properties of subsequent products. A lap length of 16.1 mm as well as a medium target density (1.01 g/cm^3) was beneficial to the improvement of mechanical properties of bamboo scrimber.

2.2.2. Technology of Heat Treatment on the Unit. The technology of heat treatment on the unit is based on hot air or overheated saturated steam as a medium to conduct high-temperature treatment of the preparation unit to improve the quality and added value of the product. The results showed that, with the increase of heat treatment temperature and the prolongation of time, the color of the unit gradually deepened, the brightness index decreased, the color difference and the mass loss increased, and the bending strength decreased at the macrolevel [29]. At the microlevel, cracks were observed in the fibrous cap, parenchyma cell wall, and intercellular layer of the unit, and the pits on the vessel wall became larger, but the morphology of the fiber cells remained unchanged [30]. In terms of chemical components, the content of alpha cellulose, hemicellulose, starch, and sugar decreased, the content of extraction and lignin increased, the pH value decreased, and the hydroxyl and hydrogen bonds of the cell surface decreased [31]. As for performance, the unit surface free energy and polarity decreased, the density, volume shrinkage, and equilibrium moisture content decreased, the hydrophobicity increased, and the elastic modulus of fibroblast and parenchyma cell wall remained unchanged, and the hardness increased significantly [32–34]. In the course of the above changes, the formation of cracks and the increase of grain size are conducive to the subsequent penetration of PF resin into the microstructure of bamboo. The decrease of the matrix material such as cellulose led to a decline in mechanical properties and the change of extract and lignin was the main reason for the color change of the unit. The decrease of starch and carbohydrate content had a positive effect on the antimildew performance of the product. The decrease of hydroxyl and hydrogen bond led to the poor hygroscopicity of the material, which benefited the improvement of the water resistance of the product. At present, the unit's heat treatment technology is built on the market demand to coordinate the temperature and time. In order to facilitate the production process of bamboo recombination technology and reduce the cost, the research on the combination of drying and heat treatment technology of bamboo has also emerged [35].

2.2.3. Drying Technology after Resin Impregnation. Reactive phenolic resin with low viscosity is used in the process of resin impregnation. After resin impregnation, the bamboo unit is dried to prepare prepreg. The prepreg is required to have two-phase matching with low content of volatile components, long storage life, appropriate viscosity, and fluidity. At present, the research on the effects of drying process after resin impregnation on the performance of products as well as the property of the resin is relatively comprehensive [36, 37]. However, few studies have been done on the characterization of the properties of adhesives during the drying process.

During the dipping process, the resin is coated with a uniform film of phenolic resin on the surface of the veneer through flow, infiltration, and wetting. At the same time, the resin adheres to or deposits on cracks formed by rolling and defibering and the cavity of parenchyma cell, as well as the cell wall of basic tissue near the crack extension [30, 38]. Impregnation capacity of the unit is achieved by the coordinated regulation of the solid content of the adhesive, the impregnation method, the impregnation time, and the water content of the unit. The solid content has a significant impact on the impregnation capacity [39–41], and the impregnation capacity is designed according to the properties and uses of the boards. At this stage, the resin used in bamboo recombination technology is mainly phenolic resin. On this basis, the impregnation properties of modified melamine resin [42] and phenolic resin/polyvinyl acetate mixed resins with different ratios [43] were studied to avoid surface cracking and improve the preloading properties of slabs.

The drying process of the impregnated unit mainly solves the problem of the moisture content brought by the adhesive in the dipping process, increases the degree of polymerization of phenolic resin, and reduces the pressing time. During the drying process, the retention value of enthalpy of resin after drying is required to be high to ensure that the adhesive has sufficient activity. If the drying temperature is too low, the final moisture content of the impregnated unit will be too high, and bubbling and other defects will occur while molding; otherwise, the precuring of adhesive will be intensified, thus affecting the bonding strength of the board [44]. It is easy to lay when the impregnated material after drying is used.

2.2.4. Molding Technology. Molding technology of bamboo is mainly composed of hot pressing and cold pressing (hot curing). In the process of molding, the microstructure, chemical composition, physical and mechanical properties of bamboo, and resin have changed significantly. The results showed that the parenchyma, vessels, and fibers of bamboo were compacted to different degrees, and the cell walls were folded or even crushed [22, 45–48]. Phenolic resin was redistributed and cured under hygrothermal condition with high pressure, forming the macrobonding interface between the resin and the substrate surface, the microscale interface between the resin and the vessel as well as the cell cavity of parenchyma cells, and the nanoscale interface between the resin and the cell wall of parenchyma cells [49]. In terms of chemical composition, hemicellulose in the cell wall was degraded, soluble extracts were further decomposed, and the relative crystallinity of cellulose was

decreased [15, 50]. Hydrogen bonds between phenolic resins and hydroxyl groups on the surface of holocellulose were formed, and hydrogen on the aromatic ring of lignin was condensed and substituted. Meanwhile, crosslinking reaction took place to form a three-dimensional network structure composed of hydrophobic groups [22, 30]. Using the cold pressing technology, the static bending strength can reach 364MPa, and the fatigue life of tension-compression can reach $3.96\times 10_6$ times (maximum loading was 90MPa). The weatherability and dimensional stability of the reconstituted bamboo have been greatly improved. For example, in the case of 28 h-boiling treatment (4 h-boiling water, 20 h-drying, and then another 4 h-boiling water), the thickness swelling rate is lower than 2.7% and the width swelling rate is less than 0.4%. In addition, the products have strong corrosion resistance.

High pressure is required in the molding process for the two methods. The difference is that the hot-pressing process is accompanied by a process of moisture and heat transfer, and the slab has a process of gradual heating and softening while the cold pressing is not. The influence of two molding processes on the properties of materials was linked to temperature, time, pressure, pressure reduction process, density, and molding type. These factors affected the rheological behavior of the resin in the process of gluing and then determined the properties of the bonding interface, which was finally manifested in the differences in the properties of the products [51–56].

2.2.5. Functionalization and Its Application Technology. Bamboo recombination technology for high-performance and multifunction products is the trend of technological progress in the industrial field. This process is based on the functionalization of materials, which will further expand the application of bamboo recombinant materials. At present, research on the preparation technology of functionalized bamboo scrimber mainly focuses on the reasonable manufacturing process, so that the product can reach the design performance, its reliability could be improved, and the cost could be reduced. Functional treatment mainly includes two methods, the treatment on bamboo (basic unit) by functional additives in the production process and postprocessing of products. The treatment of the basic unit can achieve the flame retardant and color matching function of the material. The flame-retardant function was achieved by optimizing the addition process of inorganic minerals [57] and compound flame retardant containing nitrogen, phosphorus, and boron [58–60]. Aiming at the requirements for visual and decorative properties of materials, pretreatment optimization technology on bamboo basic unit [61] and dye system screening and controllable dyeing process could improve dye-uptake and degree of fixation, which formed compounding technology system of dyeing for bamboo scrimber to achieve color regulation of bamboo scrimber. The posttreatment of the product can realize the antimildew property of the material. Physical selection of the surface of bamboo scirmber products by screening and optimizing the types and adding methods of fungicides could improve the fixation rate and antiloss ability of the antimildew agents, achieving good prevention and control effects [62–64].

The performance of the product is controllable, the structure is designable, and the dimension is adjustable via the bamboo recombination technology, which causes the product application domain to expand unceasingly. For example, bamboo scrimber products with different mechanical properties can be obtained from different bamboo species. The bamboo scrimber prepared from *Neosinocalamus affinis* bamboo has tensile strength of 119.69 MPa and tensile modulus of 24.46 Gpa. Its flexural strength and modulus are 151 MPa and 23.4 GPa, respectively. Also, it has a high shear strength of 37.33 MPa [65]. These properties are sufficient to make it suitable for structure applications. In the field of architectural structure, the related research focuses on the analysis of mechanical properties of bamboo scrimber under different environmental temperature and humidity conditions [66–69]. The mechanical properties [70–76] and creep properties [77] were characterized. The performance design [78–82] and the mechanical characteristics of connection joints [83–85] were also investigated to optimize the design method of enhanced bamboo scirmber components [86–88]. The above research is expected to provide scientific basis for rational utilization of bamboo scrimber in the field of building structure. In the field of outdoor weathering, the changes of properties of bamboo scrimber under different aging treatments [89–94] were mainly discussed. The decay resistance of bamboo scrimber [47] was also studied, and its reliability was predicted and evaluated to realize the scientific protection and application of bamboo scrimber in outdoor products [95]. In the field of indoor decoration, the finishing technology [96, 97] and corrugated lightweight design [98] were studied to improve the decorative performance of materials. In addition, the environmental protection performance [99] and secondary processing performance [100, 101] of bamboo scrimber were investigated to promote the diversification and serialization of products. According to the above research, bamboo scrimber materials have been expanded from indoor floor, furniture [102], and cement template to wind power blade [103], building structure [104], and outdoor materials [105].

3. The Technical Problems to Be Solved in China's Bamboo Recombination Technology

Although bamboo recombination technology has made breakthrough progress, as a new technology, there are relatively few basic research and applied basic research on bamboo scrimber, which limits the development of new products based on this material. Therefore, it is necessary to further summarize and refine the related technical problems related to bamboo recombination technology and systematically study bamboo recombination technology by referring to the advanced theories and research methods of traditional composite materials, so as to further promote the popularization and application of this material.

3.1. Preparation Technology of Defibered Unit. The preparation technology of defibered unit breaks through the bottleneck of bamboo veneer utilization and improves the production efficiency of bamboo by 5 times compared with bamboo strips. At present, equipment for defibering bamboo has basically achieved mechanization, but it is urgent to upgrade the continuity and automation level of existing equipment and achieve the precise control of the equipment. Meanwhile, the problems of unit adaptability for continuous, highly efficient, and automatic production during the preparation of defibered units need further research and discussion.

3.2. Technology of Heat Treatment on the Unit. Currently, the technology of heat treatment on the unit is used as a green physical modification method to improve the color and dimensional stability of products. However, the increase of heat treatment temperature and the extension of time will cause the decline of mechanical properties of the unit and greatly aggravate the loss of materials. Thus, firstly, it is necessary to explore the mechanism of strength chemical change and its effect on material properties under heat treatment and to reveal the influence of related components on bonding interface and resin permeability after heat treatment. Finally, the controllable heat treatment technology system of material unit is formed. The analysis and solution of the above problems will play a great role in guiding the adjustment of preparation technology for bamboo scrimber and the development of functional products.

3.3. Drying Technology after Resin Impregnation. Phenolic resin is invoked as the reinforcing phase in bamboo recombination technology. By controlling its content, the performance of the material can be enhanced. During the impregnation process, the bonding interface formed between phenolic resin and bamboo basic unit has a great influence on the subsequent process and properties of the material. At this stage, there is still a need to concentrate on the following aspects: (1) qualitative and quantitative analysis of the soaking rate, uniformity and degree of impregnation of resin in the substrate, and the response mechanism of the final product properties to the degree of impregnation in the impregnation process; (2) quantitative characterization of changes in physical and chemical properties of resins such as molecular weight, active groups and aggregates in drying process, and effects of resin precuring on processing, manufacturing, and final product properties; (3) the influence of moisture content of prepreg after drying on the performance of the final product; (4) developing low temperature and fast drying equipment and technology to improve the quality and efficiency of drying process and reduce the cost.

3.4. Molding Technology. The molding technology belongs to liquid forming technology for adhesive. In this process, the adhesive goes through a physical process characterized by flow and a chemical process characterized by reaction. The two subprocesses coexist and interact. The adhesive changes from low viscosity liquid resin to a solid material, forming the bonding interface, which has a great influence on the properties of the material. During the two forming processes, the flow and long-distance infiltration of resin will become ever more difficult. The rediffusion permeation of resin and the similarities and differences of flow path paths in substrates by short-range flow have yet to be studied. Secondly, prepreg at this stage needs to carry out manual laying process. Automated paving equipment and technology are required to improve production efficiency and reduce cost. At last, it is desired to develop a new adhesive to realize low-temperature curing process, and at the same time digital simulation of curing forming process needs to be carried out to guarantee product quality.

The basic units are densified during the molding process, which greatly improves the mechanical properties of the final product. The synergistic enhancement effects of unit preparation, dipping amount, and density contribute to this improvement. However, this synergistic effect is not a simple linear relationship, and the difference of bamboo species has a significant influence on the mechanical properties. For specific materials, the ultimate crushing value varies according to different molding processes. The correlativity between the microstructure and mechanical properties during the forming process and the variation of mechanical properties and ultimate mechanical properties of bamboo scrimber prepared from different bamboo species under the condition of synergistic reinforcement deserve further discussion and explanation.

3.5. Application Technology. As a newly developed biobased composite material, the durability of bamboo scrimber is one of the technical indexes for the long-term preservation of its performance in the process of use and storage, which has attracted more and more attention. Although aging properties of bamboo reconstituted materials have been explored at the present stage, there is a lack of research on the microstructure and properties of bamboo under the synergistic effect of radiation, moisture, and heat. There is still a certain distance to study the mechanism of climatic aging and the prediction methods of natural aging life based on the law of artificial accelerated aging are still lacking, which are very important to evaluate the reliability of bamboo scrimber.

Furthermore, as a novel material, the standardization system of this product is still imperfect, especially the lack of standards in the field of product structure, which limits its application in wood structure building. It is necessary to establish and optimize the evaluation method and system of bamboo recombinant materials as soon as possible so as to standardize and lead the healthy and rapid development of the industry. In addition to the above-mentioned technical issues, other issues such as flame retardant, antimildew, anticorrosion mechanism, surface properties of recombinant materials, and its response mechanism to finishing process need further research and exploration, in order to better promote its technical progress and industry development.

4. Conclusion

Bamboo recombination technology is an effective means for highly efficient and high value utilization of bamboo. In the process of production, both technology and equipment have independent intellectual property rights, which provides strong scientific and technological support for improving the quality and efficiency of bamboo processing industry in China. Also, it is at the international leading level in similar research. With the development of biomass building materials and bamboo structure in China, bamboo recombination technology will enter a period of rapid development.

Conflicts of Interest

The authors declare that they have no conflicts of interest.

Acknowledgments

This work was financially supported by Special Funds for Basic Research and Operating Expenses of Central Level Public Welfare Scientific Research Institutes (CAFYBB2017QA015), Science and Technology Planning Project of Guangdong Province, China (2016B020203002), and Forestry Science and Technology Innovation Project of Guangdong Province, China (2015KJCX031).

References

[1] W. J. Yu, "Studies on weaving methods and hot-press techniques for bamboo weaving board," *China Wood Industry*, vol. 6, no. 4, pp. 5–12, 1992.

[2] Q. Zhang, "New progress of bamboo plywood," *China Timber Journal*, vol. 1, pp. 21–23, 1993.

[3] R. Zhao, "Technological innovation and development direction of bamboo curtain plywood," *China Wood-Based Panels*, vol. 5, pp. 8–11, 2003.

[4] H. Zhang, F. Zhang, Z. Liao, X. Li, G. Li, and Z. Yang, "Research development and application of the technology for industrial production of bamboo waferboard," *China Wood-based Panels*, vol. 14, no. 8, pp. 30–33, 2007.

[5] X. Song, Z. Ye, Y. Ye, X. Liu, and P. Shi, "Study on the application of several kinds of Fujian bamboo in fiberboard industry," *Wood Processing Machinery*, vol. 3, pp. 3–7, 2007.

[6] Z. Jiang, L. Chang, Z. Wang, and L. Gao, "Physical and mechanical properties of glued structural laminated bamboo," *China Wood Industry*, vol. 4, pp. 22–24, 2005.

[7] F. Fu, "Technology and properties of bamboo curtain laminated timber," *Forest Science and Technology*, vol. 4, pp. 6–9, 1999.

[8] W. Yu, "Development of bamboo-fiber based composites," *China Wood Industry*, vol. 25, no. 1, pp. 5–8, 2011.

[9] S. Wang, "Preliminary study on reconstituted bamboo boards," *Building Particle Board*, no. 2, pp. 22–27, 1990.

[10] L. Ye, Z. Jiang, J. Ye, and J. Meng, "Study on reconstituted bamboo bamboo," *Journal of Zhejiang A & F University*, no. 2, pp. 133–140, 1991.

[11] Y. Zhang, F. Meng, and W. Yu, "Crushing effectiveness on properties of crushed bamboo-mat composites," *China Wood Industry*, vol. 26, no. 5, pp. 6–8, 2011.

[12] J. Qi, *Evaluation of the Performances of Bamboo Based Fiber Composites Based on the Characteristics of Vascular Bundle and Fiber*, Chinese Academy of Forestry, 2013.

[13] W. Zhang, *Mechanical Properties and Brooming Processing of Bamboo-Culm*, Chinese Academy Forestry, 2012.

[14] X. Yu and W. Yu, "Performance research on crushed bamboo veneer for Bambusa distegia," *Journal of Northeast Forestry University*, vol. 41, no. 2, pp. 74–76, 2013.

[15] J. Qi, W. Yu, J. Xie, Y. Yu, Y. Zhang, and H. Sun, "Morphologies of crushed bamboo veneer used for bamboo-based fiber composites," *China Wood Industry*, vol. 26, no. 2, pp. 6–9, 2012.

[16] F. Meng, *Manufacturing Technology and Properties of Scrimber of Bamboo Fibrillated-Veneer Lumber*, Northeast Forestry University, 2011.

[17] Y. Yu, *Manufacturing Technology and Mechanism of High Performance Bamboo-Based Fiber Composites*, Chinese Academy Forestry, 2014.

[18] Y. Zhang, F. Meng, and W. Yu, "Study on performance of bamboo-based fiber composites prepared with Phyllostachys bissetii McClure and Phyllostachys bambusoides fshouzhu Yi," *China Wood-Based Panels*, vol. 1, pp. 13–16, 2013.

[19] W. Yu and Y. Yu, "Development and prospect of wood and bamboo scrimber industry in China," *China Wood Industry*, vol. 27, no. 1, pp. 5–8, 2013.

[20] W. Yu, Y. Yu, Y. Zhou, and D. Ren, "Studies on factors influencing properties of reconstituted engineering timber made from small-sized bamboo," *China Forest Products Industry*, vol. 33, no. 6, pp. 24–28, 2006.

[21] L. Cheng, *Manufacturing Technology of Reconstituted Bamboo Lumber*, Inner Mongolia Agricultural University, 2009.

[22] Y.-L. Yu, X.-A. Huang, and W.-J. Yu, "High performance of bamboo-based fiber composites from long bamboo fiber bundles and phenolic resins," *Journal of Applied Polymer Science*, vol. 131, no. 12, Article ID 40371, 2014.

[23] Y. Zhang and W. Yu, "Preliminary study on the properties of Dendrocalamus latiflorus Munro bamboo-fiber based composites," *China Wood Industry*, vol. 43, no. 4, pp. 16–18, 2016.

[24] J. Qi, J. Xie, W. Yu, and S. Chen, "Effects of characteristic inhomogeneity of bamboo culm nodes on mechanical properties of bamboo fiber reinforced composite," *Journal of Forestry Research*, vol. 26, no. 4, pp. 1057–1060, 2015.

[25] J. Xie, J. Qi, T. Hu, C. F. De Hoop, C. Y. Hse, and T. F. Shupe, "Effect of fabricated density and bamboo species on physical–mechanical properties of bamboo fiber bundle reinforced composites," *Journal of Materials Science*, vol. 51, no. 16, pp. 7480–7490, 2016.

[26] Y. Qiu, *The Properties on Bamboo Bundle Veneer and Bamboo-Bundle Laminated Veneer Lumber*, Chinese Academy of Forestry, 2013.

[27] F. Chen, *Technology and Theory of Bamboo Bundle Laminated Veneer Lumber with Continuous Plate Process*, Chinese Academy of Forestry, 2014.

[28] W. He, J. Song, T. Wang et al., "Effect of heat oil treatment on bamboo scrimber properties," *China Forestry Science and Technology*, vol. 2, no. 5, pp. 15–19, 2017.

[29] Y. Zhang, W. Yu, and Y. Zhang, "Effect of steam heating on the color and chemical properties of neosinocalamus affinis bamboo," *Journal of Wood Chemistry and Technology*, vol. 33, no. 4, pp. 235–246, 2013.

[30] F. Meng, R. Liu, Y. Zhang, Y. Huang, Y. Yu, and W. Yu, "Improvement of the water repellency, dimensional stability,

and biological resistance of bamboo-based fiber reinforced composites," *Polymer Composites*, 2017.

[31] L. Qin, *Effect of Thermo-Treatment on Physical, Mechanical Properties and Durability of Reconstituted Bamboo Lumber*, Academy of Chinese Forestry, 2010.

[32] R. Salim, Z. Ashaari, H. Samsi, R. Wahab, and R. H. Alamjuri, "Effect of oil heat treatment on physical properties of semantan bamboo (Gigantochloa scortechinii Gamble)," *Journal of Sustainable Development*, vol. 1, no. 2, pp. 107–113, 2009.

[33] Y. Zhang and W. Yu, "Changes in surface properties of heat-treated phyllostachys pubescens bamboo," *Bioresources*, vol. 10, no. 4, pp. 6809–6818, 2015.

[34] F. Meng, Y. Yu, Y. Zhang, W. Yu, and J. Gao, "Surface chemical composition analysis of heat-treated bamboo," *Applied Surface Science*, vol. 371, pp. 383–390, 2016.

[35] R. Sun, *The Study on the Integration Technology about High Temperature Drying and Thermal Treatment of Bamboo*, Central South University of Forestry and Technology, 2013.

[36] C. Wang, L. Zhao, H. Liu, C. Zhang, and J. Zhang, "Synthesis and characterization of phenolic resin for bamboo impregnation," *Forestry Machinery & Woodworking Equipment*, vol. 8, pp. 14–16, 2012.

[37] J. Zhang, Q. Li, S. Yuan, Z. Wang, H. Yu, and H. Wang, "Study on permeability of phenol-formaldehyde resin for reconstituted bamboo lumber," *Forestry Machinery & Woodworking Equipment*, vol. 2, pp. 22–25, 2015.

[38] Y. Yu, R. Liu, Y. Huang, F. Meng, and W. Yu, "Preparation, physical, mechanical, and interfacial morphological properties of engineered bamboo scrimber," *Construction and Building Materials*, vol. 157, pp. 1032–1039, 2017.

[39] L. Cheng, X. Wang, and Y. Yu, "Effect of glue immersion parameters on performance of reconstituted dendrocalamopsis oldhami lumber," *China Wood Industry*, vol. 23, no. 3, pp. 16–19, 2009.

[40] F. Meng, Y. Yu, R. Zhu, Y. Zhang, and W. Yu, "Effect of resin impregnation rate on physical and mechanical properties of laminated bamboo fibrillated-veneer lumber," *China Wood Industry*, vol. 25, no. 2, pp. 1–3, 2011.

[41] Y. Wang, J. Lv, X. Li, K. Xu, and Y. Wu, "Optimization adhesive impregnation conditions of bamboo bundles used for making reconsolidated bamboo composite," *Journal of Central South University of Forestry & Technology*, vol. 33, no. 10, pp. 153–157, 2013.

[42] Y. Zhou, Y. Chen, Z. Wu, N. Li, and J. Yuan, "Influence of modified MF resin on surface crack of reconsitituted bamboo," *China Forest Products Industry*, vol. 5, pp. 26–29, 2013.

[43] D. Zhang, *Processing Technology of Overlength Bamboo-Bundle Laminated Veneer Lumber and Its Porformance*, Chinese Academy of Forestry, 2014.

[44] Y. Zhang, R. Zhu, W. Yu, and J. Qi, "Glue-impregnated bamboo-mat drying temperature effect on crushed bamboo-mat composite properties," *China Wood Industry*, vol. 25, no. 6, pp. 1–3, 2011.

[45] J. Qi, W. Yu, X. Huang, S. Chen, and B. Wu, "Effect of bamboo scrimber density on vascular bundle morphology and properties," *China Wood Industry*, vol. 27, no. 6, pp. 25–28, 2013.

[46] Y. Yu, X. Huang, and W. Yu, "A novel process to improve yield and mechanical performance of bamboo fiber reinforced composite via mechanical treatments," *Composites Part B: Engineering*, vol. 56, pp. 48–53, 2014.

[47] A. Kumar, P. Ryparovà, B. Kasal, S. Adamopoulos, and P. Hajek, "Resistance of bamboo scrimber against white-rot and brown-rot fungi," *Wood Material Science and Engineering*, pp. 1–7, 2018.

[48] F. Rao, Y. Chen, N. Li et al., "Preparation and characterization of outdoor bamboo-fiber-reinforced composites with different densities," *Bioresources*, vol. 12, no. 3, pp. 6789–6811, 2017.

[49] Y. Yu, Y. Huang, Y. Zhang, R. Liu, F. Meng, and W. Yu, "The reinforcing mechanism of mechanical properties of bamboo fiber bundle-reinforced composites," *Polymer Composites*, vol. 40, no. 4, pp. 1463–1472, 2018.

[50] L. Hou, Q. Zhang, T. Su, and J. Lu, "X-ray photoelectron spectroscopy analysis of reconstituted bamboo lumber," *Journal of Forestry Engineering*, vol. 26, no. 1, pp. 47–49, 2012.

[51] R. X. Zhu and W. J. Yu, "Effect of density on physical and mechanical properties of reconstituted small-sized bamboo fibrous sheet composite," *Advanced Materials Research*, vol. 150-151, pp. 634–639, 2010.

[52] R. Zhu, Y. Zhou, D. Ren, Y. Yu, and W. Yu, "Effect of manufacturing methods on bamboo-fiber based composite performance," *China Wood Industry*, vol. 3, pp. 1–3, 2011.

[53] Q. Li, M. Yang, L. Chen, and H. Zhang, "Effect of technological parameter on performance of recombined bamboo materials," *Journal of Fujian College of Forestry*, vol. 31, no. 2, pp. 189–192, 2011.

[54] C. Wang, L. Cui, H. Liu, J. Zhang, and C. Zhang, "Study on cold press technology for reconsolidated bamboo," *Forestry Machinery & Woodworking Equipment*, vol. 41, no. 12, pp. 17–19, 2013.

[55] Y. Mao, D. Hou, and X. Yu, "Effect of decreased pressure on the properties of reconstituted bamboo lumber," *Journal of Forest and Environment*, vol. 35, no. 2, pp. 175–178, 2015.

[56] Y. Zuo, Y. Wu, J. Xiao, X. Li, and K. Long, "Hot pressing process of recombinant bamboo based on response surface methodology," *Journal of Functional Materials*, vol. 47, no. 11, pp. 11196–11200, 2016.

[57] W. Chen, X. Li, G. Yuan, Y. Ji, M. Chen, and B. Fu, "Preparation and characterization of flame retardant bamboo-wood hybrid scrimber," *New Chemical Materials*, vol. 43, no. 8, pp. 93–95, 2015.

[58] S. Liu, *Preparation and Performance of Fire Retardant Bamboo-Based Composites*, Chinese Academy of Forestry, 2013.

[59] R. Li, *Preparation and Combustion Characteristic of Flame Retardant Reconstituted Bamboo*, Zhejiang A & F University, 2014.

[60] X. Jin, L. Zhang, Y. Li, X. Wen, and D. Qin, "Effects of three fame retardants on combustion physical and mechanical properties of bamboo scrimber," *Journal of Northwest Forestry University*, vol. 30, no. 5, pp. 214–218, 2015.

[61] C. Wang, *The Research on the Staining Characteristics and Technology of the Bamboo Bundles with Reactive Dyes*, Central South University of Forestry and Technology, 2015.

[62] H. Du, F. Sun, and S. Jiang, "Anti-mold performance of strand woven sympodial bamboo," *Journal of Zhejiang A&F University*, vol. 1, pp. 95–99, 2013.

[63] J. Zhang, S. Yuan, H. Fan, Q. Li, and H. Wang, "Effect of different antimildew and antiseptic agents on reconstructed bamboo timber," *Journal of Zhejiang Forestry Science and Technology*, vol. 36, no. 5, pp. 8–12, 2016.

[64] X. Zhang, J. Xu, S. Jiang, Y. Zhu, and D. Hu, "Simulation of the outdoor anti-mold performance of the recombinant bamboo," *Journal of Bamboo and Rattan*, vol. 35, pp. 8–12, 2016.

[65] W. Shangguan, *Research on Physical and Mechanical Properties of Bamboo Scrimber*, Chinese Academy Forestry, 2015.

[66] Z. Yu, *Processing Technology of Laminated Bamboo-Bundle Veneer Lumber and Its Application Performance*, Chinese Academy Forestry, 2012.

[67] W. Shangguan, Y. Gong, R. Zhao, and H. Ren, "Effects of heat treatment on the properties of bamboo scrimber," *Journal of Wood Science*, vol. 62, no. 5, pp. 383–391, 2016.

[68] Y. Zhong, H. Ren, and Z. Jiang, "Effects of temperature on the compressive strength parallel to the grain of bamboo scrimber," *Materials*, vol. 9, article 436, 2016.

[69] Z. Cui, F. Wang, M. Xu, and Z. Chen, "Experimental study on embedding strength of bamboo scrimber parallel to grain at high temperatures," *Journal of Southeast University (Natural Science Edition)*, vol. 47, no. 6, pp. 1174–1179, 2017.

[70] J. Zhang, H. Ren, Y. Zhong, and R. Zhao, "Analysis of compressive and tensile mechanical properties of recombinant bamboo," *Journal of Nanjing Forestry University (Natural Science Edition)*, vol. 4, pp. 107–111, 2012.

[71] W. Shangguan, Y. Zhong, X. Xing, R. Zhao, and H. Ren, "Strength models of bamboo scrimber for compressive properties," *Journal of Wood Science*, vol. 61, no. 2, pp. 120–127, 2015.

[72] X. Li, M. Yu, Y. Cai, H. Ren, and Y. Zhong, "Determination of elastic constants of recombinant bamboo for structural material using an electrical measurement method," *Journal of Anhui Agricultural University*, vol. 5, pp. 756–760, 2015.

[73] B. Sharma, A. Gatóo, M. Bock, and M. Ramage, "Engineered bamboo for structural applications," *Construction and Building Materials*, vol. 81, pp. 66–73, 2015.

[74] X. Liu, *Study on Damage and Fracture Behavior of Bamboo Scrimber*, Chongqing Jiaotong University, 2016.

[75] W. Pan, *Experimental Study and Numerical Simulation of Bamboo Scrimber Type II Fracture*, Nanjing Forestry Univeristy, 2017.

[76] Y. Wei, X. Ji, M. Duan, L. Zhao, and G. Li, "Model for axial stress-strain relationship of bamboo scrimber," *Acta Materiae Compositae Sinica*, vol. 35, no. 3, pp. 572–579, 2018.

[77] B. Wu, *Test and Analysis of Creep Performance of Bamboo Scrimber*, Northeast Forestry University, 2015.

[78] J. Su, F. Wu, H. Li, and P. Yang, "Experimental research on parallel bamboo strand lumber column under axial compression," *China Science Paper*, vol. 1, pp. 39–41, 2015.

[79] Y. Wei, M. Zhou, and L. Yuan, "Mechanical performance of glulam bamboo columns under eccentric loading," *Acta Materiae Compositae Sinica*, vol. 33, no. 2, pp. 379–385, 2016.

[80] S. Zhang, Z. Zhao, W. Zhang, Y. Shi, and N. Zhu, "Research on the flexural performance of bamboo scrimber," *Journal of Yangzhou University(Natural Science Edition)*, vol. 19, no. 1, pp. 51–54, 2016.

[81] S. Zhang, C. Li, Z. Xiao, and N. Zhu, "Bending strength and loading simulation analysis of bamboo scrimber I-shaped beam," *Journal of Forestry Engineering*, vol. 2, no. 1, pp. 125–129, 2017.

[82] J. Zhou and Y. Shen, "Numerical analysis of the flexural bearing capacity for the parallel strand bamboo beams," *China Science Paper*, vol. 1, pp. 83–86, 2018.

[83] X. Li, *Study on Load Carrying Capacity of Bamboo Scrimber Bolted Joints*, Chinese Academy of Forestry, 2013.

[84] A. Zhou, D. Huang, S. Tang, and S. Zhao, "Experimental research on bearing capacity of the bolted PSB-steel-PSB joints," *Journal of Nanjing University of Technology (Natural Science Edition)*, vol. 5, pp. 34–39, 2016.

[85] J. Zhou, D. Huang, and Y. Shen, "Experiment investigation on dowel-bearing strength perpendicular to grain of parallel strand bamboo," *Science Technology and Engineering*, vol. 32, pp. 305–309, 2017.

[86] Y. Wei, X. Wang, and G. Li, "Mechanical properties test of bamboo scrimber flexural specimens reinforced with bars," *Acta Materiae Compositae Sinica*, vol. 31, no. 4, pp. 1030–1036, 2014.

[87] J. Lai, *Preparation and Performance of Inorganic Fiber Sheets Reinforced Bamboo Scrimber Composites*, Fujian Agriculture and Forestry University, 2015.

[88] Z. Zhao, Z. Xiao, B. Shu, C. Li, and S. Zhang, "Flexural behavior of carbon fiber reinforced polymer reinforced bamboo scrimber beam," *China Forestry Science and Technology*, vol. 6, pp. 127–132, 2017.

[89] L. Qin and W. Yu, "Research on surface color, properties of thermo-treated reconstituted bamboo lumber after artificial weathering test," *Advanced Materials Research*, vol. 79-82, pp. 1395–1398, 2009.

[90] X. Huang, *The Study on Accelerated Aging Method and Aging Resistant Performance of Parallel Bamboo Strand Lumber*, Nanjing Forestry University, 2009.

[91] Y. Zhang, R. Zhu, W. Yu, and D. Ren, "Performance of exterior crushed bamboo-mat composite after accelerated aging test," *China Wood Industry*, vol. 26, no. 5, pp. 6–8, 2012.

[92] R. Zhu, Y. Zhang, and W. Yu, "Changes in the chemical properties of phyllostachys iridescens bamboo with steam treatment," *Bioresources*, vol. 10, no. 3, pp. 5987–5993, 2015.

[93] Z. Wu, "Effect of freeze-thaw circle on the resistance of reconsolidated bamboo flooring," *Anhui Agricultural Science Bulletin*, vol. 23, no. 24, pp. 118–120, 2017.

[94] J. Li, Y. Chen, J. Xu et al., "The influence of media treatments on color changes, dimensional stability, and cracking behavior of bamboo scrimber," *International Journal of Polymer Science*, vol. 2018, Article ID 6068589, 7 pages, 2018.

[95] Q. Wang, B. Fei, M. Jiang, X. Liu, and S. Yang, "Hydrothermal aging evaluation method of recombinant bamboo based on X-ray computed tomography technology," *Acta Materiae Compositae Sinica*, vol. 35, no. 4, pp. 989–998, 2018.

[96] T. Su, Z. Yu, L. Hou, S. Wang, and F. Guo, "Technology on overlaying reconstituted bamboo lumber with impregnated paper," *China Forestry Science and Technology*, vol. 28, no. 5, pp. 99–101, 2014.

[97] X. Liu, Z. Lin, and X. Guan, "Study on painting performance of re-combined bamboo timber with clear coating," *Journal of Shandong Polytechnic University*, vol. 3, no. 1, pp. 18–20, 2016.

[98] F. Chen, Z. Jiang, G. Wang, Y. Qiu, X. Liu, and H. Cheng, "Preparation and mechanical properties of corrugated bamboo bundle laminated composites," *Acta Materiae Compositae Sinica*, vol. 30, no. 3, pp. 82–86, 2013.

[99] Y. Bo, *Study on the Determination of Free Phenol and Vocs in the Bamboo Scrimber*, Chinese Academy of Forestry, 2014.

[100] S. Huang, *A Study on The Design of New-Sino-Style Furniture Made of Recombinant Bamboo*, Nanjing Forestry University, 2011.

[101] Z. Tao, *The Research on Carving Process of Recombinant Bamboo Furniture*, Central South University of Forestry and Technology, 2014.

[102] X. Liu, *Research on Thedesign of Outdoor Furniture Made of Recombinant Bamboo*, Central South University of Forestry and Technology, 2014.

[103] R. Zhu and W. Yu, "Mechanical performance of a bamboo-based fiber composite for wind turbines," *China Wood Industry*, vol. 3, pp. 7–10, 2012.

[104] Z. Xiao, S. Zhang, and B. Shu, "Application of carbonized glued laminated bamboo in bamboo structure construction," *China Forest Products Industry*, vol. 40, no. 6, pp. 44-45, 2013.

[105] Y. Yu, L. Qin, and W. Yu, "Manufacturing technology of bamboo-based fiber composites used as outdoor flooring," *Scientia Silvae Sinicae*, vol. 50, no. 1, pp. 133–139, 2014.

Hindawi
Advances in Polymer Technology
Volume 2019, Article ID 5209624, 8 pages
https://doi.org/10.1155/2019/5209624

Research Article

Structure, Mechanical Performance, and Dimensional Stability of Radiata Pine (*Pinus radiata D. Don*) Scrimbers

Jinguang Wei,[1] Fei Rao,[1] Yuxiang Huang,[1] Yahui Zhang,[1] Yue Qi,[1] Wenji Yu,[1] and Chung-Yun Hse[2]

[1] *Scrimber Engineering and Technology Research Center of State Forestry Administration, Research Institute of Wood Industry, Chinese Academy of Forestry, Beijing 100091, China*
[2] *Southern Research Station, USDA Forest Service, Pineville, LA 71360, USA*

Correspondence should be addressed to Wenji Yu; chinayuwj@126.com

Received 17 April 2019; Revised 31 May 2019; Accepted 27 June 2019; Published 10 July 2019

Guest Editor: Changlei Xia

Natural wood has certain advantages such as good processability and high specific strength and thus has been used for millennium as a structural material. But the mechanical performance and water resistance, particularly for fast-growing species, are unsatisfactory for high-end applications. In this study, the "new-type" scrimber technology was introduced to radiata pine (*Pinus radiata D. Don*) scrimbers. The structure, mechanical properties, and dimensional stability of the scrimber panels were investigated. Results showed that OWFMs as basic units of scrimber had been very even in size and superior permeability. The scrimbers exhibited a three-dimensional porous structure, and the porosity had a decrease with increasing density. Both OWFMs and densification contributed to the high performance in terms of mechanical properties and water resistance. The flexural, compressive, and short-beam shearing strength were significantly enhanced with increasing density. As the density was 0.80 g cm^{-3}, the flexural strength (MOR) was approximately 120 MPa, much larger than many selected wood-based panels. Moreover, the water resistance and dimensional stability also were closely related to the density. At the density of 1.39 g cm^{-3}, the water absorption rate and thinness swelling rate of the panels in boiled water were only 19% and 5.7%, respectively.

1. Instruction

Natural materials have advantages of sustainability, renewability, and low cost and are gradually overtaking synthetic materials, which suffer from high density, environmental problems, complex processes, and high cost [1]. Wood is recognized as an excellent natural material [2]. It has high specific strength and stiffness, good processability, and favorable aesthetics and has been widely used in the fields of paper [3], package [4], furniture [5], and building [6]. Due to the shortage of high-quality wood, fast-growing wood species such as radiata pine (*Pinus radiata D. Don*) has been attracting attentions over the world [7, 8]. These woods have many advantages such as rapid growth, easy harvesting and processing, and acceptable tolerance to various site conditions. However, they also have inherent disadvantages including low density and natural defects and thus unsatisfactory mechanical properties [9, 10]. They are thus usually used in the fields of paper, package, low-end furniture, and other low-value products. For a broader utilization in high added-value application, those disadvantages need to be overcome.

Various methods, such as chemical modification, heat treatment, and densification, have been developed to obtain better properties, and pronounced effects have been demonstrated [11–16]. Among them, processing fast-growing wood into scrimber is a promising method, in which the logs with small diameters are typically crushed to form interconnected long strands by a scrimming machine [17]. The strands exhibit three-dimensional network structure comprising the dispersed fiber bundles, which not only facilitates adhesive impregnation but also reduces the effects of natural defects on product performance [18]. The scrimber density can be adjusted in the range from 0.85 to 1.2 g cm^{-3} to meet the application requirement, and the mechanical performance is superior to that of many existed wood-based panels [19]. However, those bundles are very uneven in size, which gives

rise to many drawbacks for scrimber products. The density variation, for example, leads to poor end-product quality such as curl, deformation, and rough surface.

To address these problems, Yu and his coworkers improved the preparation method [20, 21]. In the new method, round wood was first peeled into thick veneers and then split into the oriented wood fiber mats (OWFMs) by a fluffing machine. The mats had very even fiber strands, which significantly improved the adhesive distribution and the density uniformity [22]. Since a series of uniform linear-shaped cracks were formed on the surface, the mat had better permeability than the bundles prepared by the old method. These improvements contributed to the achievement of excellent performance in terms of mechanical strength and water resistance. In addition, the scrimber panels (named new-type scrimber) preserved the structural characteristics of natural wood (e.g., fiber orientation and appearance), and it could safely be processed as the logs, even with high design strength and availability in large dimensions [23]. The new method has been successfully applied to a hardwood poplar wood (*Populus ssp.*) in China, but few attempts have been made to apply to softwood [20].

Radiata pine is a most widely planted fast-growing softwood in the Southern Hemisphere. It has been a mainstay of the forest economy and reduced cutting pressure on native forests in Australia, New Zealand, Chile, Argentina, Uruguay, Kenya, and the Republic of South Africa [24]. Like other softwoods, it has low density in the range from 0.40 to 0.50 g m^{-3} and unsatisfactory mechanical properties. For example, the pine with a mean density of 0.48 g cm^{-3} has an ultimate bending strength of approximately 75 MPa and modulus of elasticity of approximately 9 GPa [25], which cannot meet the requirement of high-end applications. The emergence of "new-type" scrimber technology has great possibility of improving pine wood performance and extending the application fields.

In this study, the process method of new-type scrimber was used to fabricate pine scrimber. The microstructure, mechanical properties, water resistance, and dimensional stability were investigated, and the effect of density also was discussed. The objective of this study is to explore the extensive applicability of the new-type scrimber technology and to develop high-performance wood materials using inexpensive and abundant pine wood.

2. Material and Method

2.1. Materials. Radiata pine with a diameter of ~ 450 mm and a basic density of 0.42 g cm^{-3} was purchased from Linyi Jinshan Wood Co., Ltd. (China). Phenol formaldehyde (PF) resin with the number-average molecular weight of 596, solid content of 47.49%, viscosity of 41 mPa·s at 25°C, and pH of 10.22 was applied by Dynea Guangdong Co., Ltd. Other reagents were of chemical grade throughout the experiment and purchased from Aldrich Chemical (Shanghai) Co., Ltd.

2.2. Methods

2.2.1. Scrimber Fabrication. The pine log without barks was used as raw material to prepare the oriented wood fiber mats according to the reported method [20], and the scrimbers were obtained through laminating the mats impregnated with PF resin. In brief, round wood was softened in the boiled water and then peeled into the flat veneers with 6 mm in thickness using the spindleless veneer lathe (Xuanjin, China). The veneers were split along the wood growth direction by a fluffing machine into the fiber mats. The mats were dried in an oven at 70°C until the moisture content was approximately 10%. The dried mats were impregnated with dilute PF resin (solid content of 10 wt.%) and the weight gain was 13 wt.% based on the weight of dried mats. The wet mats with resin were air-dried until the moisture content reached 11 wt.%. A certain weight of the dried mats with resin was assembled along the grain direction in the mold. Hot pressing was conducted at 145°C for 30 min on a Model 3856 thermocompressor (CARVER, USA) to obtain the board (300 × 200 × 20 mm^3). By changing the mat weight, a series of scrimber boards were obtained with various densities (i.e., 0.80, 1.01, 1.20 and 1.39 g cm^{-3}). Prior to testing, the scrimber boards were conditioned in a chamber at 65 ± 5% relative humidity (RH) at 20 ± 2°C for two weeks.

2.2.2. Water Loading of OWFMs. The permeability of thick veneers and OWFMs were characterized by the water loading rate (*WLR*). The samples were immersed in water at room temperature for 5 min then taken out and placed vertically for another 5 min. The rate was calculated by

$$WLR = (m_2 - m_1) \times \frac{100\%}{m_1}, \quad (1)$$

where m_1 and m_2 were the weights of samples before and after water impregnation, respectively.

2.2.3. Morphological Observation. Microstructure of transverse sections was observed using a S3400 scanning electron microscope (SEM) (Hitachi, Japan) at an accelerating voltage of 5.0 kV. Samples were made of the same wood at the same position to ensure the comparability. Prior to observation, the surface was smoothed with a sliding microtome and then sputter-coated with a thin layer of gold.

2.2.4. Determination of Porosity. The apparent density (ρ_a) was considered as the ratio between the mass of a sample and the total volume it occupied. The substantial density (ρ_s) was defined as the ratio between the mass of the sample and the actual volume it occupied. ρ_s was measured by an AccuPyc 1330 pycnometer (Micromeritics, USA) at 22 ± 0.5°C. For accuracy, the sample was transversely cut into small slices with 2 μm in thickness and at least five duplicates were measured for each sample. The porosity (ε) was defined as the fraction of the volume of voids over the total volume of the sample, and it was calculated by [26]

$$\varepsilon = \left(1 - \frac{\rho_a}{\rho_s}\right) \times 100\% \quad (2)$$

2.2.5. Mechanical Testing. The flexural and compressive properties of scrimber samples were tested according to the standard of GB/T 17657-2013 and the short-beam shearing

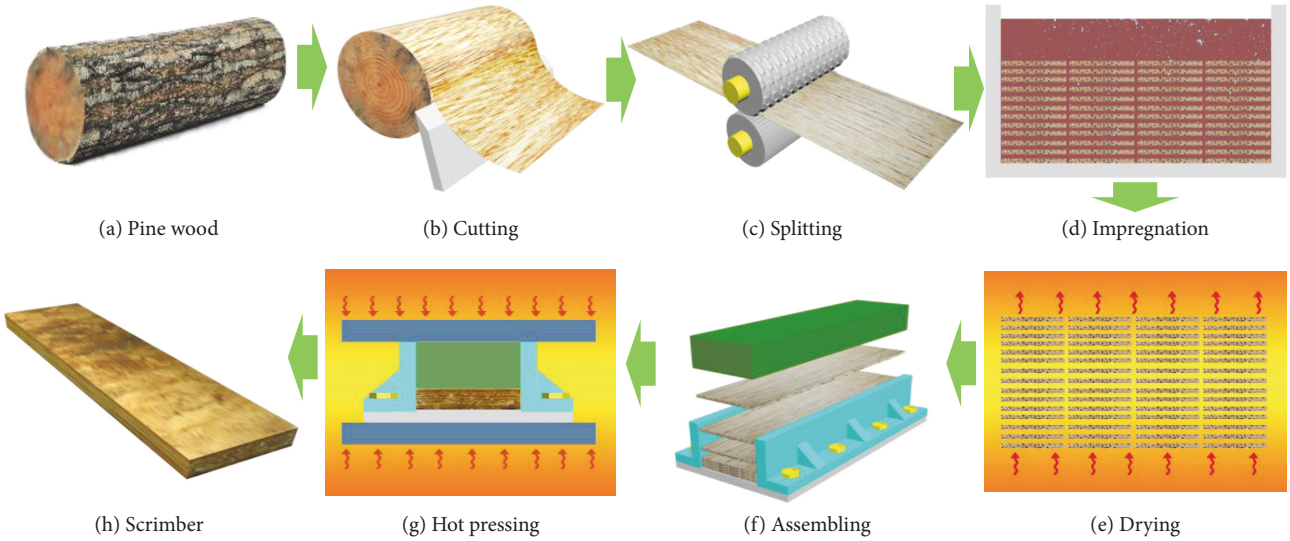

Figure 1: Diagrams of scrimber preparation.

according to the standard of GB/T 20241-2006. All tests were performed on a CMT5105 universal testing machine (MTS systems, China). For each density, at least eleven samples were tested to ensure good reproducibility.

2.2.6. Water Resistance. The water absorption rate (*WAR*), thickness swelling rate (*TSR*), and width swelling rate (*WSR*) of scrimber samples were measured according to the standard GB/T 30364-2013. The samples were boiled for 4 hours, dried at 63 ± 3°C for 20 hours and boiled for another 4 hours. *WAR* was calculated by

$$WAR = (w_2 - w_1) \times \frac{100\%}{w_1}, \quad (3)$$

where w_1 and w_2 were the sample weight before and after boiling, respectively. And TSR was calculated by

$$TSR = (t_2 - t_1) \times \frac{100\%}{t_1}, \quad (4)$$

where t_1 and t_2 were the thickness of the sample before and after boiled, respectively. Similarly, WSR was calculated as well.

3. Results and Discussion

3.1. Scrimber Formation. Figure 1 shows the diagrammatical process of pine scrimbers, which mainly involves rotary-cutting of round wood, directional splitting of thick veneers, impregnating with phenolic resin, and hot pressing. The rotary-cut veneers had flat surface and uniform thickness. As directionally split by the fluffing machine, the veneers turned into web-like fiber mats. As like the flat veneer, the mat preserved a whole sheet with well-distributed density. Compared to the strands obtained directly from the crushed log, the mat surface was flatter, and thus it was easier for layup. In addition, there existed a series of dotted and linear-shaped cracks on the mat surface (Figure 2(b)), which offered many paths for liquid impregnation. The water loading rate of OWFMs was 161.34 wt.%, which was four folds more than that of the flat (or split-free) veneers (Figure 2(c)). Apart from enhanced permeability, low-molecular-weight PF resin used in this study allowed more adhesive penetrating into the lumens and cell walls. It has been proven that phenolic resin can prominently soften wood cell walls and decrease the Young's modulus (MOE) of wood fibers [27]. More resin could facilitate the collapse of cell walls at lower pressure. Heat also can effectively soften the wood and make the pressing easier. In comparison with the cold-pressing and hot-curing method, the hot pressing saved more than 90% of the time, which were obtained from the reported literature [28, 29].

3.2. Microstructure. The cross-section surfaces of scrimbers were observed at microscopic scales, and their micrographs are shown in Figure 3. All scrimbers exhibited a three-dimensional porous structure consisting of axial tracheids with fair dense cell walls. But there still existed the difference between them due to various densities. For the scrimbers with a density of 0.8 g cm^{-3}, the cell walls had less deformation along the pressing direction (Figure 3(a)). Some walls were divided from each other and the narrow gaps were formed, which may arise from the intercellular bonding destruction during the hot pressing. As the density increased, the cell shape became more and more irregular. For the scrimber with 1.2 g cm^{-3}, almost cell walls collapsed layer by layer, accompanied by the walls cracking (Figure 3(c)). When the density reached 1.39 g cm^{-3}, a majority of lumens were filled with the collapsed walls, and most walls had been barely distinguished (Figure 3(d)).

Figure 4 shows that the average porosity of scrimbers sharply decreased with increasing density. The porosity decreased from 68% for the pine wood to 46% for the scrimbers with a density of 0.80 g cm^{-3}. In the case of the scrimbers with 1.39 g cm^{-3}, the porosity reached approximately 2.11%, which was only 3% of that of pine wood.

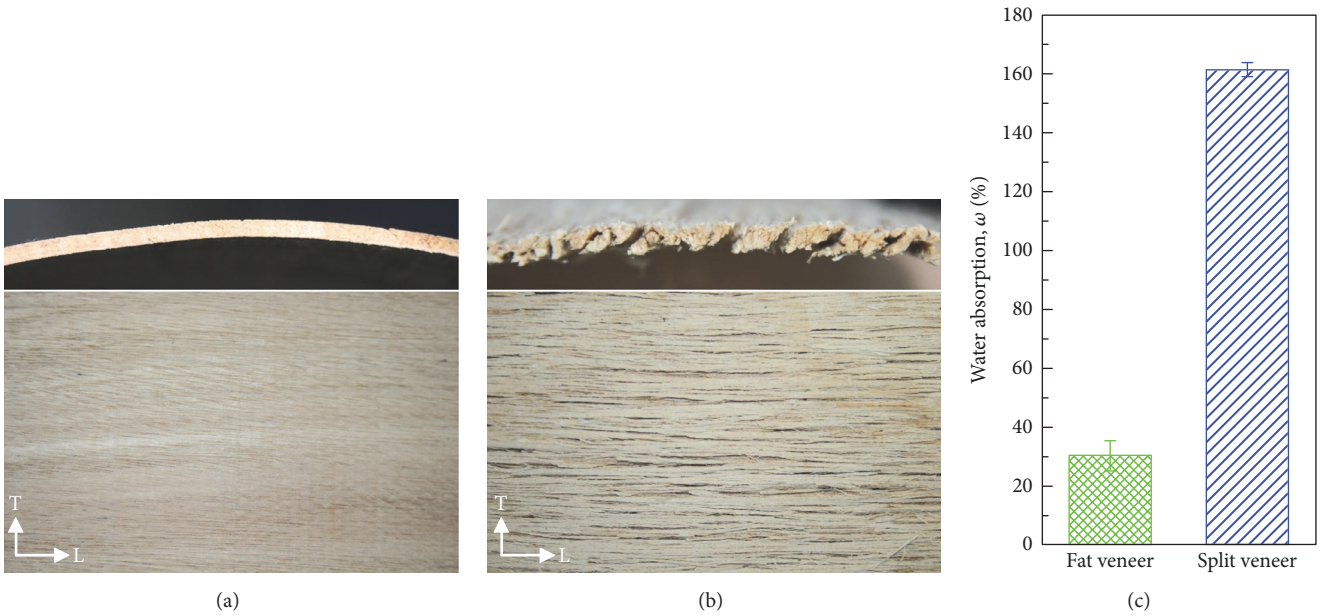

Figure 2: Surface macrograph of (a) the flat veneer and (b) OWFM, and their water loading rates.

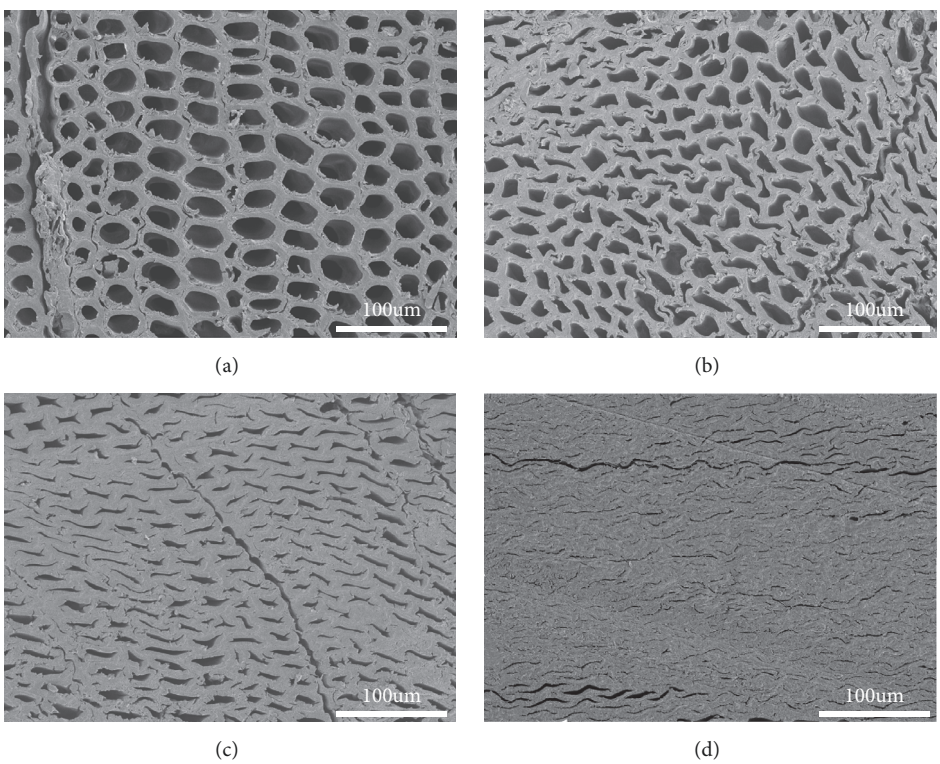

Figure 3: SEM micrographs of scrimbers with density of (a) 0.80, (b) 1.01, (c) 1.20, and (d) 1.39 g cm^{-3}.

Such low porosity may be conducive to the improvement of physical and mechanical properties.

3.3. Mechanical Properties. Figure 5 shows the strength and stiffness of scrimbers as a function of density. The flexural strength (MOR) and modulus (MOE) increased with increasing density. At the density of 0.80 g cm^{-3}, the scrimber had approximately 120 MPa in MOR, which was much larger than most selected wood-based panels as presented in Figure 6, such as pine plywood [30], pine oriented strand board (OSB) [31], kenaf particleboard [32], and wood-polymer composite (WPC) [33]. The strength almost came up to that of poplar scrimbers at the same density, which were prepared by the cold-pressing and hot-curing method [20]. As the density was

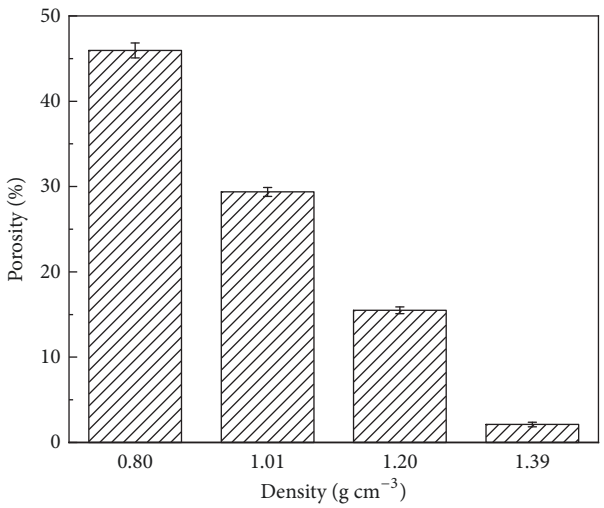

Figure 4: Porosity of scrimbers with varying densities.

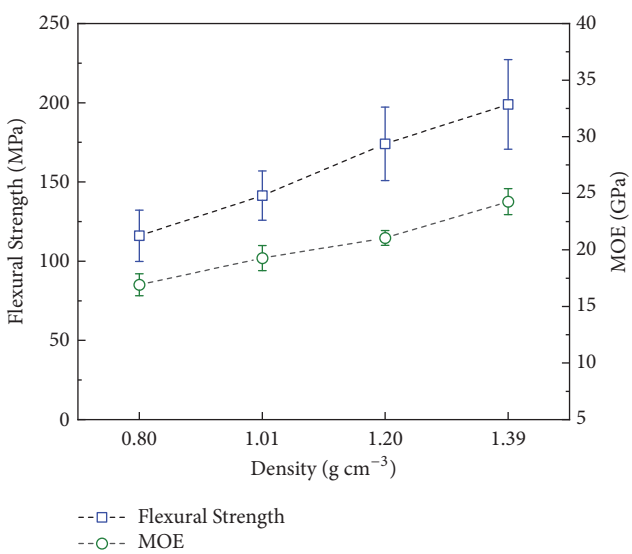

Figure 5: Flexural properties of scrimbers with various densities.

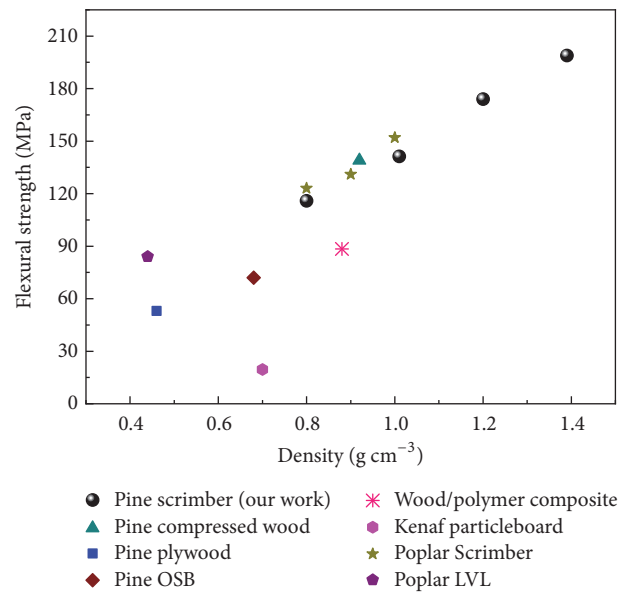

Figure 6: Comparison of flexural strength between the scrimbers and selected wood-based panels.

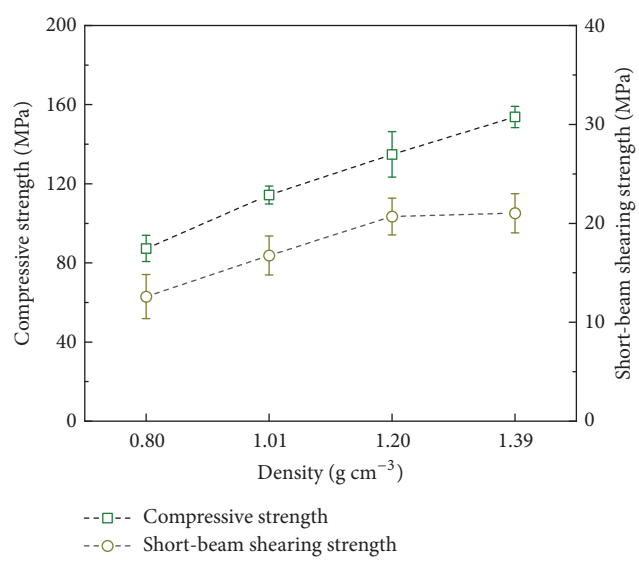

Figure 7: Compressive and short-beam shearing properties of scrimbers with various densities.

1.01 g cm^{-3}, the strength surpassed that of pine compressed wood [34]. When the density was equal to 1.39 g cm^{-3}, MOR was up to 198.92 MPa on average, which was 71% higher than that of scrimers at 0.80 g cm^{-3}. Meanwhile, the modulus had an increase by about 7.5 GPa in comparison with that at 0.80 g cm^{-3}.

Compressive and short-beam shearing properties also were enhanced with an increase of density (Figure 7). The compressive strength was 87 MPa at the density of 0.8 g cm^{-3}, which was 70% larger than that of GluBam prepared by Xiao et al. [35]. As the density reached 1.39 g cm^{-3}, the strength increased to 154 MPa and the specific strength was approximately 110 MPa g^{-1} cm^{3}. Similarly, the short-beam shearing strength, which reflects the bonding quality of laminated panels [36], increased with increasing density, but maintained at 21 MPa as the density was 1.20 g cm^{-3} or more.

These remarkable improvements were ascribed to the superior feature of OWFMs and the densified structure of scrimbers. The high permeability of OWFMs facilitated the bonding behavior between wood fibers and PF resin, thus improving the bonding strengths. Besides, the strands increased the contact area between the fiber and PF resin and between each fiber, which benefited the stress transferring. In general, the mechanical properties of lignocellulosic composites manily depended on the structure and strength of cellulosic fibers, which bears the exterior loads [37, 38]. The structural densification increased the fiber content per unit volume, resulting in high endurance capacity for these scrimbers.

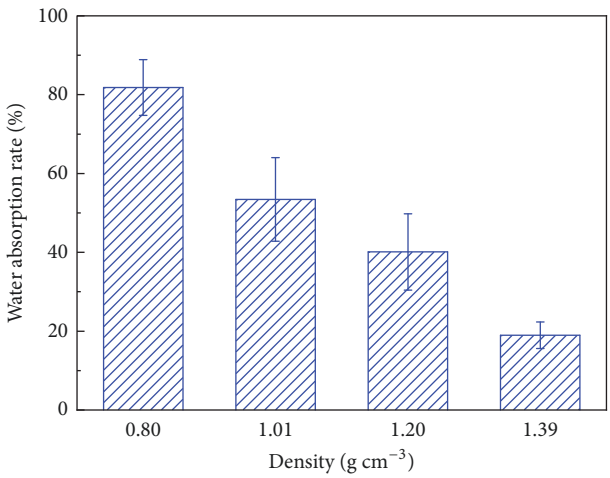

Figure 8: Water absorption rate of scrimbers with different densities.

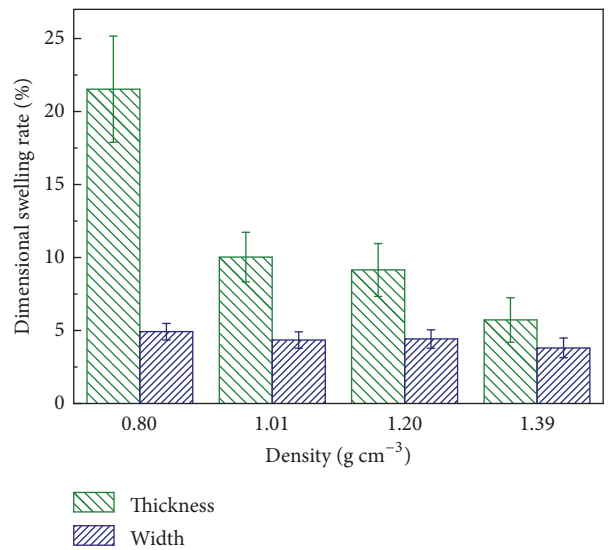

Figure 9: Dimensional swelling rate of scrimbers with different densities.

3.4. Water Absorption and Dimensional Stability. The water absorption rate of scrimbers in boiled water is depicted in Figure 8. With increasing density, the absorbed water gradually decreased. When the density was 0.80 g cm^{-3}, the absorbed water was 81.82% based on the weight of oven-dried sample, which was less than half that of pine wood (i.e., 176%). In respect to the scrimbers at the density of 1.39 g cm^{-3}, the water absorption rate was as low as 19%, which was the least value among the scrimbers in this work. Besides the molecular adsorption of cell walls, the pronounced discrepancy can be ascribed to the different porosities. The lumens offered considerable conveying channels and storage space to water [39]. Low porosity reflected fewer channels and space within the scrimber, leading to less absorbed water. Moreover, the lower the density was, the lower the porosity was, followed by less water absorbed by the scrimbers. These results suggested that the scrimbers with high density had better capacity of water resistance.

The absorbed water could cause the deformation recovery of scrimbers. As presented in Figure 9, the thickness swelling rate at the density of 0.80 g cm^{-3} was 22%, which was three times as much as that of pine wood (i.e., 7%). Besides the cell wall swelling, the recovery of compressed wood cells contributed to the great discrepancy. In the preparation process of our case, the wood cells were compressed, accompanied by extra internal stress [40]. When the scrimber was placed in the hygrothermal condition, the compressed cells tended to recover to the initial shape. In the macroscale, the recovery of cell deformations appeared as the thickness swelling. Furthermore, as the density increased, some cell walls crashed, accompanied by tiny cracks on the wall. The rate trended to decline due to the poor ability of cell recovery, confirmed by only 5.7% in thickness swelling the scrimbers at the density of 1.39 g cm^{-3} had.

Compared to the thickness, the width had much less swelling rate under any density. It could be ascribed to the fact that the wood cells were mainly compressed along the thickness direction during the hot pressing, while less deformation occurred in the width direction. In the case, the swelling rate in width was only a little but much lower than that in thickness, no matter how high the density was. It would be seen from these results that the pine scrimbers possessed high dimensional stability.

4. Conclusion

In this study, pine scrimbers were prepared using the "new-type" scrimber technology. The oriented wood fiber mats (OWFMs) as basic units of scrimber exhibited the net-like structure consisting of many sharply oriented fibers. Due to a series of cracks on the surface, the permeability was four folds more than that of the untreated veneers. SEM micrographs revealed that the cell walls were compressed along the thickness direction, resulting in decreasing porosity. Both OWFMs and densification contributed to enhanced performance in the respect of mechanics and dimensional stability. For the scrimber at the density of 0.80 g cm^{-3}, the flexural strength was much larger than that of many existed wood-based panels. As the density reached 1.39 g cm^{-3}, the strength was increased to 198.92 MPa. Meanwhile, the water absorption rate and thickness swelling rate in boiled water were only 19% and 5.72%, respectively. Such remarkable performance could endow the material with great prospects in the fields of high-value applications.

Data Availability

The data supporting the findings of this study have been not available because it is part of the programs being in progress, and it will be further studied.

Conflicts of Interest

The authors declare that they have no conflicts of interest.

Acknowledgments

This work was funded by the Special Funds for Basic Research and Operating Expenses of Central Level Public Welfare Scientific Research Institutes (CAFYBB2018SY031), Major Science and Technology Program of Hunan Province (No. 2017NK1010), and China Scholarship Council.

References

[1] D. Kretschmann, "Velcro mechanics in wood," *Nature Materials*, vol. 2, no. 12, pp. 775-776, 2003.

[2] M. Zhu, J. Song, T. Li et al., "Highly anisotropic, highly transparent wood composites," *Advanced Materials*, vol. 28, no. 26, pp. 5181–5187, 2016.

[3] K. Law and J. L. Valade, " Status of the utilization of jack pine (*Pinusbanksiana*) in the pulp and paper industry ," *Canadian Journal of Forest Research*, vol. 24, no. 10, pp. 2078–2084, 1994.

[4] Y. Andres, E. Dumont, P. Le Cloirec, and E. Ramirez-Lopez, "Wood bark as packing material in a biofilter used for air treatment," *Environmental Technology*, vol. 27, no. 12, pp. 1297–1301, 2006.

[5] T. Pakarinen, "Success factors of wood as a furniture material," *Forest Products Journal*, vol. 49, no. 9, pp. 79–85, 1999.

[6] M. H. Ramage, H. Burridge, M. Busse-Wicher et al., "The wood from the trees: the use of timber in construction," *Renewable & Sustainable Energy Reviews*, vol. 68, pp. 333–359, 2017.

[7] J. J. Balatinecz and D. E. Kretschmann, "Properties and utilization of poplar wood," in *Poplar Culture in North America (Part A)*, pp. 277–291, 2001.

[8] S. González-García, M. T. Moreira, G. Feijoo, and R. J. Murphy, "Comparative life cycle assessment of ethanol production from fast-growing wood crops (black locust, eucalyptus and poplar)," *Biomass & Bioenergy*, vol. 39, pp. 378–388, 2012.

[9] M. Frey, D. Widner, J. S. Segmehl, K. Casdorff, T. Keplinger, and I. Burgert, "Delignified and densified cellulose bulk materials with excellent tensile properties for sustainable engineering," *ACS Applied Materials & Interfaces*, vol. 10, no. 5, pp. 5030–5037, 2018.

[10] R. E. Hernández, A. Koubaa, M. Beaudoin, and Y. Fortin, "Selected mechanical properties of fast-growing poplar hybrid clones," *Wood and Fiber Science*, vol. 30, no. 2, pp. 138–147, 1998.

[11] J. H. Kwon, R.-H. Shin, N. Ayrilmis, and T. H. Han, "Properties of solid wood and laminated wood lumber manufactured by cold pressing and heat treatment," *Materials and Corrosion*, vol. 62, no. 10, pp. 375–381, 2014.

[12] W. Sun, H. Shen, and J. Cao, "Modification of wood by glutaraldehyde and poly (vinyl alcohol)," *Materials and Corrosion*, vol. 96, pp. 392–400, 2016.

[13] Z. Li, M. He, D. Tao, and M. Li, "Experimental buckling performance of scrimber composite columns under axial compression," *Composites Part B: Engineering*, vol. 86, pp. 203–213, 2016.

[14] E. Burdurlu, M. Kilic, A. C. Ilce, and O. Uzunkavak, "The effects of ply organization and loading direction on bending strength and modulus of elasticity in laminated veneer lumber (LVL) obtained from beech (Fagus orientalis L.) and lombardy poplar (Populus nigra L.)," *Construction and Building Materials*, vol. 21, no. 8, pp. 1720–1725, 2007.

[15] X. Dong, X. Zhuo, J. Wei, G. Zhang, and Y. Li, "Wood-based nanocomposite derived by in situ formation of organic-inorganic hybrid polymer within wood via a sol-gel method," *ACS Applied Materials & Interfaces*, vol. 9, no. 10, pp. 9070–9078, 2017.

[16] P. S. H'ng, L. Y. Chai, K. L. Chin et al., "Urea formaldehyde impregnated oil palm trunk as the core layer for three-layered board," *Materials and Corrosion*, vol. 50, no. 17, pp. 457–462, 2013.

[17] F. F. Kollmann, E. W. Kuenzi, and A. J. Stamm, *Principles of Wood Science and Technology: II Wood Based Materials*, Springer Science & Business Media, 2012.

[18] M. He, D. Tao, Z. Li, and M. Li, "Mechanical behavior of dowel-type joints made of wood scrimber composite," *Materials*, vol. 9, no. 7, p. 581, 2016.

[19] T. Joscak, A. Teischinger, U. Mueller, and R. Mauritz, "Production and material performance of long-strand wood composites-review," *Wood Research*, vol. 51, no. 3, pp. 37–49, 2006.

[20] Y. Zhang, X. Huang, Y. Zhang, Y. Yu, and W. Yu, "Scrimber board (SB) manufacturing by a new method and characterization of SB's mechanical properties and dimensional stability," *Holzforschung*, vol. 72, no. 4, pp. 283–289, 2018.

[21] Y. Zhang, Y. Huang, Y. Qi, and W. Yu, "Novel engineered scrimber with outstanding dimensional stability from finely fluffed poplar veneers," *Measurement*, vol. 124, pp. 318–321, 2018.

[22] Y. Wei, F. Rao, Y. Yu, Y. Huang, and W. Yu, "Fabrication and performance evaluation of a novel laminated veneer lumber (LVL) made from hybrid poplar," *European Journal of Wood and Wood Products*, vol. 77, no. 3, pp. 381–391, 2019.

[23] Y. Zhang, Y. Qi, Y. Huang, Y. Yu, Y. Liang, and W. Yu, "Influence of veneer thickness, mat formation and resin content on some properties of novel poplar scrimbers," *Holzforschung*, vol. 72, no. 8, pp. 673–680, 2018.

[24] K. Bayne, "Wood quality considerations for radiata pine in international markets," *New Zealand Journal of Forestry*, vol. 59, pp. 23–31, 2015.

[25] F. A. Kamke, "Densified radiata pine for structural composites," *Maderas: Ciencia y Tecnologia*, vol. 8, no. 2, pp. 83–92, 2006.

[26] C. A. Sologubik, L. A. Campañone, A. M. Pagano, and M. C. Gely, "Effect of moisture content on some physical properties of barley," *Industrial Crops and Products*, vol. 43, no. 5, pp. 762–767, 2013.

[27] M. I. Shams and H. Yano, "Compressive deformation of wood impregnated with low molecular weight phenol formaldehyde (PF) resin II: effects of processing parameters," *Journal of Wood Science*, vol. 50, no. 4, pp. 343–350, 2004.

[28] Y. H. Zhang, Y. M. Zhang, D. H. Ren, and Y. U. Wen-Ji, "Effect of manufacturing technology on scrimber performance," *China Wood Industry*, vol. 30, no. 5, pp. 31–34, 2016.

[29] X. Guo, Y. Lin, B. Na et al., "Evaluation of physical and mechanical properties of fiber-reinforced poplar scrimber," *BioResources*, vol. 12, no. 1, pp. 43–55, 2016.

[30] F. Arriaga-Martitegui, F. Peraza-Sánchez, and L. García-Esteban, "Characteristic values of the mechanical properties of radiata pine plywood and the derivation of basic values of the layers for a calculation method," *Biosystems Engineering*, vol. 99, no. 2, pp. 256–266, 2008.

[31] C. Barbuta, P. Blanchet, A. Cloutier, V. Yadama, and E. Lowell, "OSB as substrate for engineered wood flooring," *European Journal of Wood and Wood Products*, vol. 70, no. 1-3, pp. 37–43, 2012.

[32] A. H. Juliana, M. T. Paridah, S. Rahim, I. Nor Azowa, and U. M. K. Anwar, "Properties of particleboard made from kenaf

(Hibiscus cannabinus L.) as function of particle geometry," *Materials & Design*, vol. 34, pp. 406–411, 2012.

[33] E. Baysal, M. K. Yalinkilic, M. Altinok, A. Sonmez, H. Peker, and M. Colak, "Some physical, biological, mechanical, and fire properties of wood polymer composite (WPC) pretreated with boric acid and borax mixture," *Construction and Building Materials*, vol. 21, no. 9, pp. 1879–1885, 2007.

[34] M. K. Dubey, S. Pang, S. Chauhan, and J. Walker, "Dimensional stability, fungal resistance and mechanical properties of radiata pine after combined thermo-mechanical compression and oil heat-treatment," *Holzforschung*, vol. 70, no. 8, pp. 793–800, 2016.

[35] Y. Xiao, R. Yang, and B. Shan, "Production, environmental impact and mechanical properties of glubam," *Construction and Building Materials*, vol. 44, pp. 765–773, 2013.

[36] A. Krishnan and L. R. Xu, "Systematic evaluation of bonding strengths and fracture toughnesses of adhesive joints," *The Journal of Adhesion*, vol. 87, no. 1, pp. 53–71, 2011.

[37] Y. Yu, X. Huang, and W. Yu, "A novel process to improve yield and mechanical performance of bamboo fiber reinforced composite via mechanical treatments," *Composites Part B: Engineering*, vol. 56, no. 1, pp. 48–53, 2014.

[38] I. M. de Rosa, J. M. Kenny, D. Puglia, C. Santulli, and F. Sarasini, "Morphological, thermal and mechanical characterization of okra (*Abelmoschus esculentus*) fibres as potential reinforcement in polymer composites," *Composites Science and Technology*, vol. 70, no. 1, pp. 116–122, 2010.

[39] A. J. Stamm, "Movement of fluids in wood—part I: flow of fluids in wood," *Wood Science and Technology*, vol. 1, no. 2, pp. 122–141, 1967.

[40] S. Fukuta, F. Asada, and Y. Sasaki, "Manufacture of compressed wood fixed by phenolic resin impregnation through drilled holes," *Journal of Wood Science*, vol. 54, no. 2, pp. 100–106, 2008.

Hindawi
Advances in Polymer Technology
Volume 2019, Article ID 1045280, 7 pages
https://doi.org/10.1155/2019/1045280

Research Article

Imaging of Internal Defects of Polymer-Modified Wood Using Total Focusing Method

Liping Sun,[1] Hongju Zhou,[1] Hongwei Zhou ,[1] Guizhong Jiao,[2] and Ling Ma[1]

[1]*Northeast Forestry University, Harbin, Heilongjiang, China*
[2]*East China Optoelectronic Integrated Device Research Institute, Bengbu, Anhui, China*

Correspondence should be addressed to Hongwei Zhou; easyid@163.com

Received 18 April 2019; Accepted 29 May 2019; Published 17 June 2019

Guest Editor: Changlei Xia

Polymer modification can improve the stability and corrosion resistance of wood, but it could create defects inside wood during the modification processing. Detection of defects inside polymer-modified wood can reduce wood losses and prevent the occurring of defects. Data simulation and tomographic imaging of polymer-modified wood internal defects were carried out using electromagnetic waves with nondestructive testing. This study constructed the polymer-modified wood models, simulated the electromagnetic scattering wave, and used the total focusing method to perform tomography of the defects in the polymer-modified wood. By analyzing the imaging characteristics of different types of defects, the effectiveness of electromagnetic waves in the detection of internal defects of polymer-modified wood was proved. This method can be extended to test internal defects of other high molecular polymers.

1. Introduction

As a renewable material, wood has been widely used in various fields such as construction, decoration, and energy. However, defects of wood such as warp, crack, and decay caused by the changing of external temperature and humidity have caused serious economic losses in wood production [1]. In order to reduce the defects of wood and improve its physical and chemical properties, the modification of wood began in the early 20th century [2, 3]. The stability and corrosion resistance of polymer-modified wood have been significantly improved compared to the wood modified by other modification methods and gradually became the main method of wood modification [4, 5]. The polymer-modified wood has a wide range of applications in buildings and outdoor wood products. However, defects may occur inside wood during processing or service, and the detection of defects inside the polymer-modified wood can reduce losses and prevent from the defect occurring in advance [6].

The nondestructive testing technology can find the defects of wood by comparing the differences of physical or chemical characteristics [7]. Methods such as the electromagnetic wave detection, laser detection, infrared detection, ultrasonic detection, nuclear magnetic resonance, and X-ray detection have been widely used in the metal defect detection, ground penetrating radar, medical imaging, and other fields [8–10]. There are various methods for detecting polymer-modified wood, such as the infrared detection, ultrasonic detection, stress wave detection, and X-ray detection [11–13]. Each of these methods has its advantages and disadvantages, but there is no single method that can easily and effectively detect the internal defects of the polymer-modified wood. Infrared detection method detects the internal defects of polymer-modified wood by the phenomenon of abnormal temperature rise, but it is greatly affected by environmental factors. Sunlight, airflow, air temperature and humidity, and surface leakage current would affect the detection signals of the infrared detection method [14]. The ultrasonic detection method requires coupling agent and needs to select a probe that matches the acoustic impedance which requires close contact with the surface of the testing samples, which limits its application range [15]. The stress wave detection requires the sensors to be nailed to the polymer-modified wood, which would cause damage. The X-ray inspection equipment

costs too much and also has a safety concern; e.g., if used improperly, it can cause radiant damage to human body [16].

In this paper, the total focusing method was applied to make the image inversion of the electromagnetic wave propagation data in the composite insulator to achieve the purpose of nondestructive testing. The total focus method is mostly used in phased array ultrasonic monitoring systems; this method has been widely used in many fields such as petroleum exploration and industrial product testing [17, 18]. The principle is to coherently sum all the elements to focus at each point in the image reconstruction area. This method can define various reconstruction networks and achieve high-precision reconstruction [19, 20].

2. Method

The total focusing method collects data by the full matrix capture method, and the acquisition step is to record the signals between all array elements as shown in Figure 1. The signals collected by the transmitting element i and the receiving element j are denoted by $E(t, u_i, v_j)$, where u_i and v_j, respectively, represent the positions of the transmitting array elements and the receiving array elements. If N represents the total number of elements, the data set is defined as $E(t, u, v)(1 \le i \le N, 1 \le j \le N)$. As for reconstruction of any sample point (x, y) in the solution domain, it can be given by the following.

$$O(x, y) = \sum_{i=1}^{N}\sum_{j=1}^{N} E\left(\frac{r_1 + r_2}{c/\sqrt{\varepsilon}} + \tau, u_i, v_j\right) \quad (1)$$

In the formula $r_1 = \sqrt{(x - u_i)^2 + y^2}$, $r_2 = \sqrt{(x - v_j)^2 + y^2}$, c is the propagation speed of electromagnetic waves in vacuum, ε is the relative dielectric constant of the background medium (assuming that the polymer-modified wood material is uniform and isotropic) [21, 22], and τ is the time constant. The calculation process is equivalent to focus at each point (x, y).

The time constant τ consists of two parts: one is from the gprMax simulation software, and the other depends on the wavelength of the excited electromagnetic wave. There is a "zero zone" of the initial emission time in the gprMax simulation software, and no electromagnetic waves are emitted in this region. That is, the electromagnetic wave starts to emit later than zero-time. In the imaging result, the data of each sampling point comes from the value at the peak of the Ricker wave, which corresponds to $\lambda/2c$. The time constant τ corresponding to the electromagnetic wave of 1 GHz is 1.6121 ns.

A certain transmitting point of the electromagnetic wave array element transmits a signal which is received by all other receiving points, which means that "one transmits and more receive" the electromagnetic wave signal. This process is repeated for all array elements, which means "point-by-point transmission, total focus".

Acrylonitrile is a good wood intumescent agent, which can be used for impregnating the plasticized wood to increase its dimensional stability. In this paper, the acrylonitrile modified wood was taken as an example to develop a defect

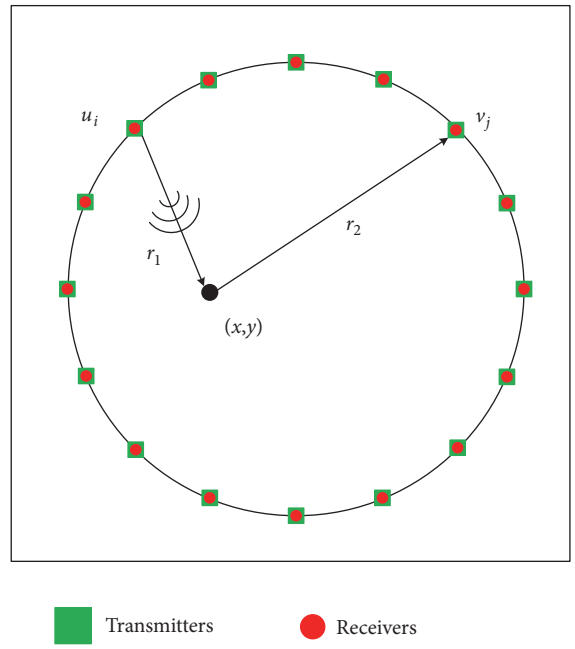

Figure 1: Schematic diagram of data acquisition for the total focusing method.

simulation model, and its factors were set to be a shape diameter of 0.18 m, a relative dielectric constant of 8, the dielectric loss tangent of 0.0038, the volume resistivity of 8.93×10^8M • Ω • cm, the surface resistivity of 9.287×10^8M • Ω, and the heat distortion temperature of 307°C. A two-dimensional space model of the solution domain (0.2m, 0.2m) was developed using the gprMax simulation software, on a circumference with a center of (0.1m, 0.1m) and a radius of 0.09m, N=16 array elements, which were equally spaced and each array element had a transmitter and a receiver. The transmitter sequentially emits a Ricker wave with a frequency of f=1GHz, and the waveform function is $\chi(t) = -A[2\pi^2 f^2(t - \sqrt{2}/f)^2 - 1]e^{-\pi^2 f^2 (t-\sqrt{2}/f)^2}$, $t > 0$, received by all receivers. Time window $t_w = 2y/(c/\sqrt{\varepsilon}) + 1/f + \tau \approx 9$ ns.

3. Experimental Results and Analysis

In this study, the circular polymer-modified wood model with preset defects was taken as the research sample. The electromagnetic wave was used to simulate the nondestructive testing of polymer-modified wood. The position, size, shape, and other related information of the defects were obtained by the electromagnetic wave propagating in the medium. Specifically, it involved the influence of the type, position, shape, and quantity of the defect medium on the inversion imaging of the electromagnetic wave total focusing method.

3.1. Single Circular Air Defect Simulation Imaging. The internal defects of the polymer-modified wood were set to be a circular air diameter of 0.02 m, and the circle center at (0.1m, 0.1m). As shown in Figure 2, the model was simulated using

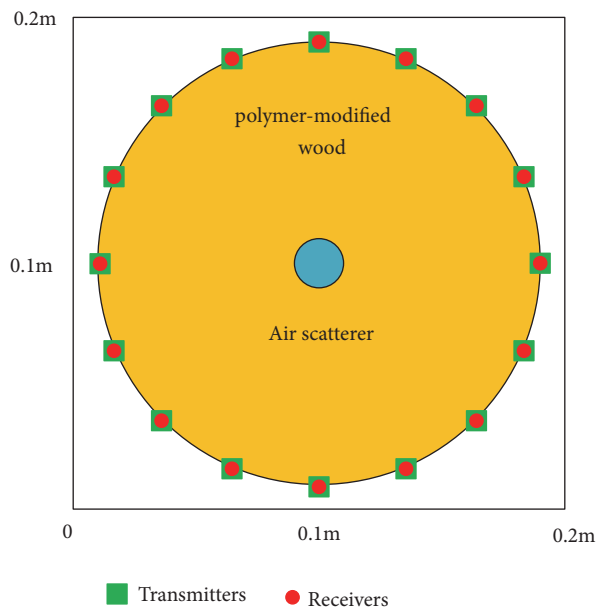

Figure 2: Single circular air defect model diagram.

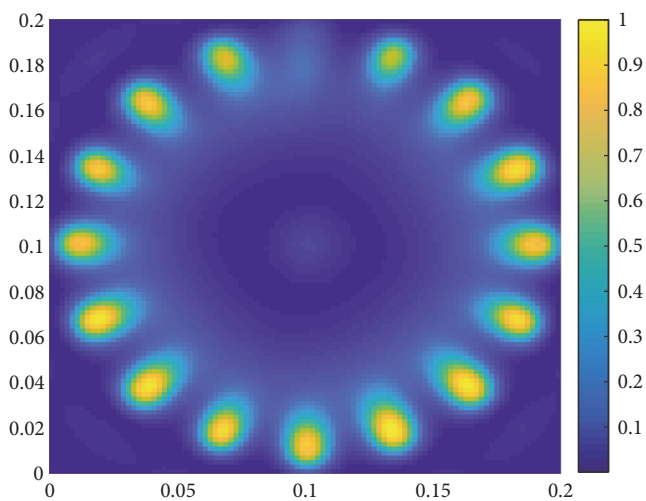

Figure 3: Single circular air defect inversion imaging diagram.

the gprMax software. The inversion results are shown in Figure 3. As shown in the figure, the air defect (weak scattered) was insensitive to the scattering of electromagnetic waves, there were obvious bright spots at the 16 array elements, and the defect position information was not obvious.

3.2. Single Circular Metal Defect Simulation Imaging. In order to explore the problem that the air defect imaging was not obvious, the defect was set to a circular metal with a diameter of 0.02 m, and the circle center at (0.1m, 0.1m). Figure 4 shows the model that was simulated by using gprMax software. The inversion results are shown in Figure 5. As shown in Figure 5, the metal defects (strong scatterers) were sensitive to electromagnetic waves, and the total focusing method can clearly and accurately image the metal defects.

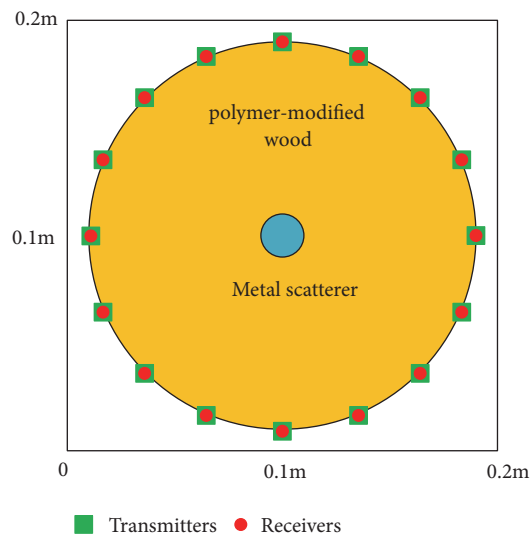

Figure 4: Single circular metal defect model.

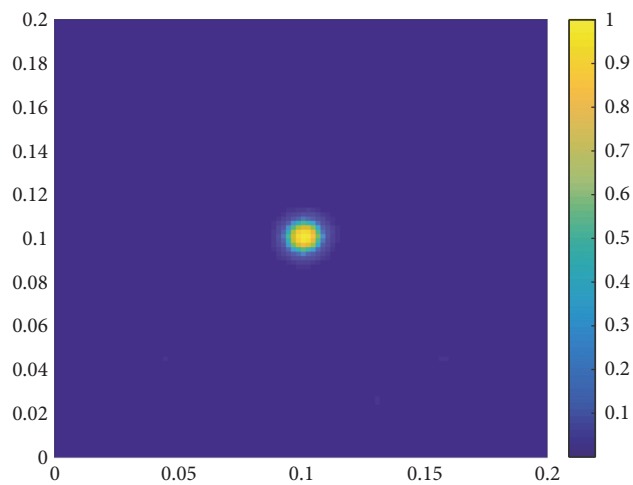

Figure 5: Single circular metal defect inversion image.

3.3. Improvement of the Total Focusing Method of Weak Scatterers. By comparing the A-scan data of the metal defect model, the air defect model and the no defect model at the same array are shown in Figure 6. It was found that the curves of the metal defect model and the air defect model were similar to those of the defect-free model in the range of 0 to 2.57 ns, where the data came from the electromagnetic wave signals emitted by the transmitter at the same array element, which was not directly received by the receiver through the scatterer. In the range of 2.57 ns to 4 ns, the curve of the metal defect model was significantly different from that of the defect-free model, and the difference between the air defect model and the defect-free model was small, where the data was from the scattering field data of the electromagnetic wave in the medium propagation process. In the range of 4 ns to 8 ns, the curves of the three models were similar, and the data fluctuation amplitude was much smaller than the data fluctuation in the range of 0 to 4 ns, where the data came

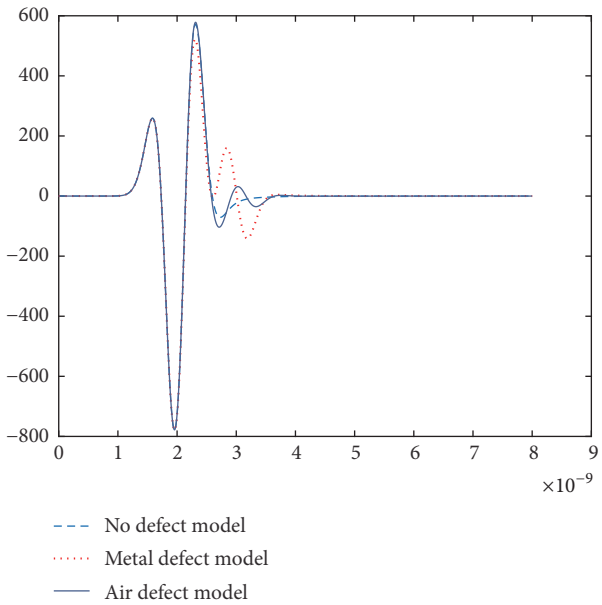

Figure 6: Comparison of A-scan scan data at the same array.

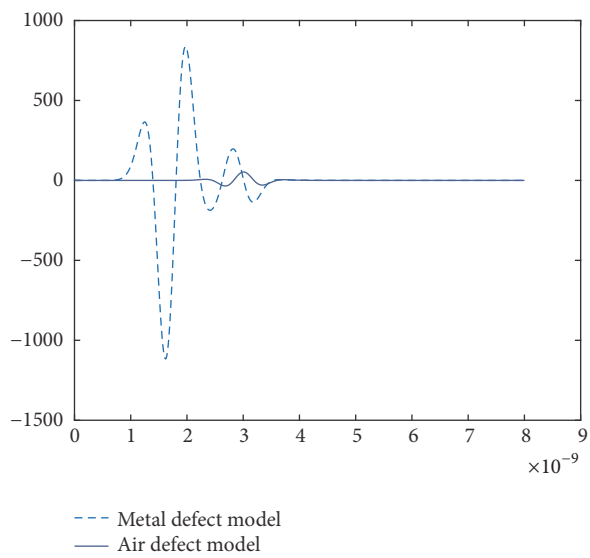

Figure 7: Comparison of scattering fields between metal defect model and air defect model.

from the scattering on the circumference of the background medium.

As shown in Figure 7, after subtracting the metal defect model data and the no defect model data, the scattering field data of the metal defect model was obtained. After the air defect model data and the no defect model data were subtracted, the scattering field data of the air defect model was obtained. Comparing the curves of the two models, it can be found that the scattering field data of the two models were not zero in the range of 2.7 to 4 ns, the scattering field intensity of the metal defect in the range of 0 to 2.57 ns was much larger than the scattering field intensity of the air defect, and the

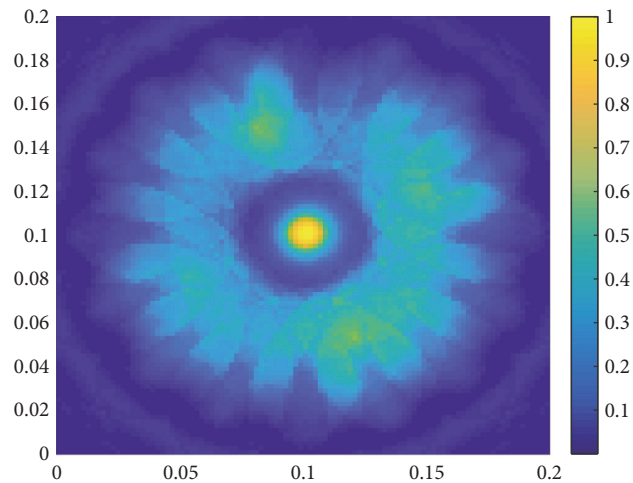

Figure 8: Image of the air defect model after pretreatment.

scattering field of the air defect was similar to the scattering field intensity at 2.57 to 4 ns.

Since we only cared about the scattering field data at the defect and needed to eliminate scattering field data from background media as much as possible, we pre-zero the scattered field data in the range of 0 to 2.57 ns and 4 to 8 ns and then made the inversion imaging calculation with the total focusing method. The image of the air defect model after preprocessing is shown in Figure 8.

3.4. Simulated Imaging of Air Defects in Different Shapes and Positions. The internal defects of the polymer-modified wood were set to a circular air with a diameter of 2 cm, and the circle center at (0.1m, 0.05m) as shown in Figure 9(a). Figure 9(b) shows that the rectangular air gap has a slit length of 0.1 m and width of 0.02 m. The vertex coordinates are sequentially A (0.05m, 0.099m), B (0.05m, 0.101m), C (0.15m, 0.101m), and D (0.15m, 0.099m), by using gprMax software to separate the two models and perform simulation calculations as shown in Figure 9(b). The inversion results are shown in Figures 10(a) and 10(b). The inversion calculation of the total focusing method can accurately detect the shape information of the defects, but the position information of the inversion imaging had a certain error compared with the model. The simulation position of the defect was compared with the model position and it can be found that it rotated about 12.5° clockwise with the center of the model as the center.

3.5. Multiple Circular Air Defect Simulation Imaging. The internal defects of the polymer-modified wood were set to two circular airs of 0.02 m in diameter, and the centers at A (0.05m, 0.1m) and B (0.15m, 0.1m), respectively, as shown in Figure 11(a), with three diameters of 0.02 m. The circular air, centered at A (0.7m, 0.7m), B (0.10m, 0.13m), and C (0.13m, 0.07m) as shown in Figure 11(b), was obtained using the gprMax software to separate the two models' simulation calculation. The inversion results are shown in Figures 12(a) and 12(b). The inversion calculation of the total focusing

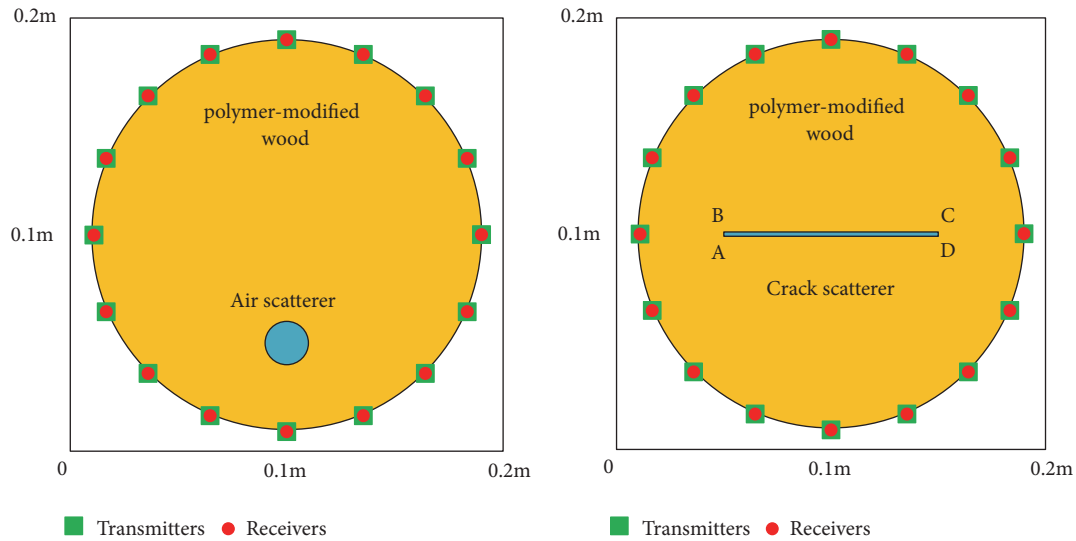

(a) Circular defect model diagram (b) Slot defect model diagram

Figure 9

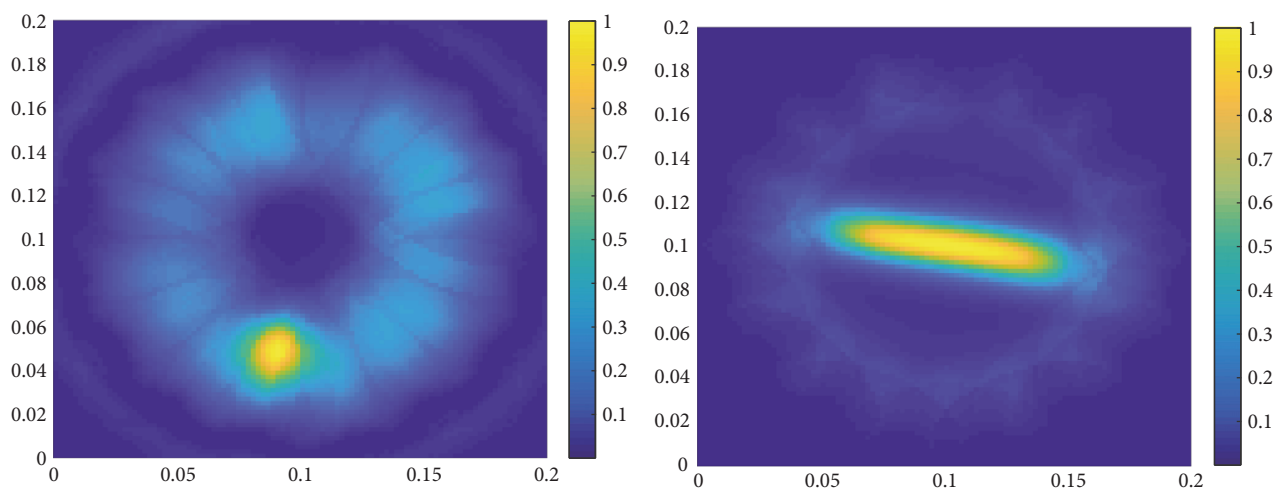

(a) Circular defect inversion imaging (b) Slot defect inversion imaging

Figure 10

method can detect multiple circular defect information, but the position information had an error of about 12.5°.

3.6. Discussion and Analysis. The total focusing method for electromagnetic wave scattering field data reconstruction that inverted spatial scatterer images from time-domain signals from all combinations of transmit-receive array elements was used in this study. The simulation results showed that the scattering field data could be reconstructed at each sampling point in space using the total focusing method, so that the position where the scattering field value was prominent formed a "bright spot" to achieve the purpose of imaging. The strength of the "bright spot" depended on the scattering intensity of the scatterer on the electromagnetic wave, and the metal scatterer had a better imaging effect than the air scatterer. In order to solve the problem that the air scatterer imaging was not ideal, the direct wave data in the scattered field was preprocessed and then the inversion imaging calculation was performed. The deviation between the simulation imaging results of the gap model and the multicircle model and the position of the scatterer in the model was expected to be solved by increasing the transmit-receive array elements (N>16).

4. Conclusion

In this paper, the objective of imaging the internal defects of polymer-modified wood was realized by the forward modeling of electromagnetic wave and the inversion imaging calculation of the total focusing method. By measuring the scattered waves generated at the normal tissue and defect

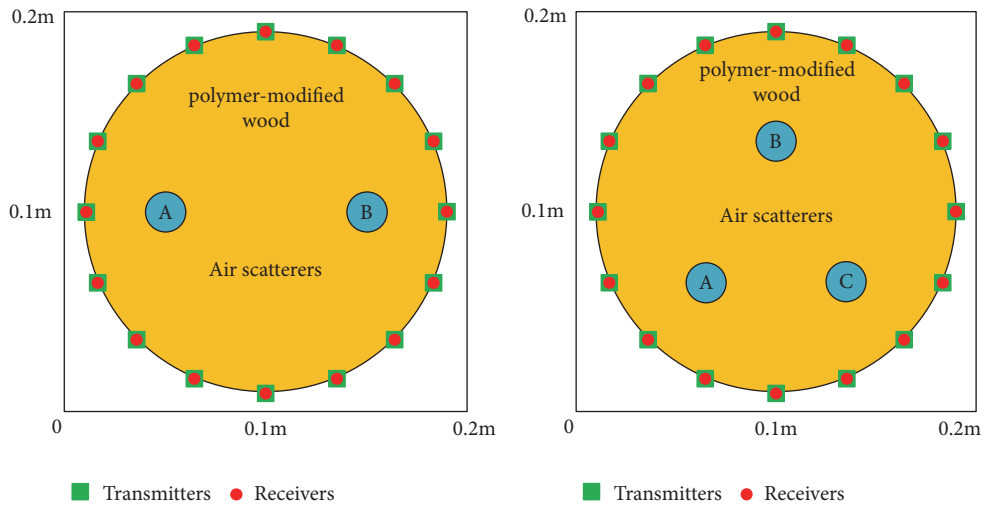

(a) Double-circle defect model diagram (b) Three-circle defect model diagram

Figure 11

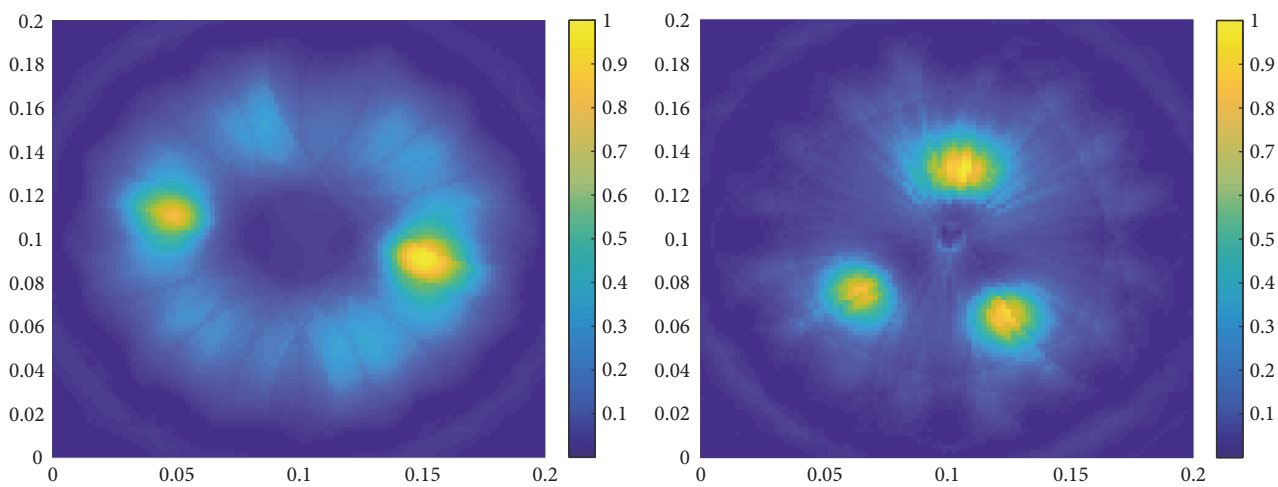

(a) Double-circle defect inversion imaging (b) Three-circle defect inversion imaging

Figure 12

interface inside the polymer-modified wood, the type, location, shape, and quantity of internal defects imaging of the polymer-modified wood were recognized according to the differences in the amplitude and speed of electromagnetic wave propagation inside different media. The scheme verified the feasibility of the total focusing method proposed in this paper to realize the inversion imaging of polymer-modified wood internal defects. The experimental results showed that the gprMax software can correctly simulate the polymer material and internal defects. The numerical results can be used for inversion imaging. The scattering intensity of metal defects on electromagnetic waves was large. Accurate defect images can be directly obtained in the inversion calculation of the total focusing method, but for air-based defects, the intensity of the scattered field at the interface was much smaller than the intensity of the direct wave, resulting in a bright spot stronger than the defect at the array element in the inversion image. After the direct wave data at each dot matrix was zeroed, the in-focus image inversion was significantly improved to achieve accurate detection of defective images. In this paper, using electromagnetic wave technology to carry out forward modeling and inversion imaging calculation of polymer-modified wood internal defects, the purpose of nondestructive testing of polymer-modified wood internal defects was realized. The method was simple in operation and fast in imaging calculation. It can provide a basis for the detection of internal defects in other types of polymer products or materials.

Data Availability

The data used to support the findings of this study are available from the corresponding author upon request.

Conflicts of Interest

The authors declare that they have no conflicts of interest.

Acknowledgments

This work was funded by the National Key Research and Development Program (Grant No. 2017YFD0600101), the China Postdoctoral Science Foundation (Grant No. 2018M640288), and the Heilongjiang Postdoctoral Fund (Grant No. LBH-Z18004).

References

[1] M. Gaff, M. Babiak, and F. Kacik, "Plasticity properties of thermally modified timber in bending – the effect of chemical changes during modification of European oak and Norway spruce," *Composites Part B: Engineering*, vol. 165, pp. 613–625, 2019.

[2] X. Wei, D. Tao, X. Sheng, and M. Zhang, "Modification of poplar wood using polyhexahydrotriazine and its effect on hygroscopicity," *Journal of Wood Chemistry and Technology*, vol. 38, no. 3, pp. 214–223, 2018.

[3] K. Peeters, E. Larnøy, A. Kutnar, and C. A. S. Hill, "An examination of the potential for the use of the Maillard reaction to modify wood," *International Wood Products Journal*, vol. 9, no. 3, pp. 108–114, 2018.

[4] A. Bastani, S. Adamopoulos, and H. Militz, "Shear strength of furfurylated, N-methylol melamine and thermally modified wood bonded with three conventional adhesives," *Wood Material Science and Engineering*, vol. 12, no. 4, pp. 236–241, 2017.

[5] M. Ghorbani, A. Nikkhah Shahmirzadi, and S. M. Amininasab, "Physical and Morphological Properties of Combined Treated Wood Polymer Composites by Maleic Anhydride and Methyl Methacrylate," *Journal of Wood Chemistry and Technology*, vol. 37, no. 6, pp. 443–450, 2017.

[6] M. Altgen, S. Adamopoulos, and H. Militz, "Wood defects during industrial-scale production of thermally modified Norway spruce and Scots pine," *Wood Material Science and Engineering*, vol. 12, no. 1, pp. 14–23, 2017.

[7] J. Laviada, B. Wu, M. T. Ghasr, and R. Zoughi, "Nondestructive evaluation of microwave-penetrable pipes by synthetic aperture imaging enhanced by full-wave field propagation model," *IEEE Transactions on Instrumentation and Measurement*, vol. 68, no. 4, pp. 1112–1119, 2019.

[8] V. A. Zorin, N. I. Baurova, and E. A. Kosenko, "Detection of defects in components made of dispersion-filled polymeric materials by the method of infrared thermography," *Polymer Science - Series D*, vol. 10, no. 3, pp. 241–243, 2017.

[9] E. Schneider and C. Boller, "Ultrasonic material characterization and testing of anisotropic components," in *Innovative Design and Development Practices in Aerospace and Automotive Engineering*, vol. 14, pp. 5-6, 2016.

[10] Z. Li, A. D. Haigh, M. N. Saleh et al., "Detection of impact damage in carbon fiber composites using an electromagnetic sensor," *Research in Nondestructive Evaluation*, vol. 29, pp. 123–142, 2018.

[11] I. P. Shcherbakov, V. I. Vettegren, R. I. Mamalimov, and K. F. Makhmudov, "The influence of stress on electron emission initiated by a shock wave from a heterogeneous material (granite)," *Physics of the Solid State*, vol. 59, no. 3, pp. 575–577, 2017.

[12] S. Guo, S. Chen, L. Zhang, Y. F. Chen, and K. Yao, "Plastic strain determination with nonlinear ultrasonic waves using in situ integrated piezoelectric ultrasonic transducers," *IEEE Transactions on Ultrasonics, Ferroelectrics and Frequency Control*, vol. 65, no. 1, pp. 95–101, 2018.

[13] Y.-I. Hwang, J. Park, and H.-J. Kim, "Performance comparison of ultrasonic focusing techniques for phased array ultrasonic inspection of dissimilar metal welds," *International Journal of Precision Engineering and Manufacturing*, vol. 20, pp. 525–534, 2019.

[14] W. Jiangfei, Y. Lihua, Z. Zhengguang, and Y. Mingyuan, "Accurate detection of a defective area by adopting a divide and conquer strategy in infrared thermal imaging measurement," *Journal of the Korean Physical Society*, vol. 73, pp. 1644–1649, 2018.

[15] N.-S. Kwak, J.-Y. Kim, and J.-C. Gao, "Detection of small-flaw in carbon brake disc (C-C) using air-coupled ultrasonic C-scan technique," *International Journal of Precision Engineering and Manufacturing*, vol. 18, pp. 987–994, 2017.

[16] R. B. Roy, A. Ghosh, S. Bhattacharyya et al., "Weld defect identification in friction stir welding through optimized wavelet transformation of signals and validation through X-ray micro-CT scan," *The International Journal of Advanced Manufacturing Technology*, vol. 99, pp. 623–633, 2018.

[17] Y. Jiang and S. Yin, "Recursive total principle component regression based fault detection and its application to vehicular cyber-physical systems," *IEEE Transactions on Industrial Informatics*, vol. 14, no. 4, pp. 1415–1423, 2018.

[18] A. Muller, B. Robertson-Welsh, P. Gaydecki, M. Gresil, and C. Soutis, "Structural health monitoring using lamb wave reflections and total focusing method for image reconstruction," *Applied Composite Materials*, vol. 24, no. 2, pp. 553–573, 2017.

[19] Holmes C., B. W. Drinkwater, and P. D. Wilcox, "Post-processing of the full matrix of ultrasonic transmit-receive array data for non-destructive evaluation," *NDT&E International*, vol. 38, pp. 701–711, 2005.

[20] J. zhang, B. W. Drinkwater, and D. Paul, "Defect detection using ultrasonic arrays: the multi-mode total focusing method," *NDT and E International*, vol. 43, pp. 123–133, 2010.

[21] H. Zhou, L. Sun, Y. Yang et al., "Reduction of electric field strength by two species of trees under power transmission lines," *Journal of Forestry Research*, vol. 29, no. 5, pp. 1415–1422, 2018.

[22] H. Zhou, L. Ma, L. Sun, H. Zhou, D. Liu, and L. Cai, "Impact moderation of power transmission lines on the environment by the shielding of trees," *BioResources*, vol. 13, no. 4, pp. 8239–8250, 2018.

Hindawi
Advances in Polymer Technology
Volume 2019, Article ID 8697047, 7 pages
https://doi.org/10.1155/2019/8697047

Research Article

Development of Eco-Friendly Soy Meal Adhesives Enhanced by Ethylene Glycol Diglycidyl Ether

Xingfang Yao,[1] **Hongli Liu**,[1] **and Congcong Li**[2]

[1]*School of Materials Science and Engineering, Tianjin Chengjian University, 26 Jinjing Road, Tianjin 300384, China*
[2]*MOE Key Laboratory of Wooden Material Science and Application, Beijing Forestry University, Beijing 100083, China*

Correspondence should be addressed to Xingfang Yao; yaoxingfang77@126.com and Hongli Liu; lhlbh@163.com

Received 31 December 2018; Accepted 13 February 2019; Published 9 June 2019

Guest Editor: Changlei Xia

The ethylene glycol diglycidyl ether (EGDE) as a viscosity reducer, plasticizing agent, and crosslinking agent was introduced into the adhesive system to improve the properties of the soy-based adhesive. The adhesive properties including viscosity, solid content, and shear adhesion of soy protein adhesive were measured. The morphology, infrared spectra, and crystallinity of the cured adhesives were evaluated with scanning electron microscopy (SEM), Fourier transform infrared (FTIR), and X-ray diffraction (XRD). The results showed that the viscosity of soybean flour (SF) adhesive was reduced by 48% and the solid content increased from 25.9% to 31.7% with the addition of 10 wt% EGDE. The wet shear strength of the plywood bonded by EGDE-modified SF adhesive was significantly improved owing to the formation of crosslinking structure in the adhesive system. The SEM, FTIR, and XRD results demonstrated that the crosslinking reaction among epoxy group of EGDE, the amino group of SF, and the hydroxyl groups of polyvinyl alcohol occurred successfully during the curing process.

1. Introduction

Soy-based adhesives were developed in 1923 and widely used in commercial production of plywood between 1930s and 1960s, but later they were placed by petroleum-based adhesives owing to the poor adhesion property and water resistance [1, 2]. In recent years, however, the dwindling of fossil resources and the growing concerns about the pollution of petroleum-based adhesives have been driving the development of renewable and eco-friendly materials [3, 4]. Soybean is considered as an alternative because of its abundance, low cost, operability, renewability, and environment friendliness [5–9]. It is necessary to modify the soy-based adhesives to obtain the desired adhesion properties. Crosslinking is one major acceptable modification method [10]. The introduction of a crosslinking agent allows the soy proteins to form a three-dimensional network structure, thus improving the adhesion properties of soy-based adhesives.

Soybean flour (SF) is mainly a mixture of soy proteins and carbohydrates containing many polar functional groups, such as -OH, -NH_2, -COOH, and -SH [5, 10]. Thus, many chemicals can be used as a crosslinking agent for soy-based adhesives such as the chemicals with epoxy group [11, 12]. The glycerol polyglycidyl ether (GPE) is an effective crosslinking agent for bonding yellow poplar plywood, which meets the requirement for interior plywood [13]. Supporting evidence shows that glycidyl methacrylate (GMA) can successfully graft onto soy protein isolate (SPI) [14] and enzyme-treated soybean meal adhesives. Epoxy resin (EPR) can react with the amine group in soy protein and thus improve the water resistance of soy-based adhesives [10, 15]. The improved mechanical properties of soy-based bioplastic and pineapple leaf fiber 'Green' composites are attributed to the interaction between hydroxyl groups in the pineapple leaf and the epoxy groups in polyester amide grafted with glycidyl methacrylate [16].

Many efforts have been done to improve the adhesion strength and viscosity of soy-based adhesives. Polyethylene glycol (PEG) can reduce the viscosity of soy-based adhesive, which is against the shear strength owing to the lack of reactive functional groups. Polyethylene glycol diacrylate (PEGDA) was introduced as a crosslinker and viscosity reducer into the soybean adhesive system for the formation of interpenetrating networks (IPNs) in situ. The shear strength

could not be significantly improved because of the hydrophobicity of IPNs.

The ethylene glycol diglycidyl ether (EGDE) with two epoxy groups is prepared from the reaction between ethylene glycol (EG) and epichlorohydrin (ECH) and is widely used in the chemical industry. Previous studies prove that EGDE can be used as a crosslinking agent [17, 18]. EGDE was used as a crosslinking agent for crosslinking chitosan beads, which were then insoluble in acidic and basic media [19]. In the present study, EGDE as a viscosity reducer and crosslinker was introduced into the soy flour (SF) adhesive system. The viscosity, solid content, shear adhesion, morphology, infrared spectra, and crystallinity were evaluated to investigate the effects of EGDE on the adhesion property and water resistance of SF adhesives.

2. Materials and Methods

2.1. Materials. The SF with protein content of 45.2% and moisture content of 5% was obtained from Sanhe Hopefull Group Oil Grain Food Co. Ltd. Poplar veneer with a thickness of 1.6 mm and moisture content of 8% was purchased from Wen'an county of Hebei province, China. Polyvinyl alcohol (PVA) was purchased from Beijing Chemical Reagents Co. The EGDE was obtained from Chuzhou Hui-Sheng Electronic Material Co., Ltd.

2.2. Preparation of SF Adhesives. The SF (25 g) was suspended in the mixture of PVA solution (40 g, 5%) and tap water (35 g) at room temperature and then stirred to form a homogeneous system. Finally, the different amounts of EGDE based on weight of the adhesive were added to the above mixture and mixed uniformly.

2.3. Determination of Viscosity. The viscosity of SF adhesive was determined using a DV-II+ viscometer (Brookfield Engineering Laboratories, Middleboro, MA, USA). The viscosity was measured at room temperature and the reported values are the average of three replications.

2.4. Solid Content Measurement. The solid content was measured by using an oven-drying method. About 2 g (weight α) of the adhesive was placed into an oven with the temperature set to 100±2°C for drying until a constant weight (weight β) was obtained. The value of the solid content was calculated with the following equation. The final solid content was the average of the value of three parallel samples.

$$\text{Solid content } (\%) = \frac{\beta(g)}{\alpha(g)} \times 100 \quad (1)$$

2.5. Preparation of Plywood Samples. The adhesive was brushed uniformly onto one side of a piece of poplar veneer surface with dimensions of 400mm × 400 mm (length × width) in order to evaluate its property. The adhesive spread rate was between 180 and 200 g/m^2. Before being sent into the press, the three-layer plywood sample was assembled by hand. Then the assembled plywood was hot-pressed at 120°C and 1.0 MPa for 6 min.

2.6. Test of Shear Strength of Plywood Samples. After being stored at ambient conditions for at least 24 h, the three-layer plywood was cut into shear specimens with a dimension of 100 mm × 25 mm for evaluation of its shear strength and water resistance. The bonded area of each specimen was 25 mm × 25 mm. The testing method was in accordance with the procedure described in the China National Standard Plywood-Part 3: General Specification for Plywood for General Use (GB/T 9846.3-2004). For type I plywood, the eight plywood specimens of each plywood panel were firstly soaked in boiling water for 4 h, then dried in 63°C for 20 h, and lastly reapplied in boiling water for another 4 h. For type II plywood, the same number of specimens was soaked in 63°C tap water for 3 h. For both type I and type II plywood, all of the specimens were taken out of water and cooled at room temperature for 10 min before testing the shear strength. The wet shear strength was measured by using a common tensile machine with a cross head speed of 10.0 mm/min. The average bonding strength was reported.

2.7. Scanning Electron Microscopy (SEM) Testing. The unmodified and modified SF adhesives samples were dried in an oven at 120±2°C until a constant weight was obtained. The microstructure of the adhesive was observed by a Hitachi S-3400 N (Hitachi Science System, Ibaraki, Japan) SEM. The cured adhesives were affixed to an aluminum stub with double-side adhesive tape and the surface was sputter-coated with gold before being examined under the microscope. The SEM images of the adhesives were obtained with operation conditions at an accelerating voltage of 15kV.

2.8. Fourier Transform Infrared (FTIR) Spectroscopy. The oven was preheated to 120°C and then the SF adhesives with or without EGDE were placed in the oven to a constant weight and then ground into power. The FTIR spectra of the adhesives were recorded on a Nicolet 380 spectrometer (Nicolet Instrument Corporation, Madison, WI) over the range of 400 to 4000 cm^{-1} with a 4 cm^{-1} resolution and 32 scans.

2.9. X-Ray Diffraction (XRD). The specimens were prepared as mentioned earlier. The X-ray diffraction (XRD) spectrum investigations were recorded with a XRD diffractometer (D8, Advance, Bruker, Germany) composed of a cobalt source. The scan range was from 5° to 60° (2θ) with 2°/min of scanning speed at 45 KV, 30 mA.

2.10. Thermogravimetric (TG) Analysis. Thermal degradation patterns of the cured unmodified and EGDE-modified SF adhesive were studied using a TGA analysis (TGA Q50, TA instruments, USA) in a nitrogen atmosphere. The adhesives were cured at 120°C in a vacuum until the constant weight was obtained and ground. Then the ground powder was put into a platinum cup and scanned from the room temperature to 600°C at a heating rate of 10°C/min. Maximum degradation rate was calculated as mass (%) at peak temperature divided by peak temperature.

Table 1: Effects of EGDE dosage on the performance of SF adhesive and SF adhesive-based plywood.

Sample	EGDE dosage (wt%)	Viscosity (cP)	Solid content (%)	Dry shear strength (MPa)	Wet shear strength (MPa)	
					63°C[b]	100°C[c]
A	0	102000±6245	25.9±0.2	1.24±0.12 CWF[a]	0.40±0.03	--[d]
B	2	99000±9539	27.7±0.3	1.47±0.11 CWF	0.76±0.05	0.33±0.04
C	4	75000±4583	28.9±0.3	1.39±0.30 CWF	0.82±0.05	0.42±0.02
D	6	66000±7937	30.2±0.1	1.62±0.10 CWF	0.96±0.04	0.50±0.03
E	8	60000±6557	30.9±0.1	1.51±0.21 CWF	1.06±0.02	0.54±0.03
F	10	53000±3606	31.7±0.5	1.39±0.38 CWF	0.81±0.01	0.49±0.01

[a] CWF: 100% cohesive wood failure.
[b] The results from type II.
[c] The results from type I.
[d] Delamination.

3. Results and Discussion

3.1. Viscosity Analysis. Viscosity is one major physical property that determines the adhesive behavior. The high viscosity will lead to poor wettability and thus the adhesive cannot spread evenly on the surface of wood veneer during the hot-pressed procedure. In other words, an appropriate viscosity makes the adhesives more uniform during hot pressing and increases the spread area of wood veneer and adhesives. The viscosity of EGDE-modified SF adhesive decreased with the increasing dosage of EGDE (Table 1). The viscosity was reduced slightly along with the dosage increasing from 0 to 2 wt% EGDE, but after 4 wt% EGDE, the viscosity was reduced by 26% from 102000 to 75000 cP. With the further increased dosage of EGDE, the viscosity continued to decrease. On the addition of 10 wt%, the viscosity was reduced by 48% to 53000 cP. These results indicate that EGDE could be used as a viscosity reducer for the SF adhesive. EGDE was incorporated as a plasticizer and decreased the intermolecular interactions, molecular entanglements, and friction when SF was dissolved in water, thus reducing the viscosity.

3.2. Solid Content Analysis. The experimental results showed that the lower viscosity and the higher solid content resulted in higher wet shear strength [20]. At low solid content, a longer hot-pressed cycle was needed to remove the superfluous water from the adhesives during the hot-pressed process. The solid content continued to rise with the increased EGDE dosage in Table 1. The solid content of the unmodified SF adhesive was only 25.9%, which was not suitable for the hot-pressed process since more than 70% of water in the adhesive should be removed. After addition of 6 wt% EGDE, the solid content of the modified SF adhesive already reached 30.2%.

3.3. Dry Shear Strength. The dry shear strength for both unmodified and EGDE-modified SF adhesive-based plywood specimens met the requirement of Chinese national standard (GB/T 9846.3-2004, ⩾0.7 MPa) (Table 1). However, the wood failure was 100% for almost all of the specimens. Thus, the measured value was determined by the strength of poplar veneer, and it was unable to demonstrate the effect of EGDE on the dry shear strength of the plywood.

3.4. Water Resistance. Water resistance is an important property related to wood adhesion [2]. Table 1 shows the wet shear strength of plywood bonded by different adhesives. After the 3 h soaking in the 63°C tap water, the wet shear strength was improved significantly at first with EGDE dosage of 2-8 wt%, but decreased with further increase of EGDE dosage. When the dosage was 2 wt%, the wet shear strength was increased by 90% from 0.40 to 0.76 MPa, which well satisfied the national standard for type II plywood (≥0.70 MPa). With addition of 8 wt% EGDE, the wet shear strength of plywood was maximized to 1.06 MPa, which indicates that the water resistance was improved by adding a certain amount of EGDE. We deduced that the hydrophilic groups in the SF adhesive system were reduced in amount or hidden with the incorporation of EGDE during the curing process.

All of the unmodified SF adhesive-based plywood specimens failed in the 28 h boiling-dry cycle, while the EGDE-modified SF adhesive survived the cycle and yielded wet shear strength of 0.54 MPa with addition of 8 wt% EGDE (Table 1). The results indicate that EGDE improved the water resistance of the EGDE-modified SF adhesive-based plywood. However, no adhesive satisfied the Chinese national standard for type I plywood (≥0.70 MPa).

Two reasons account for the improvement of the shear strength of modified SF adhesive. First, EGDE used as a crosslinking agent was introduced into the system to form a 3D network structure and, thus, significantly increased the shear strength. However, the wet shear strength was reduced with further addition of EGDE, which resulted from the hydrophilicity of excessive EGDE. Second, EGDE also acted as a plasticizing agent in this system. In general, the water evaporation leads to the reduced flowability of SF adhesive during the hot-press process. However, the incorporation of EGDE positively affected the dispersivity and leveling of SF adhesive on the surface of the poplar veneer, and then improved the adhesion property. The reaction scheme between EGDE and SF adhesive is shown in Figure 1. Each end of the molecular chain of EGDE contained an epoxy group that reacted with the amine group of soy protein. Meanwhile, the epoxy group of EGDE reacted with the hydroxyl group of PVA. Then the macromolecular structure was formed by the crosslinking reaction, which may cause the improvement of dry and wet shear strengths.

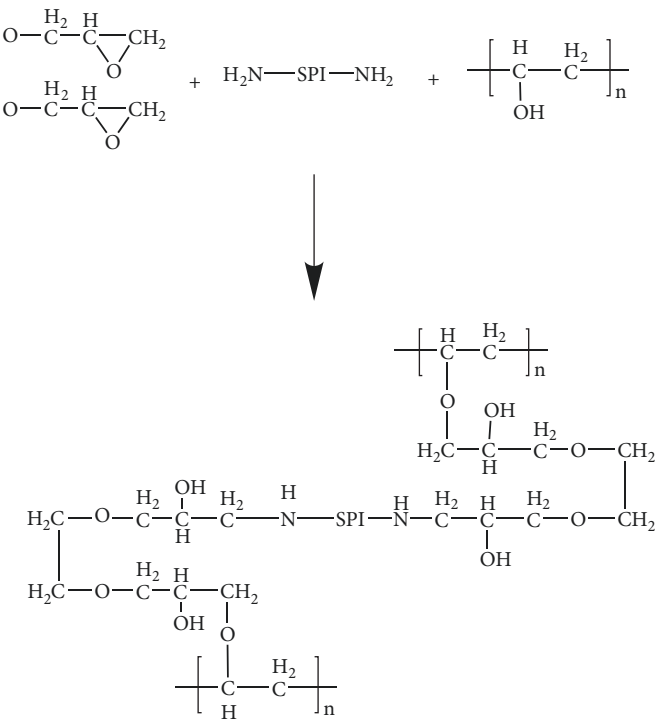

Figure 1: The interaction among EGDE, SF, and PVA.

3.5. SEM Analysis. The micrographs of cured adhesives are presented in Figure 2. Many holes and cracks appeared on the fractured surface of the cured unmodified SF adhesive, which were caused by the water gasification in the adhesive during the hot pressing (Figure 2(a)) (Gao et al., 2012). Therefore, the wet shear strength was poor. After the incorporation of EGDE, the micrographs showed fewer holes or cracks than the unmodified ones, indicating that EGDE alleviated the water gasification during the curing process (Figure 2(b)). With the EGDE dosage being further increased, the surface became more and more smooth (Figures 2(b)–2(f)). Table 1 clearly shows that a higher EGDE dosage leads to more crosslinking reactions with soy protein and PVA.

3.6. FTIR Spectroscopic Analysis. The FTIR spectra of cured SF adhesive and EGDE-modified SF adhesive are given in Figure 3. For SF adhesive without addition of EGDE (Figure 3(a)), the broad band within 3000 to 3500 cm^{-1} was assigned to the free and bound N-H and O-H groups. The protein characteristic absorption bands at 1655 cm^{-1} (amide I), 1535 cm^{-1} (amide II), and 1239 cm^{-1} (amide III) were related to C=O stretching, N-H bending, C-N stretching, and N-H bending vibration, respectively [21]. Moreover, the absorption band at 1053 cm^{-1} resulted from -C-NH stretching. The absorption band at 2872 cm^{-1} (Figures 3(b) and 3(c)) was stronger than that of SF adhesive (Figure 3(a)), which might result from the increasing content of $-CH_2$ with the addition of EGDE. The main difference between the spectra of SF adhesives with or without EGDE lied in the absorption band at 1074 cm^{-1}, which was assigned to C-O-C stretching resulting from aliphatic ethers after the incorporation of EGDE. Also, the absorption band at 1404 cm^{-1} resulted from C-N stretching. However, the epoxy bond was not revealed in the spectra of 6 wt% EGDE-modified SF adhesive, indicating that the interaction among EGDE, SF, and PVA occurred during the curing process. As the dosage of EGDE increased to 10 wt%, no absorption band of epoxy group was observed probably because of the low EGDE content.

3.7. XRD Analysis. Figure 4 presents the XRD patterns of the unmodified and EGDE-modified SF adhesives. For the unmodified SF adhesive, there are two peaks around 2θ=9.5° and 20.4° due to the presence of PVA [22]. With the incorporation of EGDE, the peak at 2θ=9.5° was weakened and even disappeared with the increased dosage of EGDE. The crystallinity test results of all adhesives are shown in Table 2. The crystallinity increased from 18.8% to 21.6% when the EGDE dosage was 0-6 wt%, but slightly reduced with further addition of EGDE, because the crosslinking effect limited the rearrangement of the molecular chains. This evidence further confirmed that crosslinking interaction occurred in the adhesive system.

3.8. TGA Analysis. The TGA and differential TGA (dTG) curves of cured unmodified and EGDE-modified SF adhesives are shown in Figure 5. The weight loss of both types of adhesives degraded in three stages. In the first stage from 29 to 120°C, about 5% weight was lost owing to the loss of residual moisture [23]. In the second stage between 190 and 400°C, the weight loss was due to the degradation of soy proteins which involved the breakage of inter- and intramolecular hydrogen bond and electrostatic bond, and the cleavage of covalent shearing between the peptide bonds of amino acid residues.

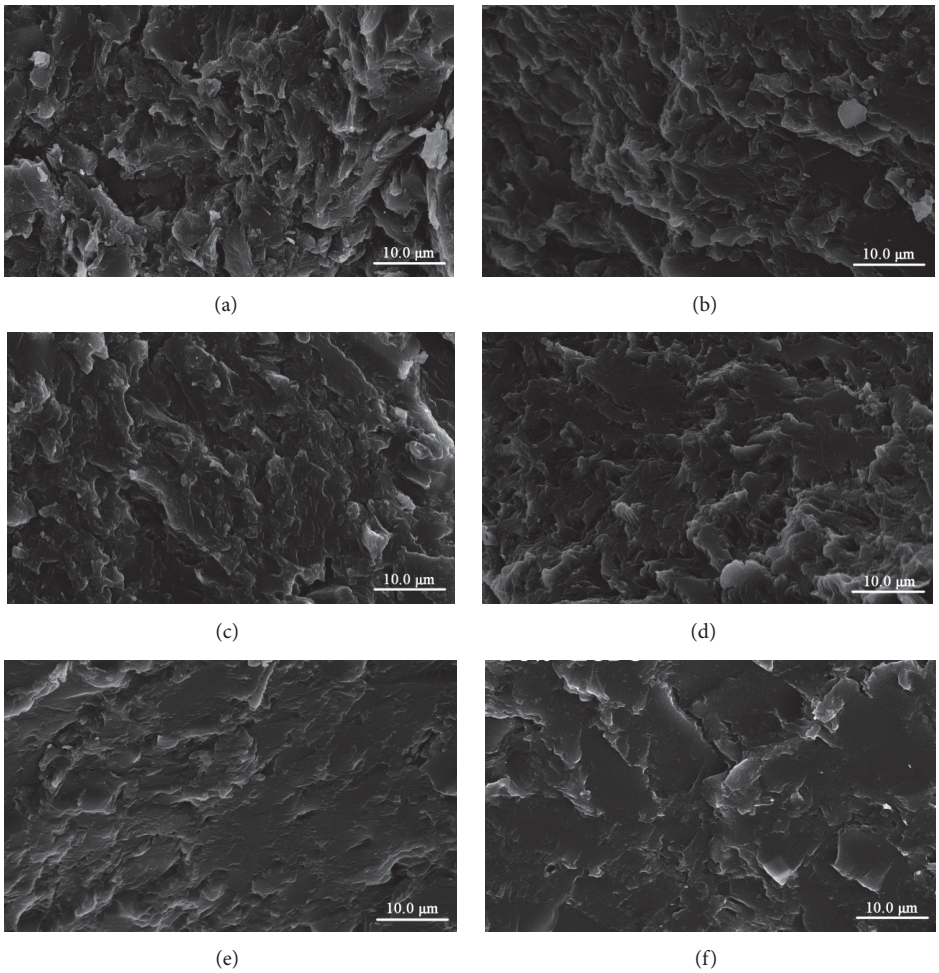

Figure 2: SEM micrographs of fracture surface of cured EGDE/SF adhesives.

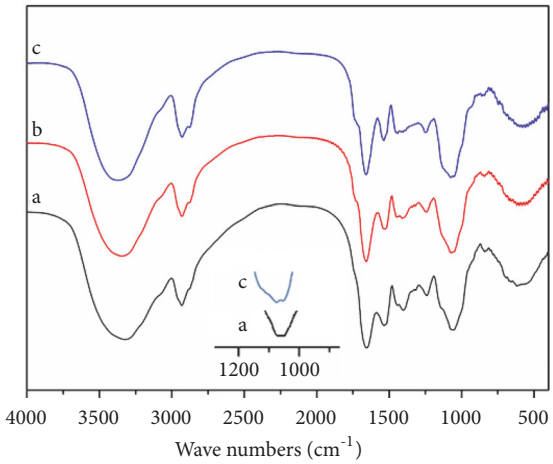

Figure 3: FTIR spectra of EGDE/SF adhesives: (a) A; (b) D; (c) F.

In the last stage, further heating led to the breakage of S-S, O-N, and O-O and finally to the decomposition of protein backbone peptide bonds, thus producing various gases such as CO, CO_2, NH_3, and H_2S [20, 24].

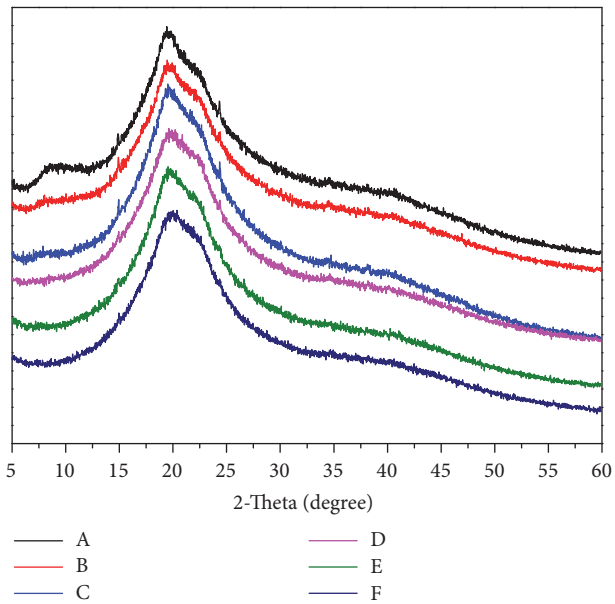

Figure 4: XRD diffraction patterns of unmodified and EGDE-modified SF adhesives.

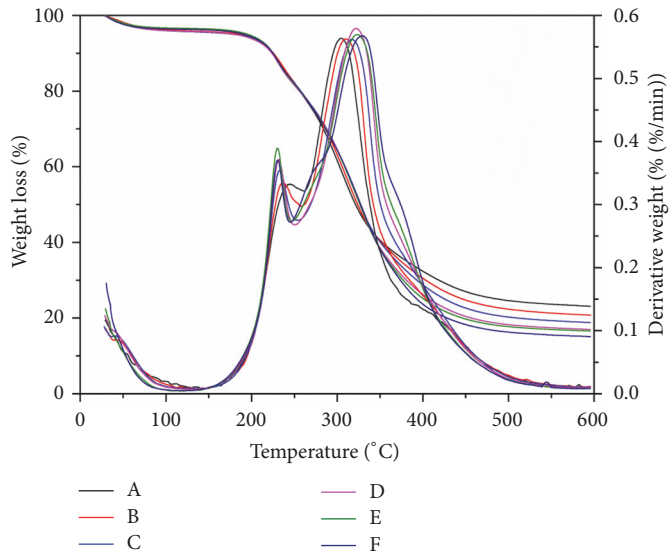

Figure 5: The TGA and dTG curves of cured unmodified and EGDE-modified SF adhesives.

Table 2: The crystallinity of unmodified and EGDE-modified SF adhesives.

Sample	A	B	C	D	E	F
Crystallinity (%)	18.80	20.13	21.17	21.68	21.57	21.45

Table 3: Thermal analysis of unmodified and EGDE-modified SF adhesives.

Sample	T_i	T_m^a	T_m^b	T_d				RW% at 600°C
				20%	40%	60%	80%	
A	208	245	305	256	303	353	--	23.1
B	206	237	310	257	306	352	--	20.8
C	205	233	317	256	309	350	511	18.8
D	203	232	322	256	309	346	457	17.0
E	201	230	323	257	309	346	446	16.6
F	201	233	329	257	309	346	428	15.1

The results of initial degradation temperature (T_i), maximum pyrolysis temperature (T_m), decomposition temperature with varying weight loss (T_d), and residual weight (RW %) of unmodified and modified SF adhesives are shown in Table 3. The T_i and T_m^a of the unmodified samples were slightly higher than in the modified ones. The main peak degradation temperature (T_m^b) of modified adhesive was higher than that of the unmodified ones and T_m^b increased from 305 to 329°C with the increasing dosage of EGDE increasing, probably because the crosslinking reaction among EGDE, SF, and PVA resulted in dense macromolecular structure and higher thermal stability. T_d values were similar between the modified and the unmodified SF adhesives. R_w was higher in the unmodified SF adhesive and decreased upon the addition of EGDE.

4. Conclusions

(1) With the incorporation of EGDE, the viscosity of SF adhesive obviously decreased and the solid content increased.

(2) The water resistance of plywood bonded by EGDE-modified SF adhesive was improved significantly compared with the unmodified SF adhesive. In addition, the water resistance of 8 wt% EGDE-modified SF adhesive was the highest, and it increased by 165% from 0.40 to 1.06MPa, which met the Chinese national standard for type II plywood but not the type I plywood standard.

(3) SEM, FTIR, XRD, and TG suggest that the crosslinking reaction among EGDE, SF, and PVA occurred successfully during the curing process.

Data Availability

The data used to support the findings of this study are available from the corresponding author upon request.

Conflicts of Interest

The authors declare that they have no conflicts of interest.

Acknowledgments

This work was financially supported by the Fundamental Research Funds for the Central Universities (NO. 2016ZCQ01).

References

[1] H.-N. Xu, S. Ma, W. Lv, and Z. Wang, "Soy protein adhesives improved by SiO_2 nanoparticles for plywoods," *Pigment & Resin Technology*, vol. 40, no. 3, pp. 191–195, 2011.

[2] S. Zhao, Z. Wang, H. Kang et al., "Fully bio-based soybean adhesive in situ cross-linked by interactive network skeleton from plant oil-anchored fiber," *Industrial Crops and Products*, vol. 122, pp. 366–374, 2018.

[3] N. Chen, P. Zheng, Q. Zeng, Q. Lin, and J. Rao, "Characterization and performance of soy-based adhesives cured with epoxy resin," *Polymer*, vol. 9, no. 10, 2017.

[4] Q. Zeng, Q. Lu, Y. Zhou, N. Chen, J. Rao, and M. Fan, "Circular development of recycled natural fibers from medium density fiberboard wastes," *Journal of Cleaner Production*, vol. 202, pp. 456–464, 2018.

[5] Z. Zhong, X. S. Sun, and D. Wang, "Isoelectric pH of polyamide-epichlorohydrin modified soy protein improved water resistance and adhesion properties," *Journal of Applied Polymer Science*, vol. 103, no. 4, pp. 2261–2270, 2007.

[6] Y. Chen and L. Zhang, "Blend membranes prepared from cellulose and soy protein isolate in NaOH/thiourea aqueous solution," *Journal of Applied Polymer Science*, vol. 94, no. 2, pp. 748–757, 2004.

[7] G. A. Amaral-Labat, A. Pizzi, A. R. Gonçalves, A. Celzard, S. Rigolet, and G. J. M. Rocha, "Environment-friendly soy flour-based resins without formaldehyde," *Journal of Applied Polymer Science*, vol. 108, no. 1, pp. 624–632, 2008.

[8] Y. Zhang, Y. Li, V. K. Thakur, Z. Gao, J. Gu, and M. R. Kessler, "High-performance thermosets with tailored properties derived from methacrylated eugenol and epoxy-based vinyl ester," *Polymer International*, vol. 67, no. 5, pp. 544–549, 2018.

[9] Y. Zhang, V. K. Thakur, Y. Li et al., "Soybean-oil-based thermosetting resins with methacrylated vanillyl alcohol as bio-based, low-viscosity comonomer," *Macromolecular Materials and Engineering*, vol. 303, no. 1, 2018.

[10] H. Lei, G. Du, Z. Wu, X. Xi, and Z. Dong, "Cross-linked soy-based wood adhesives for plywood," *International Journal of Adhesion and Adhesives*, vol. 50, pp. 199–203, 2014.

[11] Y. Jang, J. Huang, and K. Li, "A new formaldehyde-free wood adhesive from renewable materials," *International Journal of Adhesion and Adhesives*, vol. 31, no. 7, pp. 754–759, 2011.

[12] C. May, *Epoxy Resins: Chemistry And Technology*, CRC Press, Boca Raton, Fla, USA, 1987.

[13] J. Huang, C. Li, and K. Li, "A new soy flour-polyepoxide adhesive system for making interior plywood," *Holzforschung*, vol. 66, no. 4, pp. 427–431, 2012.

[14] T. Li, N. Wang, and Q. Fang, "Incorporation of modified soy protein isolate as filier in BR/SBR blends," *Journal of Materials Science*, vol. 45, no. 7, pp. 1904–1911, 2010.

[15] C. Xia, L. Wang, Y. Dong et al., "Soy protein isolate-based films cross-linked by epoxidized soybean oil," *RSC Advances*, vol. 5, no. 101, pp. 82765–82771, 2015.

[16] W. Liu, M. Misra, P. Askeland, L. T. Drzal, and A. K. Mohanty, "'Green' composites from soy based plastic and pineapple leaf fiber: fabrication and properties evaluation," *Polymer*, vol. 46, no. 8, pp. 2710–2721, 2005.

[17] X. Lu, Y. Xu, C. Zheng, G. Zhang, and Z. Su, "Ethylene glycol diglycidyl ether as a protein cross-linker: A case study for cross-linking of hemoglobin," *Journal of Chemical Technology and Biotechnology*, vol. 81, no. 5, pp. 767–775, 2006.

[18] M. Eguchi, Y.-Z. Du, Y. Ogawa, T. Okada, N. Yumoto, and M. Kodaka, "Effects of conditions for preparing nanoparticles composed of aminoethylcarbamoyl-β-cyclodextrin and ethylene glycol diglycidyl ether on trap efficiency of a guest molecule," *International Journal of Pharmaceutics*, vol. 311, no. 1-2, pp. 215–222, 2006.

[19] W. S. Wan Ngah, C. S. Endud, and R. Mayanar, "Removal of copper(II) ions from aqueous solution onto chitosan and cross-linked chitosan beads," *Reactive & Functional Polymers*, vol. 50, no. 2, pp. 181–190, 2002.

[20] Z. Qin, Q. Gao, S. Zhang, and J. Li, "Glycidyl methacrylate grafted onto enzyme-treated soybean meal adhesive with improved wet shear strength," *Bioresources*, vol. 8, no. 4, pp. 5369–5379, 2013.

[21] A. Fried and D. Richter, *Infrared Absorption Spectroscopy*, Blackwell Publishing, Oxford, UK, 2006.

[22] K. Nakane, T. Yamashita, K. Iwakura, and F. Suzuki, "Properties and structure of poly(vinyl alcohol)/silica composites," *Journal of Applied Polymer Science*, vol. 74, no. 1, pp. 133–138, 1999.

[23] G. Qi and X. S. Sun, "Soy protein adhesive blends with synthetic latex on wood veneer," *Journal of the American Oil Chemists' Society*, vol. 88, no. 2, pp. 271–281, 2011.

[24] A. Moure, J. Sineiro, H. Domínguez, and J. C. Parajó, "Functionality of oilseed protein products: a review," *Food Research International*, vol. 39, no. 9, pp. 945–963, 2006.

Hindawi
Advances in Polymer Technology
Volume 2019, Article ID 4949786, 7 pages
https://doi.org/10.1155/2019/4949786

Research Article

The Influence of Heat Treatment on the Static and Dynamic Sorptive Behavior of Moso Bamboo (*Phyllostachys pubescens*)

Yuxiang Huang, Ru Liu, Fandan Meng, Yanglun Yu, and Wenji Yu

Key Laboratory of Wood Science and Technology of State Forestry Administration, Research Institute of Wood Industry, Chinese Academy of Forestry, Xiangshan Road, Haidian District, Beijing 100091, China

Correspondence should be addressed to Yanglun Yu; yuyanglun@caf.ac.cn

Received 4 January 2019; Revised 2 April 2019; Accepted 4 April 2019; Published 2 May 2019

Guest Editor: Changlei Xia

The influence of heat treatment on moisture sorption behavior of moso bamboo (*Phyllostachys pubescens*), especially under dynamic sorption conditions, was investigated. Moso bamboo was heated to 180 and 200°C for 8 h to investigate the chemical components and sorptive behavior at sinusoidal relative humidity (RH) and constant humidity. The results of chemical components revealed that the content of holocellulose, α-cellulose, and hemicellulose decreased while that of lignin increased slightly with increasing treatment temperatures. The results of static adsorption at constant RH showed that 200°C treated bamboo exhibited the lowest moisture content and moisture sorption coefficient. The results of dynamic sorptive behavior indicated that the moisture content changed sinusoidally but lagged behind the triggering sinusoidal RH changes. Heat-treated bamboo presented greater phase lag and smaller amplitudes of moisture content and sorption hysteresis due to the hemicellulose removal.

1. Introduction

Bamboo, regarded as an attractive natural material in terms of strength and cost [1] due to its rapid growth, affordability, workability, and high mechanical resistance [2], is widely used in light building materials, fencing, scaffolding, and musical instruments [3]. In recent years, bamboo is developed to produce bamboo-based composites to improve its added value, such as bamboo plywood [4], laminated bamboo lumber [5, 6], bamboo particleboard [7], and bamboo fiber-reinforced polymer composite [8].

However, as is common with other bio-based materials, bamboo is susceptible to dimensional instability by being exposed to moisture or water due to its natural hygroscopicity, which greatly limited its application [9]. Heat treatment has been shown to be an effective way to improve the dimensional stability of wood and wood products and a great deal of research has been done on the heat treatment of wood [10–14]. These studies have showed that the cell wall components underwent thermal degradation during the heat treatment, which reduced the number of hydrophilic hydroxyl groups, thus increasing wood hydrophobicity. Recently, thermal modification technology has also been used to improve the bamboo properties by using heat treatment of wood as reference. Some relevant research has been carried out in the past in terms of heat treatment process [15], color change and dimensional stability [16], mechanical property change [1, 9, 16], and durability of heat treatment [17]. Their results showed that the heat treatment is a green and environmentally friendly modification method. With the help of heat conducting medium, the physical and chemical properties of bamboo can be modified by heat alone. The change of these properties was closely related to the process parameters such as temperature, time, and medium of heat treatment. The increase of heat treatment temperature and time led to the decrease of elastic modulus and flexural strength of bamboo [9, 16]. The bending strength of bamboo treated with 200°C decreased by 31-60% [3]. Wahab et al. found that the equilibrium moisture content of heat-treated bamboo was significantly lower than that of untreated bamboo and the lower moisture absorption led to better dimensional stability of bamboo [17]. The results by Azadeh and Ghavami also indicated that increasing the temperature and time exposure of heat treatment reduced the hygroscopic property of bamboo [2]. In terms of the hygroscopic properties of heat-treated bamboo, these studies

were carried out under static conditions with constant relative humidity (RH). However, in fact, when bamboo is utilized and processed, the RH is changing, which can be regarded as an approximate sinusoidal change [18]. Herein, the effects of heat treatment on the dynamic sorptive behavior at sinusoidal RH as well as its static sorptive behavior at constant RH were investigated, which is expected to contribute to a better control of moisture and dimensional stability of bamboo products in service.

2. Materials and Methods

2.1. Materials Preparation. Moso bamboo (*Phyllostachys pubescens L.*), aged 4 years, was harvested from the forest in Anji, Zhejiang. Its diameters ranged from 7-10 cm and culm-wall thickness was from 7 to 10 mm. The bamboo culm was sawn into small bamboo slivers with dimensions of 50 mm (length)× 20 mm (width) × 5 mm (thickness) after removing the inner and outer bamboo skin. The bamboo sliver was dried at 85°C for 24 h to an approximate moisture content of 10% in an oven. Then, the samples were kept in a conditioned room at 20°C and 50% relative humidity for 2 weeks.

2.2. Heat Treatment. The slivers were oven-dried at 103°C and weighed before the thermal treatment. The dried samples were placed in an iron bucket in an oven and heated at 180 and 200°C, respectively, for 8 h. Inspired by the chestnut roasted in sand with brown sugar, the bamboo samples were covered by sand as protecting medium, which can make the bamboo samples uniformly heated and avoid burning. The sand was passed through a 40 mm sieve, and any glass or stone pieces were manually removed to obtain a homogeneous mix prior to testing. Afterwards, the samples were taken out and washed with water and oven-dried again.

2.3. Chemical Components. The bamboo slivers before and after heat treatment were ground and passed through 40-60 mesh sieves prior to chemical analyses.

2.3.1. Holocellulose. The content of holocellulose was determined by GB/T 2677.10-1995. Firstly, benzene-ethanol ($C_8H_{10}O$) was used to extract the bamboo powders of 2 g (accurate to 0.0001 g). Then, the powder was infused with 65 mL distilled water and placed in 75°C water bath. The powders were treated with 0.5 mL acetic acid (CH_3COOH) and 0.6 g sodium chlorite ($NaClO_2$) per hour till they became white. After filtering and washing to neutrality, the mixture was washed three times with acetone and dried in an oven at 105 ± 2°C to reach a constant weight. The content of holocellulose was determined by

$$\text{The content of holocellulose (\%)} = \frac{m_1}{m_0} \times 100 \quad (1)$$

where m_0 (g) is the oven-dry weight of the sample and m_1 (g) is the oven-dry weight of the extracted holocellulose.

The aforementioned procedure was repeated; the arithmetic average value of the two measurements was taken as the result. The error between two measurements should not exceed 0.4%.

2.3.2. α-Cellulose Analysis. The content of α-cellulose was determined by GB/T 744-1989. 2 g (accurate to 0.0001 g) of oven-dried holocellulose obtained from Section 2.3.1 was mixed with 30 mL NaOH with a mass fraction of 17.5%. After placing in 25°C water bath for 45 min, the mixture was added with 30 mL distilled water and then it was filtered three times with 25 mL NaOH with a mass fraction of 9.5% and then washed again with 400 mL distilled water. Next, the residue was added with CH_3COOH and the system was kept for 5 min. Complete a vacuum filtration process to remove the acetic acid and wash the residue until the filtrate solution was no longer acidic. Finally, the residue was dried in an oven at 105 ± 2°C to reach a constant weight. The content of α-cellulose was calculated by

$$\text{The content of } \alpha - \text{cellulose (\%)} = \frac{m_1}{m_0/W_1} \times 100 \quad (2)$$

where m_0 (g) is the oven-dry weight of the extracted holocellulose, m_1 (g) is the oven-dry weight of the extracted α-cellulose, and W_1 (%) is the content of holocellulose.

The aforementioned procedure was repeated; the arithmetic average value of the two measurements was taken as the result. The error between two measurements should not exceed 0.4%.

2.3.3. Hemicelluloses. The content of hemicellulose of bamboo samples was estimated by the equation proposed by Zhao et al. [19].

$$\begin{aligned} &\text{the content of hemicellulose (\%)} \\ &\quad = \text{the content of holocellulose (\%)} \\ &\quad - \text{the content of } \alpha\text{-cellulose (\%)} \end{aligned} \quad (3)$$

2.3.4. Acid-Insoluble Lignin. The content of acid-insoluble lignin (lignin for short) was determined by GB/T 2677.8-1994. Firstly, $C_8H_{10}O$ was used to extract the bamboo powders of 1 g (accurate to 0.0001 g). After hydrolyzing with 15 mL sulphuric acid (H_2SO_4) with a mass fraction of 72%, the bamboo powders were place in a 20°C water bath for 2.5 h. Then, the mixture was added with distilled water until the total volume reached 560 mL and boiled at 100°C. During the period, the distilled water was continuously added to maintain the total volume of 560 mL, and then it was kept static to deposit lignin. The content of lignin was determined by

$$\text{The content of lignin (\%)} = \frac{m_2}{m_0} \times 100 \quad (4)$$

where m_0 (g) is the oven-dry weight of the bamboo powder and m_2 (g) is the oven-dry weight of the collected lignin.

The aforementioned procedure was repeated; the arithmetic average value of the two measurements was taken as the result. The error between two measurements should not exceed 0.2%.

2.3.5. Hot Water Extractives. The content of hot water extractives (extractives for short) was determined by GB/T 2677.4-1993. About 2 g (±0.1 mg) of bamboo powders was added into

Table 1: Chemical component contents of bamboo during heat treatment.

Labels	Holocelluloses (%)	α-cellulose (%)	Hemicellulose (%)	Lignin (%)	Extractives (%)
Untreated	68.21(0.65)	38.25(2.38)	29.96(1.23)	22.06(0.88)	6.34(2.41)
180°C treated	60.72(0.06)	36.73(0.07)	23.99(0.56)	25.67(3.12)	7.95(1.32)
200°C treated	55.86(2.47)	35.14(1.70)	20.72(3.43)	31.67(3.08)	8.82(0.35)

Note. values in the brackets are deviations.

200 mL distilled water with temperature of 95-100°C. After placing in 100°C water bath for 3 h, the mixture was put into a reflux condensation tube. Prior to washing with distilled water, the solution was filtered with a tared sintered glass crucible. Then the residues were dried at in an oven to reach constant weight. The content of extractives was calculated by the following:

$$\text{The content of hot water extractives (\%)} = \frac{m_0 - m_3}{m_0} \times 100 \quad (5)$$

where m_0 (g) is the oven-dry weight of the bamboo power and m_3 (g) is the oven-dry weight of the sample after hot water extracting.

The aforementioned procedure was repeated; the arithmetic average value of the two measurements was taken as the result. The error between two measurements should not exceed 0.2%.

2.4. Static Adsorption at Constant RH. The heat-treated bamboo powder and untreated bamboo powder obtained from 2.3 were placed into boxes and then the boxes were transferred into 3 kinds of desiccators containing the saturated salt solutions (NaCl, K_2CO_3 and LiCl) at a conditioned room with constant temperature of 25°C. The RH of the three salt solutions is 75%, 45%, and 11%, respectively. Every 24 hours, the samples were taken out of the desiccators and weighed until their weight reaches a constant weight. The number of repeated specimens under each condition is 6. The moisture content at constant RH was the average value of 6 specimens.

2.5. Hailwood-Horrobin Sorption Theory. The sorption behavior of heat-treated bamboo and untreated bamboo was explored using the H-H sorption theory [20]. In the theory, the sorption isotherm of wood can be described as a parabola by

$$\frac{h}{m} = A + Bh - Ch^2 \quad (6)$$

$$A = \frac{W}{18}\frac{1}{K_2(K_1+1)},$$
$$B = \frac{W}{18}\frac{K_1-1}{K_1+1}, \quad (7)$$
$$C = \frac{W}{18}\frac{K_1K_2}{K_1+1}$$

where h is the relative humidity, m is the moisture content of bamboo, K_1 is the equilibrium constant, where the hydrated bamboo is formed from the dissolved water and dry bamboo, K_2 is the equilibrium constant between dissolved water and water vapor, W is the molar mass of wood, and $18/W$ is the moisture content corresponding to complete hydration of all the available sorption sites.

Hydrated water (m_h) and dissolved water (m_s) can be further figured out through

$$m_h = \frac{(18/W)K_1K_2h}{(1+K_1K_2h)} \quad (8)$$

$$m_s = \frac{(18/W)K_2h}{(1-K_2h)} \quad (9)$$

2.6. Dynamic Sorption at Sinusoidal RH. The heat-treated samples and untreated samples were conditioned at 20°C in 45%RH and submitted to a cyclic RH oscillation, where the RH was changed sinusoidally between 75% and 45%RH at a constant temperature of 20°C. Prior to dynamic sorption, all the samples were placed over saturated salt solutions of K_2CO_3 (the corresponding RH was 45%) over 10 days for preconditioning. The dynamic sorption testing was carried out in a conditioning oven (DHS 225, YaShiLin Co., Ltd., Beijing) [21]. The RH changed for 4 cycles and each cyclic period lasted 6 h. In line with the predetermined schedule, the RH in the conditioning oven was programmed to change at discrete steps. The RH (sensitivity±1%) was monitored by a thermorecorder (TR-72Ui, T and d Co., Ltd, Japan) which was placed closed to the specimens. During the experimental process, the weight changes were measured at every 5 min intervals by an electronic analytical balance (ME104E, Mettler-toledo Co., Ltd., Columbus, OH, USA) (sensitivity±0.1 mg). During the whole dynamic testing process, the measurement data can be automatically recorded by the personal computer without opening the door of the oven.

3. Results and Discussion

3.1. Chemical Composition. The results of the chemical composition analysis indicated that the content of holocellulose and hemicellulose declined after heat treatment and kept on decreasing as rising the temperature (Table 1). The relative content of α-cellulose decreased slightly while that of lignin and extractives increased, which was consistent with the results reported by Lee et al. [15].

3.2. Static Adsorption at Constant RH. Figure 1 shows the equilibrium moisture contents (EMC) of the samples at various humidities. The EMCs of heat-treated samples were lower than those of untreated samples under any humidity

Table 2: Values for parameters in Hailwood-Horrobin sorption theory and moisture sorption coefficient Z.

Parameters	Untreated	180°C treated	200°C treated
K_1	10.29	6.74	6.5
K_2	0.88	0.91	0.92
$18/W$ (%)	4.27	3.19	3.11
Z	0.19	0.17	0.15

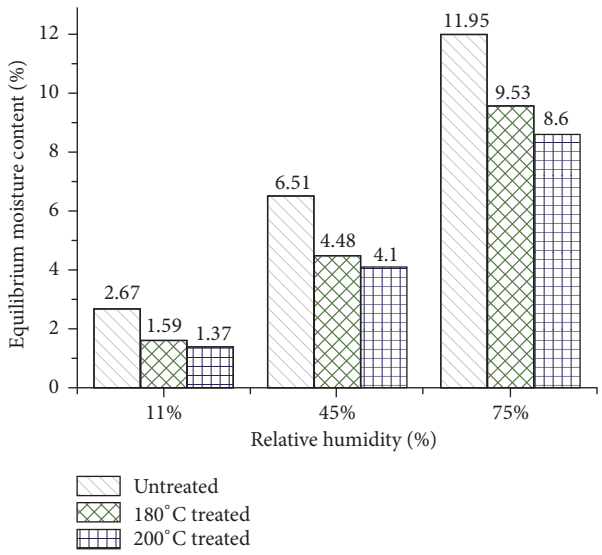

Figure 1: Equilibrium moisture contents (EMC) of the samples at various humidities.

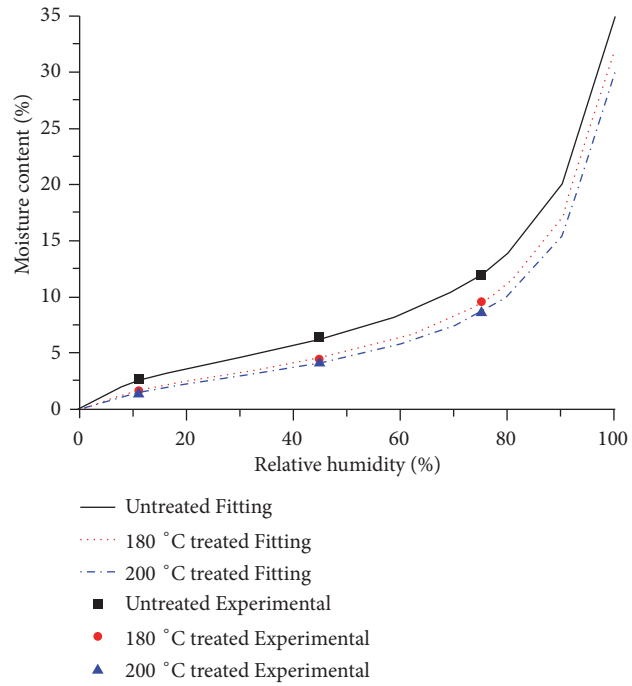

Figure 2: Sorption isotherms calculated by H-H sorption theory and a comparison with experimental data.

condition, and the higher the temperature of heat treatment temperature, the lower the EMC of bamboo. This was because the chemical changes during heat treatment resulted in the decrease of the amount of sites which are able to absorb bound water [12]. Using this data, the main parameters given in (6) and (7) can be calculated and the corresponding values are summarized in Table 2.

As seen from Table 2, K_2 values of all the samples were approximately 0.9, similar to the values for solid wood [22]. All the values of $18/W$ of bamboo flours fell in the range of 3% to 4%. In other words, the MC of samples should be between 3% and 4% when all the hydroxyls available are saturated by a monolayer of adsorbed water. A comparison of $18/W$ values between samples indicated that the $18/W$ values for heat-treated samples were lower than the untreated samples, demonstrating a reduction of free hydroxyl groups after heat treatment due to the partial removal of hemicellulose. The hemicellulose loss of the heat-treated sample at 200°C was higher than that at 180°C (Table 1), and accordingly the former showed a minimum $18/W$ value.

The sorption isotherms calculated using EMC of bamboo samples according to H-H sorption theory are shown in Figure 2. The fitting curve agrees well with the experimental data, confirming the effectiveness of the data in Table. Moreover, the final water absorption readings of the samples were in the following order: untreated sample>heat-treated sample at 180°C > heat-treated sample at 200°C.

Figure 3 shows the MC of samples for hydrated water and dissolved water. Both of the contents of hydrated water and dissolved water were characterized by a trend in which the untreated sample showed the highest MC, followed by the heat-treated sample at 180°C and the heat-treated sample at 200°C. Furthermore, after heat treatment, the contents of hydrated water of bamboo had been substantially reduced (Figure 3(a)).

The moisture adsorption coefficient Z is the variation of wood MC per unit of RH, which is usually used as an index to evaluate wood hygroscopicity. The coefficients for the samples within the RH range of 45% to 75% ($z = (MC_{75\%RH} - MC_{45\%RH})/30\%$) are listed in Table 2. It can be found that Z of the untreated sample was 0.19, close to the values for 28 wood species (0.20) [23]. The lower Z values for the heat-treated samples demonstrated a drop in hygroscopicity.

3.3. Dynamic Sorption at Sinusoidal RH. Figure 4 shows the general MC responses of heat-treated samples and untreated samples to the sinusoidal RH for 4 cycles. It can be clearly seen that the MCs of all the samples change sinusoidally with the sinusoidal variation of RH, but they lag behind the change of RH in phase.

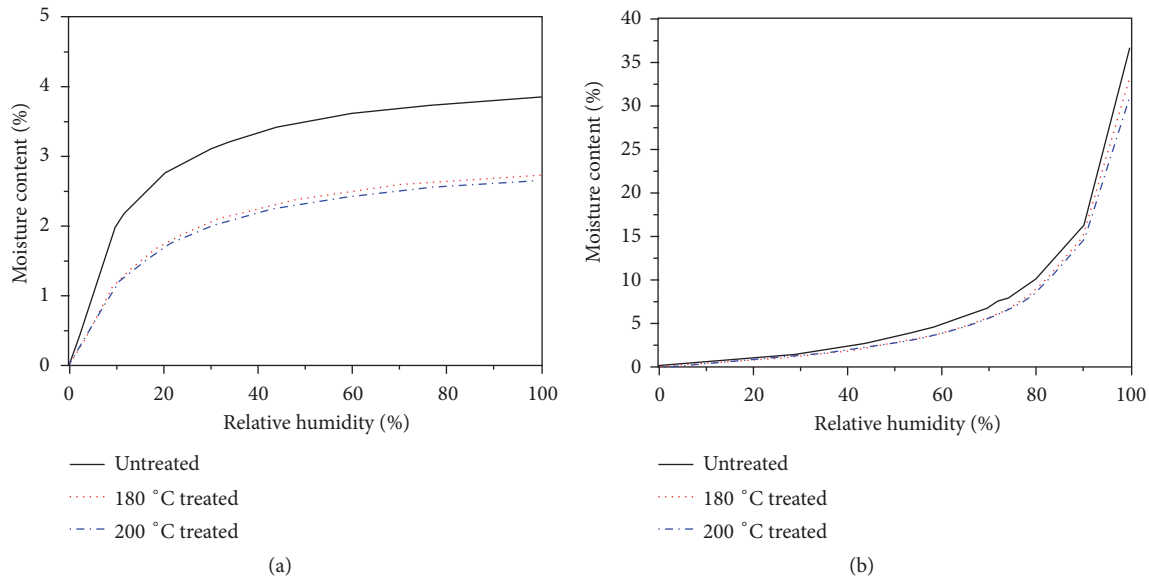

Figure 3: Moisture content of samples for (a) hydrated water and (b) dissolved water.

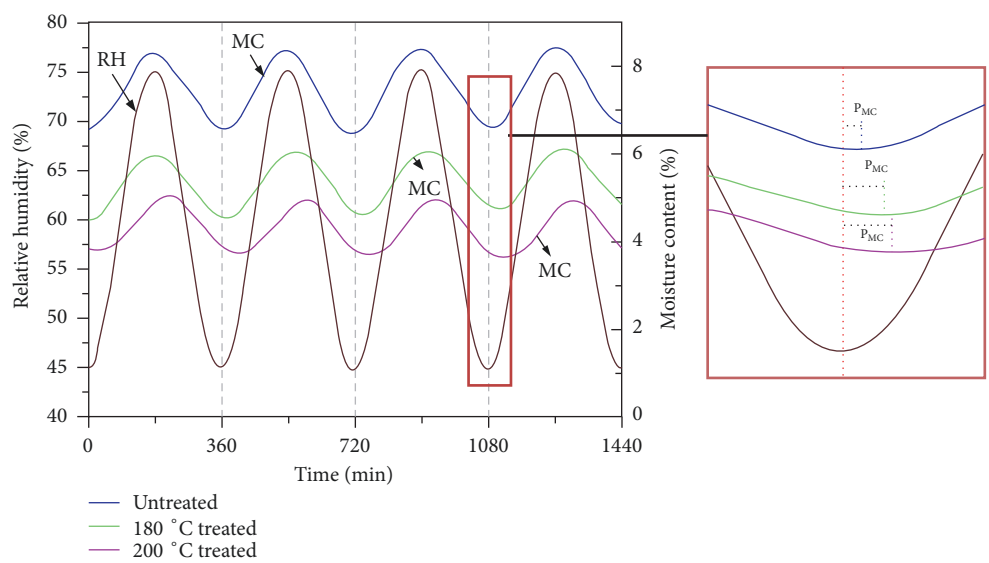

Figure 4: Plots of moisture content changes where relative humidity changes sinusoidally at a constant temperature against cyclic time for untreated and heat-treated bamboo samples. P_{MC}: phase lag of MC change.

As seen from Figure 4, the starting points of MC of the three types of samples were different, which was consistent with the static moisture adsorption. This was because they have reached their respective EMC at 45%RH after a long period moisture adjustment before the dynamic moisture sorption began. Table 3 lists the amplitude of MC response of all the samples under dynamic conditions and MC increment from RH 45% to 75%. The untreated samples showed the greatest amplitude while the heat-treated samples at 200°C showed the smallest. This was because the decrease of hemicellulose reduced the moisture absorption sites. Compared with the results of static moisture absorption, when the RH was changed from 45% to 75%, the increment of MC for all the samples under dynamic condition was smaller than that under static condition (Table 3). As the RH was changed sinusoidally, bamboo no longer had enough time to reach the EMC at the specified humidity.

The phase lag of MC reflected the speed of response to RH change. The larger the phase lag was, the lower the response to the RH change was. As seen from Figure 4, the heat-treated bamboo showed a larger phase lag than untreated bamboo, demonstrating the lower mass transfer rate of moisture after heat treatment.

Figure 5 presents the MC data for heat-treated samples at 200°C between the 3rd wave trough point and the 4th wave trough point in Figure 4 with sinusoidal RH. An

Table 3: Amplitude of MC response and hysteresis ratio of all the samples under dynamic conditions and MC increment from RH 45% to 75%.

Sample	Dynamic sorption		Static adsorption (45%-75%)
	Amplitude of MC (%)[a]	Ads. MC/Des. MC[a]	Increment of MC (%)
Untreated	1.86	0.828	5.44
180°C treated	1.48	0.845	5.05
200°C treated	1.31	0.854	4.50

[a]Average value with relative humidity (RH) changed sinusoidally between 45% and 75%.

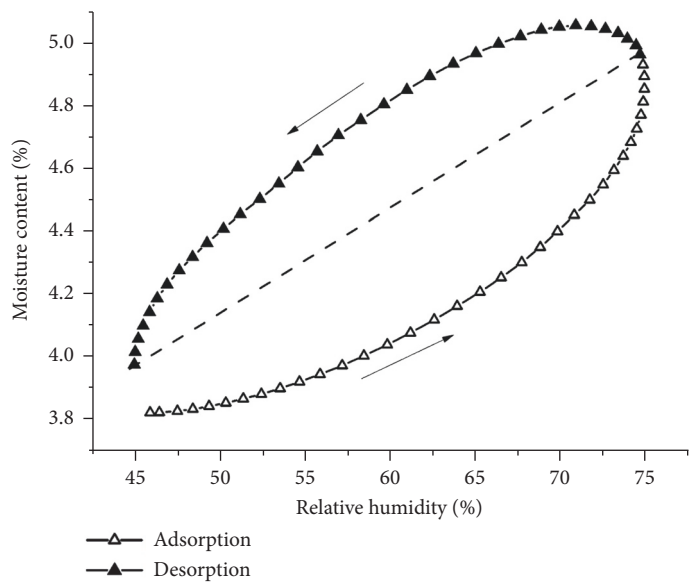

Figure 5: Plots of dynamic moisture content changes against sinusoidal relative humidity for 200°C treated bamboo.

obvious sorption hysteresis could be observed. The minimum hysteresis ratio "Ads. MC/Des. MC" for all the samples was calculated (Table 3). After heat treatment, the hysteresis ratio decreased and it was inversely related to the temperature of heat treatment, which could be explained by the relaxation theory. The sorption hysteresis is primarily influenced by the softening of hemicellulose. Therefore, a decrement in sorption hysteresis would follow after the partial removal of hemicellulose.

4. Conclusion

In this study, the influence of heat treatment on the adsorption behavior of bamboo at constant relative humidity and its dynamic sorption behavior at sinusoidal relative humidity has been investigated. The hemicellulose of bamboo was greatly removed after the heat treatment. Under the constant condition, the untreated bamboo exhibited the highest moisture content and moisture sorption coefficient, followed by the 180°C heat-treated sample and 200°C heat-treated sample. Under the dynamic condition, the moisture content of all the sample changed sinusoidally but lagged behind the triggering sinusoidal relative humidity changes. The heat-treated samples showed a decrement in the amplitudes of moisture content and an increment in the phase lag. The removal of hemicellulose after heat treatment also led to the reduction in sorption hysteresis of bamboo.

Data Availability

The data used to support the findings of this study are available from the corresponding author upon request.

Conflicts of Interest

The authors declare that they have no conflicts of interest.

Acknowledgments

This work was financially supported by the National Natural Science Foundation of China (Nos. 31870550, 31470591).

References

[1] T. Li, D.-L. Cheng, M. E. P. Wålinder, and D.-G. Zhou, "Wettability of oil heat-treated bamboo and bonding strength of laminated bamboo board," *Industrial Crops and Products*, vol. 69, pp. 15–20, 2015.

[2] A. Azadeh and K. Ghavami, "The influence of heat on shrinkage and water absorption of Dendrocalamus giganteus bamboo

as a functionally graded material," *Construction and Building Materials*, vol. 186, pp. 145–154, 2018.

[3] R. D. Manalo and M. N. Acda, "Effects of hot oil treatment on physical and mechanical properties of three species of Philippine Bamboo," *Journal of Tropical Forest Science*, vol. 21, no. 1, pp. 19–24, 2009.

[4] J. Q. Qi, J. L. Xie, X. Y. Huang, W. J. Yu, and S. M. Chen, "Influence of characteristic inhomogeneity of bamboo culm on mechanical properties of bamboo plywood: effect of culm height," *Journal of Wood Science*, vol. 60, no. 6, pp. 396–402, 2014.

[5] B. Sharma, A. Gatóo, and M. H. Ramage, "Effect of processing methods on the mechanical properties of engineered bamboo," *Construction and Building Materials*, vol. 83, pp. 95–101, 2015.

[6] C.-H. Lee, M.-J. Chung, C.-H. Lin, and T.-H. Yang, "Effects of layered structure on the physical and mechanical properties of laminated moso bamboo (Phyllosachys edulis) flooring," *Construction and Building Materials*, vol. 28, no. 1, pp. 31–35, 2012.

[7] A. C. D. Almeida, V. A. D. Araujo, E. A. M. Morales, M. Gava, R. A. Munis, and J. N. Garcia, "Wood-bamboo particleboard: mechanical properties," *Bioresources*, vol. 12, pp. 7784–7792, 2017.

[8] T. C. Yang, T. L. Wu, K. C. Hung, Y. L. Chen, and J. H. Wu, "Mechanical properties and extended creep behavior of bamboo fiber reinforced recycled poly(lactic acid) composites using the time-temperature superposition principle," *Construction & Building Materials*, vol. 93, pp. 558–563, 2015.

[9] Y. M. Zhang, Y. L. Yu, and W. J. Yu, "Effect of thermal treatment on the physical and mechanical properties of phyllostachys pubescen bamboo," *European Journal of Wood and Wood Products*, vol. 71, no. 1, pp. 61–67, 2013.

[10] B. M. Esteves and H. M. Pereira, "Wood modification by heat treatment: A review," *Bioresources*, vol. 4, no. 1, pp. 370–404, 2009.

[11] J. H. Kwon, R.-H. Shin, N. Ayrilmis, and T. H. Han, "Properties of solid wood and laminated wood lumber manufactured by cold pressing and heat treatment," *Materials and Corrosion*, vol. 62, pp. 375–381, 2014.

[12] M. Bak and R. Németh, "Changes in swelling properties and moisture uptake rate of oil-heat-treated poplar (Populus × euramericana cv. pannónia) wood," *Bioresources*, vol. 7, no. 4, pp. 5128–5137, 2012.

[13] D. S. Korkut and B. Guller, "The effects of heat treatment on physical properties and surface roughness of red-bud maple (Acer trautvetteri Medw.) wood," *Bioresource Technology*, vol. 99, no. 8, pp. 2846–2851, 2008.

[14] G. Gündüz, S. Korkut, and D. S. Korkut, "The effect of heat treatment on physical and technological properties and surface roughness of Camiyani Black Pine (Pinus nigra Arn. Subsp. Pallasiana var. pallasiana) wood," *Bioresource Technology*, vol. 99, no. 7, pp. 2275–2280, 2008.

[15] C.-H. Lee, T.-H. Yang, Y.-W. Cheng, and C.-J. Lee, "Effects of thermal modification on the surface and chemical properties of moso bamboo," *Construction and Building Materials*, vol. 178, pp. 59–71, 2018.

[16] T.-H. Yang, C.-H. Lee, C.-J. Lee, and Y.-W. Cheng, "Effects of different thermal modification media on physical and mechanical properties of moso bamboo," *Construction and Building Materials*, vol. 119, pp. 251–259, 2016.

[17] R. Wahab, A. Mohamad, H. W. Samsi, and O. Sulaiman, "Effect of heat treatment using palm oil on properties and durability of Semantan bamboo," *Journal of Bamboo and Rattan*, vol. 4, no. 3, pp. 211–220, 2005.

[18] A. P. Schniewind, "Creep-rupture life of Douglas-fir under cyclic environmental conditions," *Wood and Science Technology*, vol. 1, no. 4, pp. 278–288, 1967.

[19] R. J. Zhao, Z. H. Jiang, C. Y. Hse, and T. F. Shupe, "Effects of steam treatment on bending properties and chemical composition of moso bamboo (Phyllostachys pubescens)," *Journal of Tropical Forest Science*, vol. 22, no. 2, pp. 197–201, 2010.

[20] A. J. Hailwood and S. Horrobin, "Absorption of water by polymers: Analysis in terms of a simple model," *Transactions of the Faraday Society*, vol. 42, pp. B084–B092, 1946.

[21] T. Yang, E. Ma, and J. Zhang, "Dynamic moisture sorption and hygroexpansion of Populus euramericana Cv. under two cyclic hygrothermal conditions," *Holzforschung*, vol. 70, no. 12, pp. 1191–1199, 2016.

[22] H. Zhou, R. Xu, and E. Ma, "Effects of removal of chemical components on moisutre adsorption by wood," *Bioresources*, vol. 11, no. 2, pp. 3110–3122, 2016.

[23] D. Noack, E. Schwab, and A. Bartz, "Characteristics for a judgment of the sorption and swelling behavior of wood," *Wood and Science Technology*, vol. 7, no. 3, pp. 218–236, 1973.

Hindawi
Advances in Polymer Technology
Volume 2019, Article ID 5973403, 17 pages
https://doi.org/10.1155/2019/5973403

Research Article

Study on External Gas-Assisted Mold Temperature Control for Improving the Melt Flow Length of Thin Rib Products in the Injection Molding Process

Phan The Nhan,[1] Thanh Trung Do,[1] Tran Anh Son,[2] and Pham Son Minh[1]

[1] *HCMC University of Technology and Education, Hochiminh City, Vietnam*
[2] *Ho Chi Minh City University of Technology, Vietnam*

Correspondence should be addressed to Pham Son Minh; minhps@hcmute.edu.vn

Received 20 December 2018; Revised 1 February 2019; Accepted 28 March 2019; Published 17 April 2019

Guest Editor: Jianzhang Li

In the injection molding process, mold temperature control is one of the most efficient methods for improving product quality. In this research, an external gas-assisted mold temperature control (Ex-GMTC) with gas temperature variation from 200°C to 400°C was applied to thin wall injection molding at melt thicknesses from 0.2 to 0.6 mm. The melt flow length was evaluated through the application of this system to the mold of a thin rib product. The results show that the heating process achieves high efficiency in the initial 20 s, with a maximum heating rate of 6.4°C/s. In this case, the mold surface reached 158.4°C. By applying Ex-GMTC to a 0.2 mm flow thickness, the flow length increased from 37.85 to 41.32 mm with polypropylene (PP) material and from 14.54 to 15.8 mm with acrylonitrile butadiene styrene (ABS) material. With the thin rib mold and use of Ex-GMTC, the mold temperature varied from 112.0°C to 140.8°C and the thin rib height reached 7.0 mm.

1. Introduction

Injection molding is a popular method for manufacturing plastic products. However, with consumer demands for higher product quality, as well as increasingly complex product geometries, it is clear that the injection molding process requires improvement. In this regard, mold temperature control is an effective method for solving issues encountered during the melt filling step [1–3]. In general, with a high mold surface temperature, component quality is improved; however, the cooling time and cycle time will both increase. By contrast, decreasing the mold surface temperature will reduce the cooling time but limit the surface quality of the component [4, 5]. Therefore, a critical requirement for current studies is to increase the mold surface temperature while maintaining a sufficiently short cycle time.

For the molding of micro products or products with thin walls, mold temperature should be set as high as the equipment allows. In the common molding process using a mold temperature controller, the mold temperature can be raised to about 90°C by hot water flowing inside the cooling channel [6]. However, in the field of electronic production using materials such as polycarbonate (PC) or polymethyl methacrylate (PMMA), the mold temperature must be higher than 100°C. In such cases, many different methods have been investigated for the purpose of raising mold temperature.

One common solution for cases where mold temperature must be higher than 100°C is the application of steam heating to the mold plate [7]. Although such a method is efficient in terms of the molding process and improving component quality, it may damage the channel and connector when operating at high pressure; energy use is also an issue. Use of an electronic heater inserted into the mold plate has also been suggested. The heater heats the mold cavity to the target temperature before the mold plate is cooled by the cooling channel. This method can heat the mold to higher than 100°C, but the heating time is an issue [8]. To improve the heating rate during mold temperature control, a thin heater has been adopted to control the temperature of cavity surfaces during the injection molding process. This method can support fast cooling even if it is kept active for very long periods. In experiments where the heater was set at 150°C

for a long heating period, the results showed a significant effect on sample frozen-in orientation, as identified by optical microscopy and confirmed by X-ray analysis. This method could be applied to micro injection molding with a suitable sheet heater [9]. However, in general, the electrical method often requires additional design and tool costs; this method also requires an auxiliary heating source.

To reduce energy wastage, surface heating methods have been studied. Chang et al. studied mold heating by infrared systems using simulations and experiments [10]. Their results showed that energy wastage was reduced. For a high heating rate, induction heating was investigated by Chen et al. [11], with the results illustrating that a large heating rate was achieved when using a suitable coil design. In addition, certain types of induction heating have been suggested such as proximity heating [12, 13] and ring coil heating [14]. However, with induction heating methods, there remain application difficulties, such as identifying the required coil design for reaching a good temperature distribution and the potential for overheating, which will damage the mold material. For directly heating the mold surface, gas-assisted mold temperature control (GMTC) has been suggested. With this approach, hot gas flows into the mold cavity. Through heat convection, the mold surface receives energy, increasing its temperature. In this method, the heating system includes gates inserted into the mold plate for hot gas entrance and exit [15, 16]. Initial results showed that the cavity surface could be heated to over 200°C. In addition, because hot gas flows into the cavity, this method can heat a complex cavity. However, the mold structure becomes more complex because of the combining of heating systems. Another disadvantage of GMTC is the temperature distribution; this is an issue that needs to be resolved.

Therefore, based on the disadvantages reported for GMTC, we applied external GMTC (Ex-GMTC) in which the gas temperature was varied from 200°C to 400°C. This was applied to thin wall injection molding at melt thicknesses of 0.2 to 0.6 mm. To improve the temperature distribution, the heating step was achieved using four gas gates on a melt flow length mold. In this case, the four gas gates were arranged along the cavity surface. After the molding process was complete, the length of the molding product was measured to observe the influence of Ex-GMTC on melt flow length. In addition, Ex-GMTC was applied to the injection mold of a thin rib product. In this application, the improvement of rib height was observed by heating the mold surface until the surface temperature was higher than the glass temperature of the material. In all cases, simulations were used to predict the heating rate and temperature distribution. Experimentally, mold temperatures were determined by infrared camera. The experiment and simulation results are compared and discussed.

2. Simulation and Experimental Methods

In general, the application of gas-assisted mold surface heating in injection molding is achieved using the six steps shown in Figure 1 [17]. According to this process, the mold cavity is heated to the target temperature before the hot melt is filled into the mold cavity. The greatest difference compared with the common injection molding process is the heating in Step 2. As with our former research on mold temperature control, hot gas was used as a heating source to increase the cavity surface temperature of the injection mold. Compared with other studies on gas heating for injection mold temperature control [15–17], Ex-GMTC is a new technique in the field of mold temperature control and can heat the cavity surface rapidly during the injection molding process without a significant change in the mold structure. During the heating operation, two mold plates are first moved to the open position by opening the mold. Second, a hot gas drier is moved to the heating position by a robot arm; then, the hot gas is sprued to directly contact the cavity surface. This hot gas heats the cavity surface to the target temperature. Third, after the cavity surface is heated to the target temperature, the gas drier is moved outside the molding area and the mold completely closes in preparation for the melt filling process.

In this research, the Ex-GMTC system consisted of a mold temperature controller, a hot gas generator system (including an air compressor, air drier with a power of 12 kW, and digital volumetric flow controller), and a robot arm for moving the hot gas generator system to the heating position. The assembly of the Ex-GMTC system and the injection molding machine is shown in Figure 2. For generating the hot air, the air drier was used with dimensions of 240 mm x 100 mm x 60 mm as shown in Figure 3. A gas channel, 5 mm in width and 10 mm in depth, was cut inside the gas drier. The environment air will press into the air drier with the pressure of 7 Bar; then, the air will flow along the gas channel and absorb the thermal energy from the wall of air channel. The hot air will flow out at the four gates with the hole diameter of 10 mm. The function of the high power hot gas generator system is to support a heat source, which provides a flow of hot air up to 400°C with an inlet gas pressure up to 7 Bar.

In this study, to observe the improvement of the melt flow length when using the Ex-GMTC, an injection mold was designed and manufactured with the structure of a cavity plate, as shown in Figure 4. In this case, the mold was designed with two cavities. One had the common structure and the other was designed with an insert, as shown in Figure 5. As with our previous research [15–17], this type of design helped to increase the heating efficiency and better control the heating area. The mold and the Ex-GMTC were assembled with a SW-120B molding machine from Shine Well Machinery Co., Ltd, as shown in Figure 6.

To study the temperature distribution of the heating area, a simulation model was built to represent the experiments. Because a cavity insert (Figure 5) was used, an insulation component covered the heating area; therefore, the simulation model includes only two volumes: the heating area volume and the hot gas volume, as shown in Figure 7. In contrast with former papers on gas-assisted temperature control for injection molding processes [15–17], the hot gas was sprued to the heating area via four gates to increase the temperature uniformity of the cavity surface. The simulation model and meshing model are shown in Figure 7, and the boundary conditions are shown in Table 1. To improve the

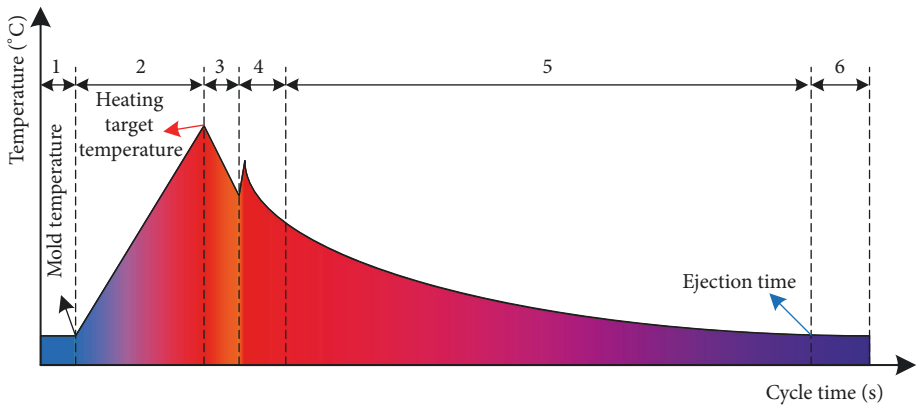

1. Mold closes to heating position
2. Hot gas heats the mold surface
3. Mold closes to molding position
4. Filling and packing process
5. Cooling process
6. Mold opens for part ejection

Figure 1: General process of gas-assisted mold surface heating in injection molding [17].

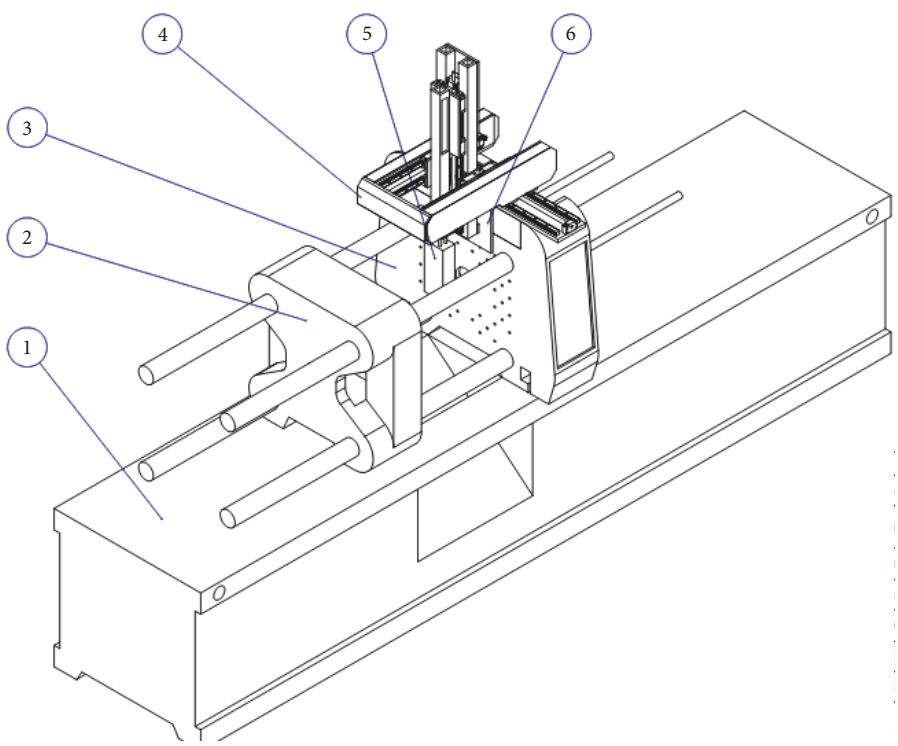

(1) Injection molding machine
(2) Core side
(3) Cavity side
(4) Robot arm
(5) Hot-gas generator
(6) The position for hang on the robot arm

Figure 2: External gas-assisted mold temperature control heating devices.

Table 1: Simulation parameters for studying melt flow length.

Simulation parameters						
Air inlet temperature of air drier	30°C, 7 bar					
Air outlet temperature of air drier (°C)	30	200	250	300	350	400
Air density (kg/m^3) [18]	1.165	0.746	0.680	0.616	0.570	0.524
Heat capacity of air (J/kg∗K) [18]	1004	1026	1035	1046	1057	1068
Thermal-expansion coefficient of air (x10^{-3}K^{-1}) [18]	3.32	2.1	1.93	1.76	1.64	1.52
Air pressure	1 atm					
Initial temperature of mold insert	30°C					
Aluminum density - ASTM B209-14	2702 kg/m^3					
Heat capacity of aluminum - ASTM B209-14	903 J/kg∗K					
Thermal conductivity of aluminum - ASTM B209-14	237 W/m∗K					
P20 steel density - ASTM A681	7870 kg/m^3					
Heat capacity of P20 steel - ASTM A681	460 J/kg∗K					
Thermal conductivity of P20 steel - ASTM A681	29 W/m∗K					
Simulation type	Transient					
Heating time	0 s ⟶ 30 s					
Air outlet to environment	(i) Environment pressure: 1 atm (ii) Air temperature: 30°C					
Initial air volume	(i) Air velocity: 0 m/s (ii) Air pressure: 1 atm (iii) Air temperature: 30°C					

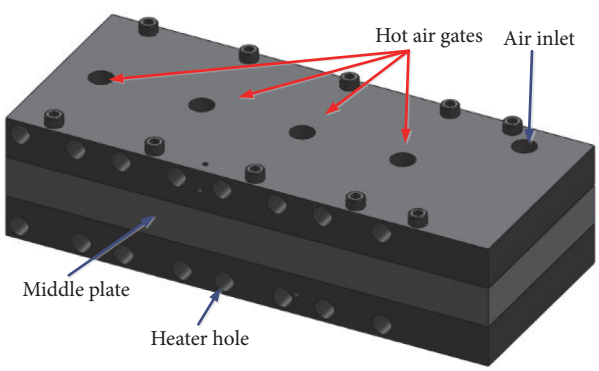

Figure 3: Air drier component parts.

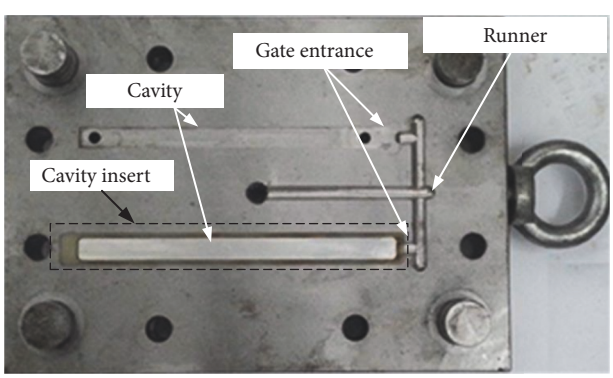

Figure 4: Cavity plate of melt flow length mold.

simulation accuracy, the cavity insert was meshed with a hex dominant element with seven layers in the thickness direction. In addition, with the air volume, a tetrahedron element used with a smaller element size was set up at the hot gas inlet location. The heating process was simulated by ANSYS software with the same experimental parameters.

After studying the influence of Ex-GMTC on the melt flow length of the injection molding process, this heating method was applied to a real product with a thin rib, as shown in Figure 8. The thin rib had a thickness varying from 0.5 to 0.3 mm and a height of 7.0 mm. This rib size is often used in plastic products for the electrical field. In many cases, a thin rib is used to increase the rigidness of the product; however, in the molding process, fully filling this type of rib is a challenge of rapid cooling of the melt as it enters the cavity. To improve the process of filling melt into a thin rib, Ex-GMTC was applied using one gate of hot gas. The heating area and the cavity structure are shown in Figure 9. The hot gas was sprued directly on the center of the heating area. Then, the temperature distribution and temperature values at three points, as shown in Figure 9, were collected. For observing the temperature distribution along the thickness of mold, a 3D thermal fluid analysis was performed by ANSYS software. Figure 10 shows the simulation model of the thin rib mold. In simulation, the heat transfer mode around all external surfaces of mold plate was set at free convection to the air, with ambient temperature at 30°C and a heat transfer coefficient of 10 W/m2 K. The same with experiment, the area at the cavity center was designed with a steel insert to improve the heating efficiency. This cavity insert had dimensions of 40 × 25 × 1.0 mm^3. A 400°C gas inlet was used for simulation.

3. Results and Discussion

3.1. Effect of External Gas-Assisted Mold Temperature Control on the Heating Process of a Melt Flow Length Mold. In our former research [15–17], when hot gas was used to raise cavity temperature, heating efficiency was relatively good. However, in addition to the disadvantage of the complex mold structure, the temperature distribution within the cavity is an issue in need of further research. Therefore, in

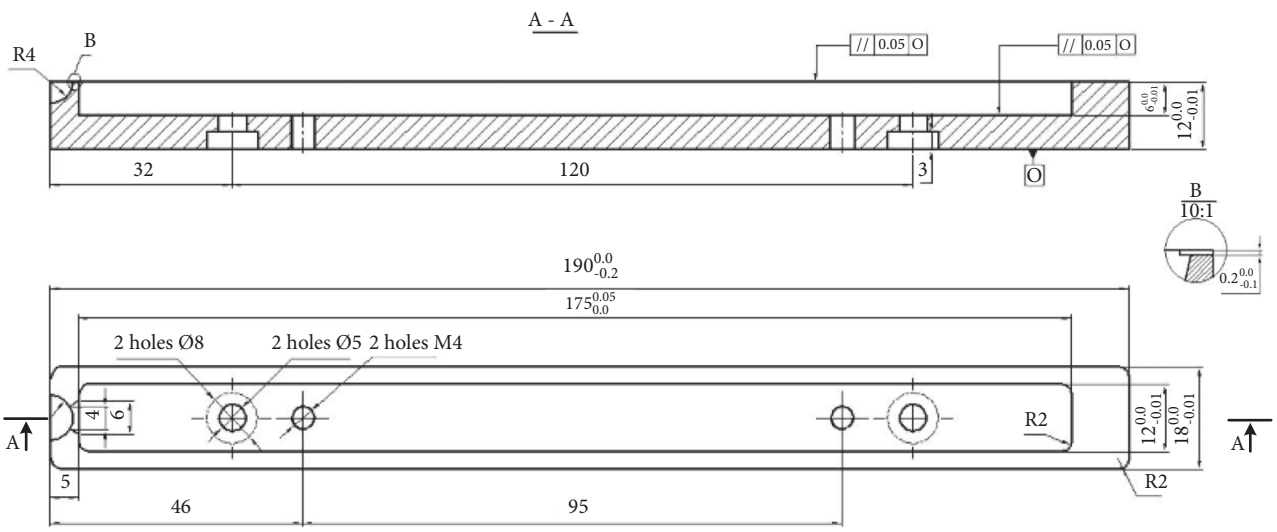

(a)

(b)

Figure 5: Mold insert for studying melt flow length. (a) Design of mold insert. (b) Experimental mold insert.

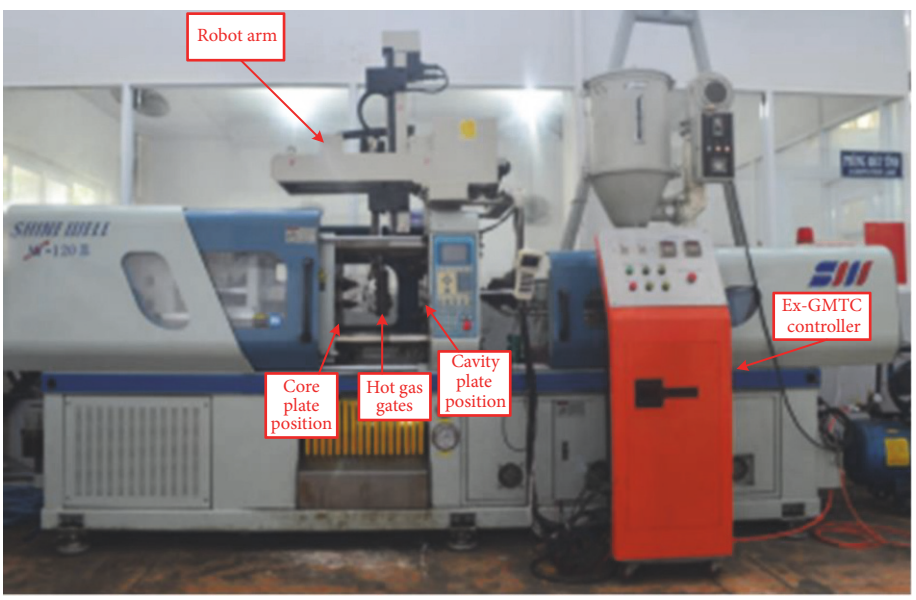

Figure 6: External gas-assisted mold temperature control experiment model.

this research, with Ex-GMTC used for the injection molding process, the heating process was observed in relation to the heating rate and temperature distribution within the cavity. To study the application of Ex-GMTC, the mold was designed as in Figure 4, with the gas drier having four hot gas gates. These gates were arranged along the cavity to improve the temperature distribution and heating rate. As an initial step, heating was simulated using the model, as in Figure 7. The heating process was performed at gas temperatures of 200°C, 250°C, 300°C, 350°C, and 400°C, a heating time of 30 s, and an initial cavity surface temperature of 30°C.

The simulation results show the temperature distribution of the cavity at the top view as in Figure 11 and the cross section A-A as in Figure 12. The temperature at the four

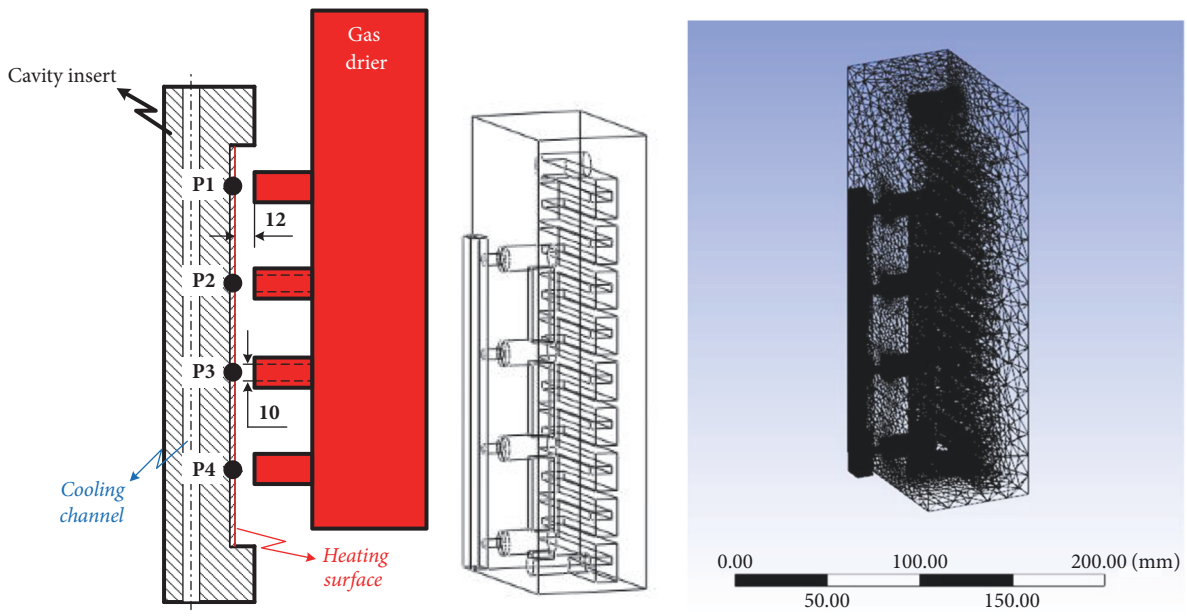

(a) Heating position (b) Simulation model (c) Meshing model

Figure 7: Model of Ex-GMTC with 4 gas gates.

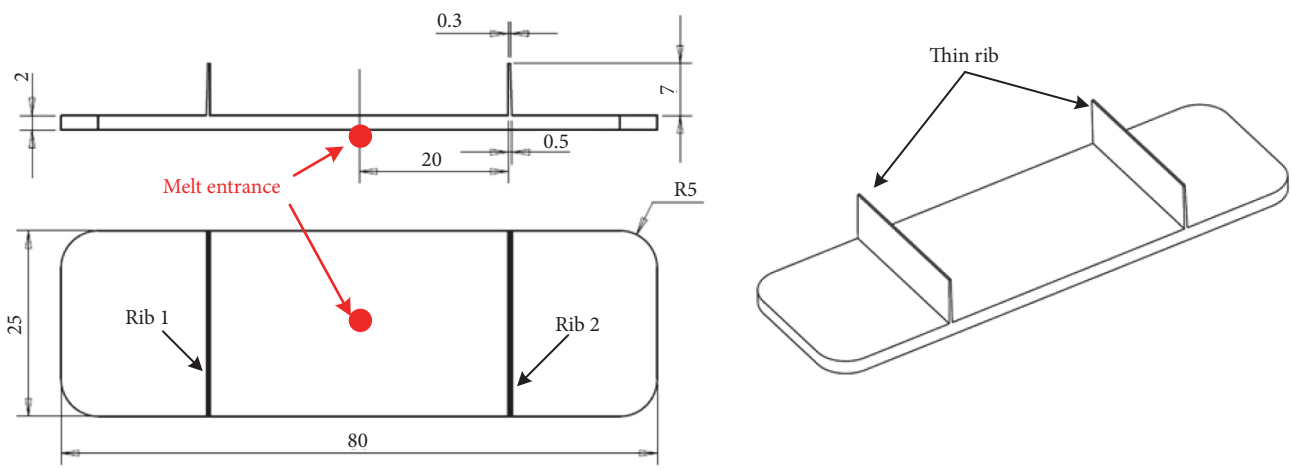

Figure 8: Thin rib model.

measurement points was collected as in Table 2. According to the temperature distribution simulation results, the cavity surface underwent a relatively balanced heating process, although there were some higher temperature regions near the hot gas gates. The differences in temperature are clearer at the beginning of the heating period because the heating rate at the gas gates was very strong during this period. This phenomenon is clear at all gas temperatures. By contrast, when a higher gas temperature was used (Figures 11(e) and 12), the difference in temperature is also clear at the end of heating period. This is because of an imbalance in the thermal energy between the receiving thermal energy (near the gas gates) and the calorific power area (distant from the gas gate). This phenomenon could be observed clearer with the temperature distribution at the cross section A-A as in Figure 12. At higher gas heating temperature, the cavity surface shows a trend of releasing greater calorific power to the environment. Therefore, in the area distant from the gas gate, the temperature was much lower than that of the area near the gas gate. This result could be observed clearly at a 400°C gas temperature and heating time of 30 s. To reduce this imbalance, the gas drier could be designed with more gas gates. However, as compared with other heating methods for injection molds [3, 8–10], the temperature distribution result shows that this heating method, with four gas gates and a cavity length of 175 mm, is highly advantageous. In addition, the effect of cavity insert was clarified by the appearing of higher temperature area at the cavity surface.

To assess heating rate, the temperatures at four points were collected and compared, as shown in Figure 13. According to the results, the raising of temperature showed a limitation of the heating process. The heating efficiency

Table 2: Simulation results of mold cavity temperature after heating for the melt flow length mold.

Heating Time (s)	Position	Gas temperature (°C)				
		200	250	300	350	400
5	P1	62.3	73.2	83.3	92.5	102.8
	P2	58.1	69.3	81.4	84.5	95.4
	P3	56.6	67.2	79.8	82.4	91.3
	P4	57.8	66.0	78.9	76.6	88.4
10	P1	76.0	91.6	109.1	115.8	125.6
	P2	78.3	92.6	109.5	115.5	126.8
	P3	74.5	84.4	105.6	104.3	115.7
	P4	74.4	86.8	104.4	105.1	115.6
15	P1	90.8	105.7	119.0	131.8	148.4
	P2	87.2	102.7	117.5	123.7	144.2
	P3	86.6	101.5	116.3	124.2	142.1
	P4	85.5	101.3	115.4	131.0	141.6
20	P1	92.2	114.0	125.6	147.8	154.8
	P2	90.2	110.9	122.9	146.6	153.7
	P3	88.3	108.1	119.7	145.9	151.1
	P4	84.8	105.3	117.1	145.9	150.5
25	P1	95.6	116.2	129.8	147.4	160.1
	P2	92.1	112.4	125.5	144.0	158.6
	P3	91.2	112.6	123.3	142.1	157.8
	P4	86.6	96.8	117.4	143.8	155.7
30	P1	96.5	119.6	132.9	151.7	161.3
	P2	94.4	117.7	128.0	147.9	159.4
	P3	94.3	116.9	127.4	145.3	158.1
	P4	84.0	106.2	119.6	140.7	152.5

was high only at the beginning of the heating step; after 20 s, the temperature increase was slowed. This result was because of heat convection between the hot gas and the mold surface. At the same gas temperature, when the cavity temperature increased, the transfer of thermal energy was lower. Therefore, with the four gas temperatures, highly efficient heating was achieved within the first 20 s, with a maximum heating rate of 6.4°C/s with the 400°C gas. In this case, although there is a limitation in the raising of temperature, the mold surface reached 158.4°C, which was sufficiently high for almost all of the melt to flow easily into the cavity. By contrast, this limitation reduced overheating of the mold insert, especially with micro injection molding. This is also an advantage of Ex-GMTC as compared with other heating methods for injection molds [10–14].

To verify the accuracy of the simulation result, the experiment was conducted with the same boundary conditions as used in the simulation. The experiment was conducted 10 times for each case and the average value is presented herein. The temperatures at four points (Figure 7(a)) were collected using a thermal camera and compared with the simulation results, as shown in Figure 13. Based on these comparisons, the temperature difference between the simulations and experiments was lower than 12°C. This difference is because of a measurement delay of the thermal camera, especially as the thermal energy can transfer quickly from the high temperature area to the lower temperature area. However, in general, this result demonstrates that the simulations and experiments showed good agreement. In addition, the limitation in the heating process was observed experimentally.

3.2. Effect of External Gas-Assisted Mold Temperature Control on Melt Flow Length. In injection molding, cavity surface temperature has a strong influence on melt flow length because of a reduction of the freeze layer [1, 5]. This property is a key aspect of the molding process, especially with micro products or thin-walled components. In this study, to increase the cavity temperature, Ex-GMTC was applied to the melt flow length mold, as in Figure 4. To observe the effect of Ex-GMTC on the melt flow length, the heating step was achieved at a gas temperature of 400°C and the heating time was varied from 5 to 20 s. After the heating step, the gas drier was moved outside the molding area and the two-half mold plate was closed for the filling step to commence (Step 3 in Figure 1). In this period, the mold temperature will change, and the mold temperature at the end of this period impacts the melt flow length. In the real molding cycle, it takes about 6 s from the end of the heating period to the start of the filling step. Therefore, after the heating period was finished, the mold temperature was measured for comparison with the melt filling result. For the molding experiment, polypropylene (PP 1100N from Advanced Petrochemical Company) and acrylonitrile butadiene styrene (ABS 750SW from Kumho Petrochemical

Table 3: Molding parameters for the melt flow length experiment.

No.	Molding parameters	Value	
		PP material	ABS material
1	Melt temperature	210°C	230°C
2	Injection pressure	60 kg/cm^2	
3	Cooling time	20 s	
4	Injection speed	50 mm/s	
5	Injection time	0.5 s	
6	Packing time	2.5 s	
7	Heating time	5 s, 10 s, 15 s, 20 s	
8	Initial mold temperature	30°C	
9	Glass transition temperature	100°C	105°C

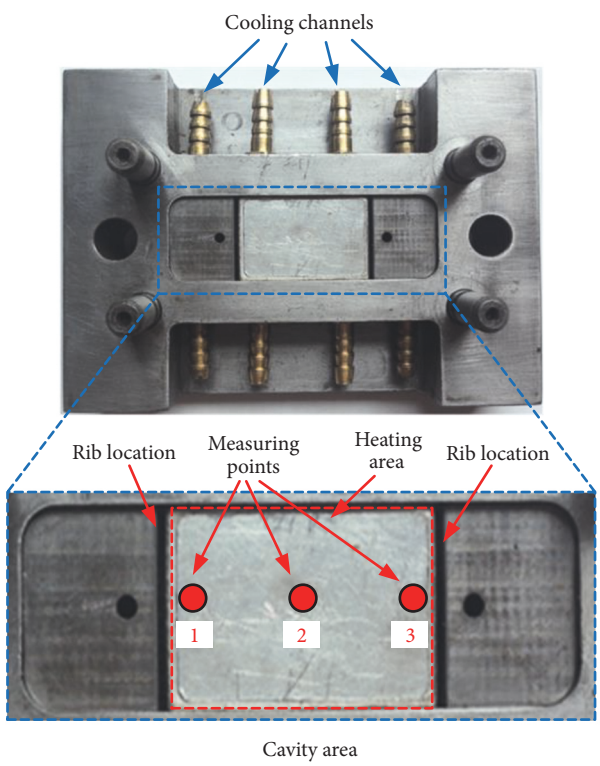

Figure 9: Mold plate of thin rib with the cavity insert.

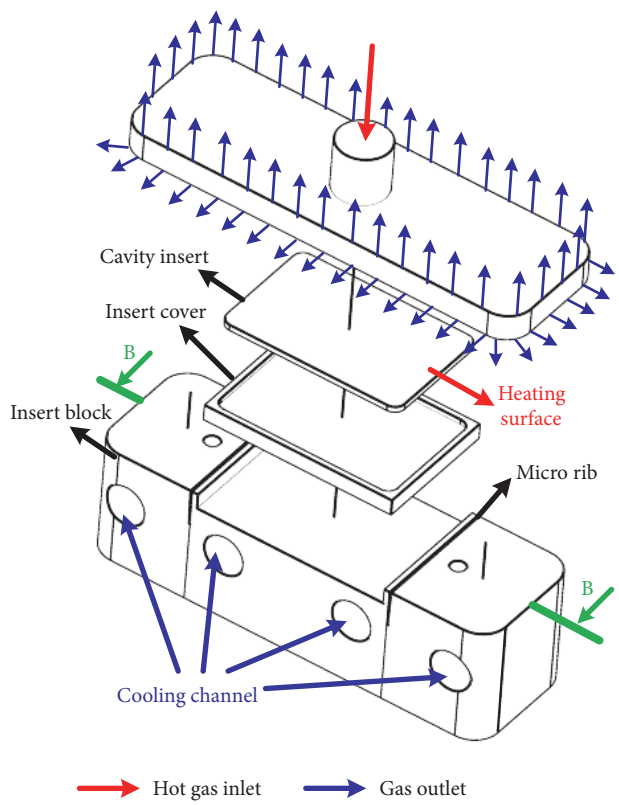

Figure 10: Simulation model of thin rib heating step.

Company) were used with the material properties as in Table 3.

Using the infrared camera, we determined the temperature distribution of the melt flow length mold (Figure 14). This shows that with heating times of 5, 10, 15, and 20 s, at the beginning of melt filling step, the temperature of the cavity surface is maintained at 62.8°C, 94.9°C, 121.2°C, and 133.7°C, respectively. In addition, the uniformity of the temperature distribution was clearly improved after the heating step. This result could be explained by the heat conduction of the mold insert. In this period, the thermal energy would have transferred from the higher temperature region to the lower temperature region. Therefore, the temperature distribution of the mold insert would be more uniform. In the experiment, the temperature difference was less than 5°C for all cavity areas (175 mm × 12 mm). This degree of temperature uniformity is much improved over that of our former research [15–17] and could help reduce the warpage of plastic products. The result also indicates that with a proper layout of the gas gates, Ex-GMTC could be applied to the complex geometry of the mold cavity.

Experimentally, the molding process was operated with different heating times. The plastic components were evaluated, as shown in Figures 15 and 16. With the plastic material and molding parameters shown in Table 3, the experiment was performed with melt flow thicknesses of 0.2, 0.4, and 0.6 mm. The results show that the melt flow length was improved

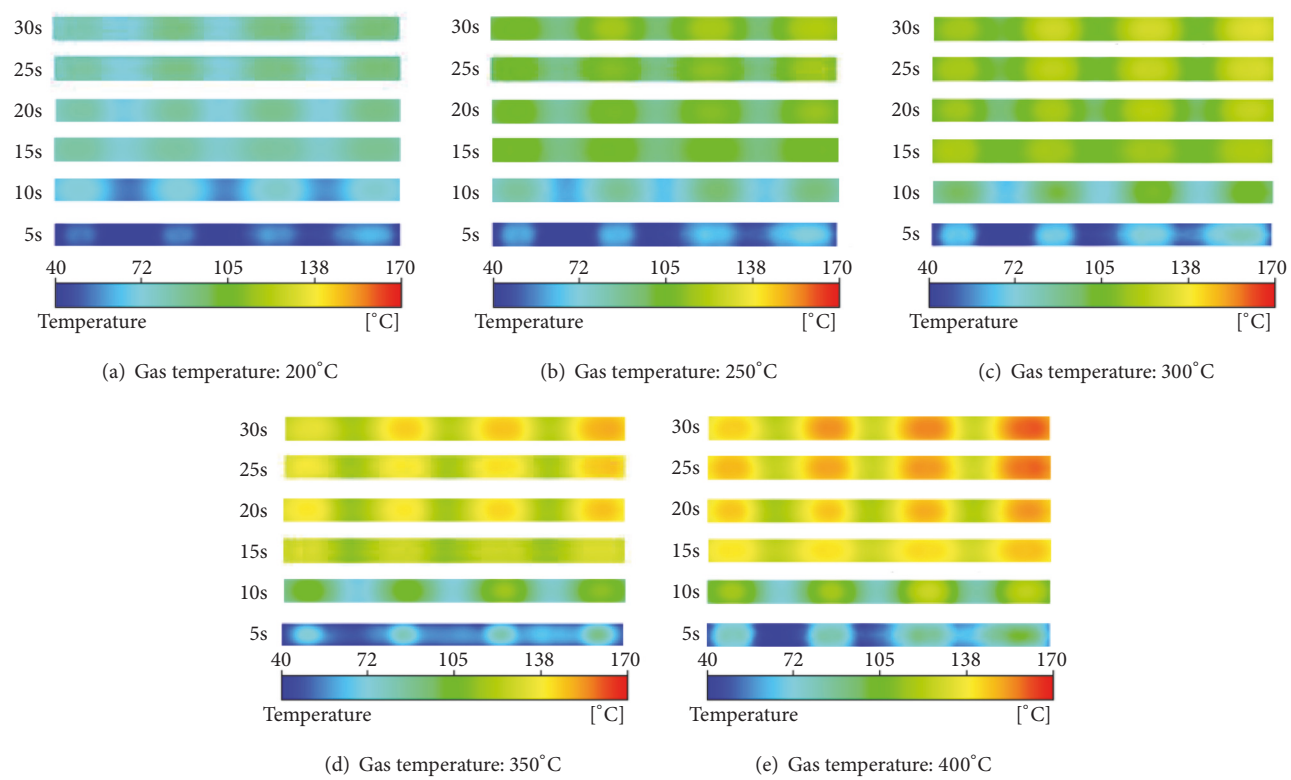

Figure 11: Temperature distribution at the cavity surface of the melt flow length mold after 30 s heating at different gas temperatures.

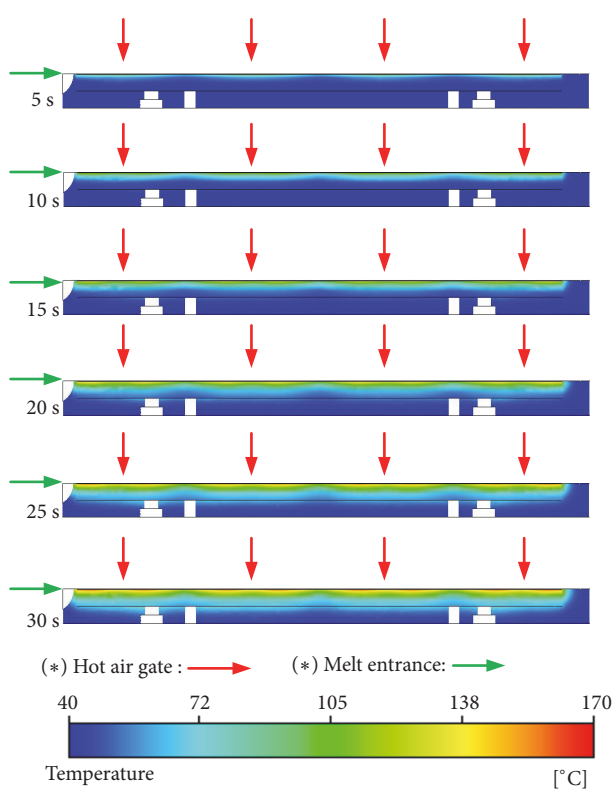

Figure 12: Temperature distribution at the cross section A-A with the gas heating of 400°C.

with the application of Ex-GMTC and a heating time between 5 and 20 s. The improvement is clearer with heating times of 15 and 20 s because the cavity surface temperature was heated to over 110°C in these cases, which is higher than the glass transition temperature of both the PP and ABS materials (Table 4). The percentage improvement in flow length was calculated and is shown in Figure 17. The results show that by applying Ex-GMTC for a 0.6 mm flow thickness, the melt flow length could be improved by 23.5% with the PP material and 22.3% with the ABS material. With the 0.2 mm flow thickness, the flow length increased from 37.85 to 41.32 mm with the PP material and from 14.54 to 15.8 mm with the ABS material.

3.3. Improving the Thin Rib Filling Step by External Gas-Assisted Mold Temperature Control. To assess the efficiency of Ex-GMTC on the injection molding cycle, the mold for a thin rib product was used. The dimensions of this product are shown in Figure 8, with rib thickness varied from 0.3 to 0.5 mm and a rib height of 7.0 mm. The melt material was ABS. For the common injection molding process, mold temperature should be set in the range 20°C to 80°C. However, with a thin wall product, the mold temperature must be set as high as possible to allow for complete filling of the cavity. This readily allows flow because of the reduction of the freeze layer of the melt flow [5]. However, when the mold temperature is high, energy wastage will also be high; in addition, other issues such as warpage and flashing can become evident. To mitigate such

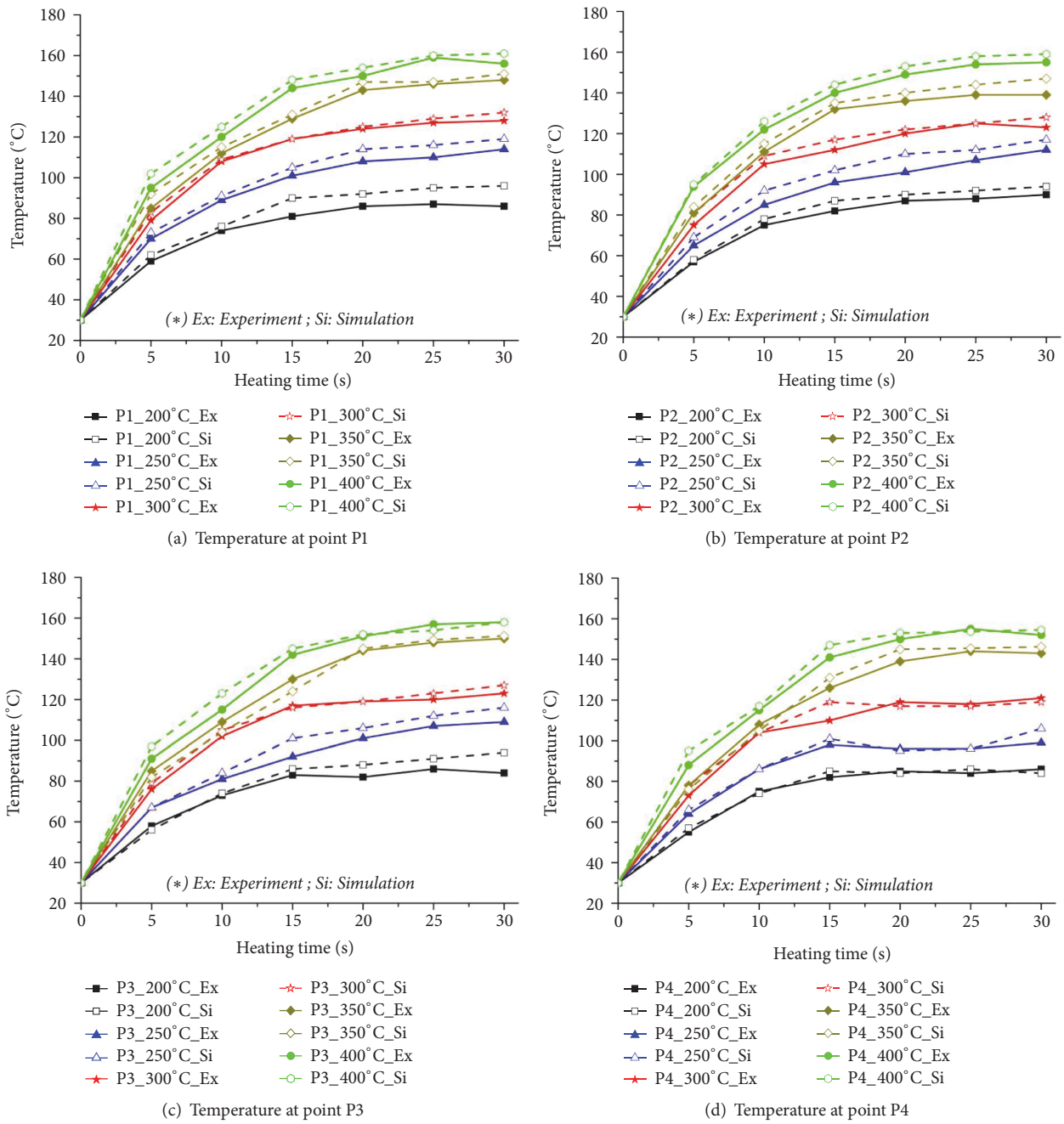

Figure 13: Temperature history at four points with different gas sources.

issues, local mold temperature control was presented in this study with the Ex-GMTC method. Rather than maintaining all mold plates at a high temperature, Ex-GMTC is applied to the cavity area by local gas preheating at the beginning of the molding cycle. The high temperature at the cavity center will reduce the pressure drop of the melt flow as it enters the mold cavity [2, 4]. Figure 9 shows the cavity plate, which includes the cavity area and the melt entrance area.

With the above structure, the area at the cavity center was redesigned with a steel insert to improve the heating efficiency. This insert had dimensions of $40 \times 25 \times 1.0\ \text{mm}^3$. A gas drier with one gate and a gas temperature of 400°C were used for these experiments. To observe the influence of Ex-GMTC on the filling step of the thin rib, the common molding cycle was initially operated with molding temperatures from 45°C to 75°C. In these cases, the mold temperature controller was used with water flow inside the cooling channel. Then, Ex-GMTC was applied with heating times from 4 to 10 s. After the heating step, the melt was filled into the cavity after 6 s for the mold closing. All thin rib experiments used the same ABS material shown in Table 3.

To study the heating step for the thin rib mold, the temperature of the cavity surface was measured at three points, as shown in Figure 9. By experiment, the temperature

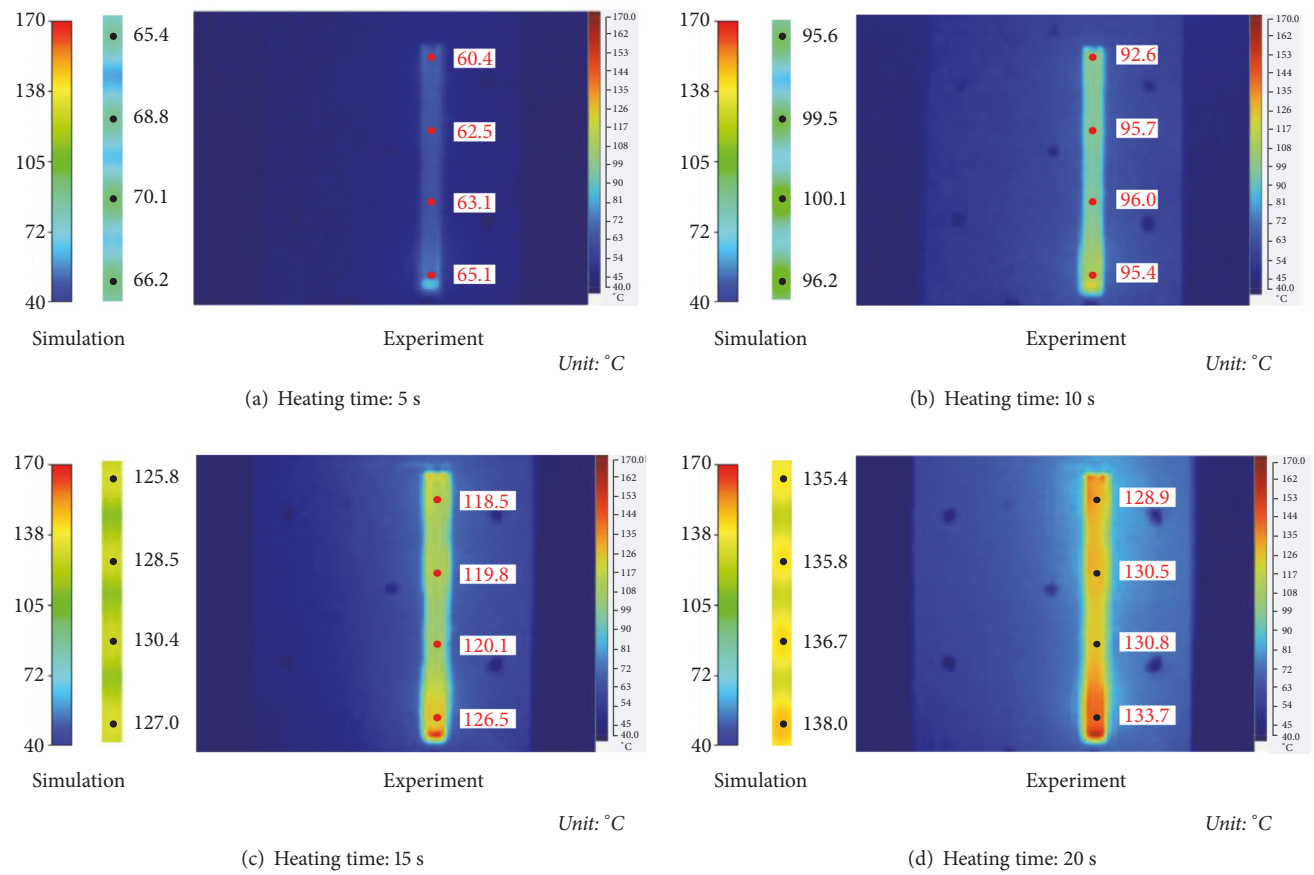

(a) Heating time: 5 s

(b) Heating time: 10 s

(c) Heating time: 15 s

(d) Heating time: 20 s

Figure 14: Temperature distribution of the melt flow mold at the beginning of melt filling step.

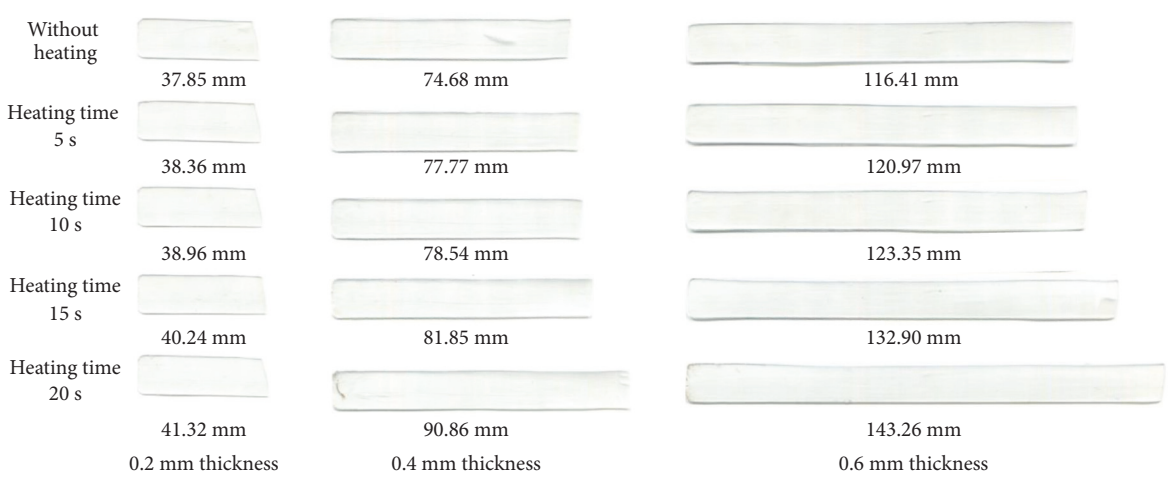

Figure 15: Experimental results for melt flow length with the polypropylene material at different heating times.

histories are given in Table 4 and Figure 18. The temperature histories in Figure 18 show that at the end of the heating step the mold temperature reached 112.0, 121.3, 132.5, and 140.8°C at heating times of 4, 6, 8, and 10 s, respectively. In addition, after 6 s for mold closure, the temperature of the heating surface decreased by about 10°C with the thin rib mold. To verify the temperature uniformity, the thermal camera was used to determine the temperature distribution in the thin rib mold at the end of the heating step. These results are shown in Figure 20. The results show that the temperature uniformity was very good, and the heating process influences only the heating area. For observing the temperature distribution and uniformity along the thickness of mold, the heating step was simulated with the gas heating of 400°C and the simulation

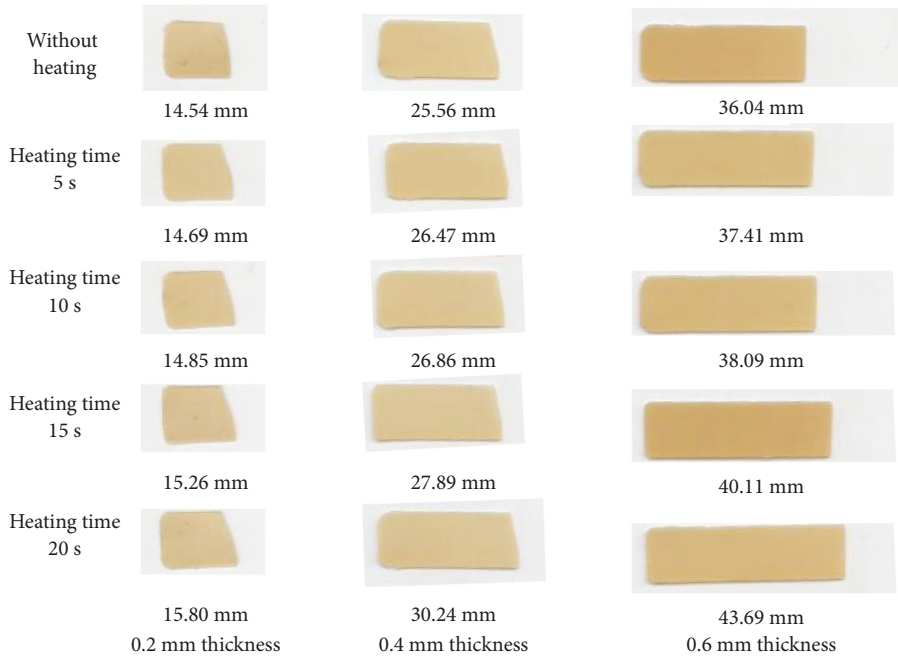

Figure 16: Experimental results for melt flow length with the acrylonitrile butadiene styrene material at different heating times.

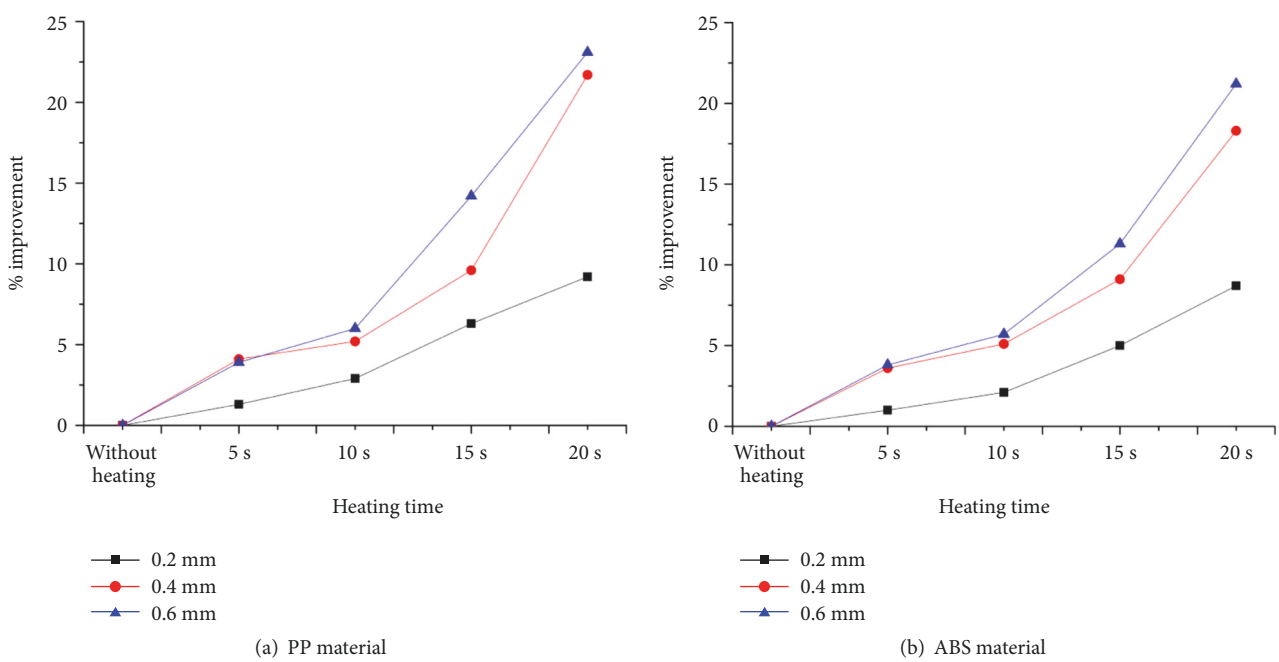

Figure 17: Improvement of melt flow length with the polypropylene and acrylonitrile butadiene styrene materials at different heating time.

model as in Figure 10. The temperature distribution at the cross section B-B was shown in Figure 19. According to this result, the highest temperature was located at the center surface of cavity insert. The mold surface of the rib is not close to the gas heating gate, so, the heating effect is not as clear as the cavity insert. Both simulation and experimental results show that the temperature difference between the three points was less than 10°C. The temperature difference between Point 1 and Point 3 was lower than 3.2°C. The more consistent the temperature between Points 1 and 3, the more balanced the melt filling into the two ribs. In addition, the temperature at the center heating area (Point 2) was always higher than that at the other points. This is because of the closer proximity of the gas gate to Point 2 than to the other points.

At each mold temperature, the molding cycle was performed 20 times to reach system stability, before the next

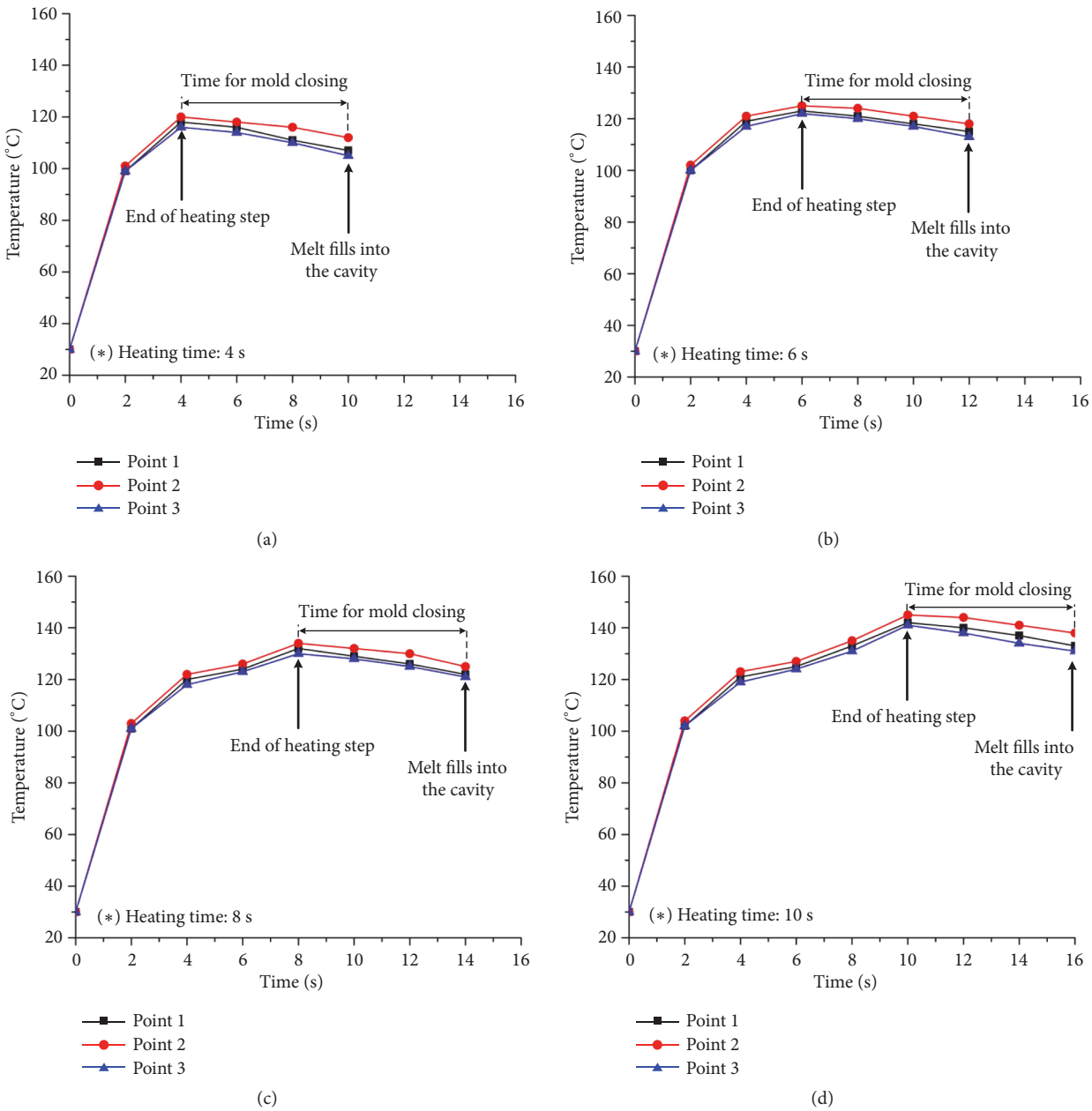

Figure 18: Temperature histories of the thin rib mold surface at three points.

10 cycles were used for comparing rib height. After the molding step, the molding samples were collected and rib heights measured. The results are shown in Figures 21 and 22. According to these results, when the mold temperature increased from 45°C to 75°C, the rib height increased from 2.8 to 4.2 mm. When Ex-GMTC was used with 400°C gas, although the highest temperature was focussed on the cavity insert (Figure 19), the improvement of thin rib was observed clearly. In detail, when the mold temperature varied from 112.0°C to 140.8°C, the thin rib height reached a maximum of 7.0 mm. This development is due to the reduction of the frozen layer when the melt flows through the cavity insert, which helps to increase the filling pressure at the thin rib area. Figure 22 also shows that the height of two ribs was different when using the mold temperature controller with hot water flow inside the cooling channel. This is because of the nonsymmetry of the mold structure; the temperature distribution inside the mold was impacted, especially in the lower mold temperature case. On the contrary, with Ex-GMTC, the heating only affected the molding surface; therefore, the mold structure had almost no influence on the heating result. As such, the height of two thin ribs was more uniform than with the hot water control method.

4. Conclusions

In this research, external gas-assisted mold temperature control (Ex-GMTC) was applied to the injection molding

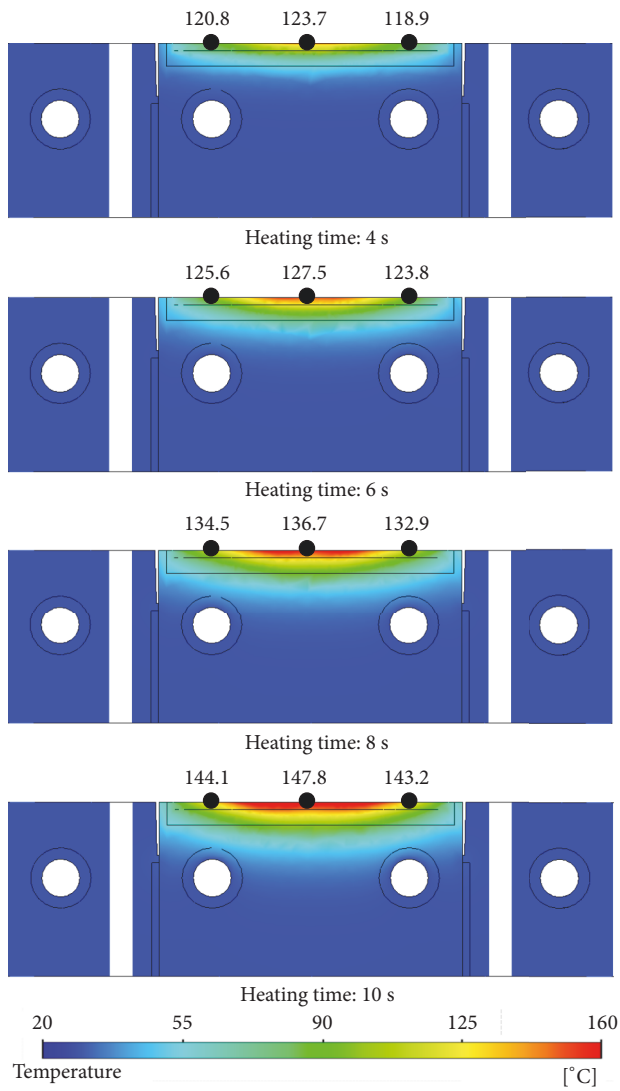

Figure 19: Temperature distribution at the cross section B-B with the thin rib model.

cycle to improve mold filling ability. The simulations and experiments were performed with molds of melt flow length and thin rib. For the mold of melt flow length, the gas temperature was varied from 200°C to 400°C and the molding cycle was operated at component thicknesses of 0.2, 0.4, and 0.6 mm. With the thin rib mold, Ex-GMTC was performed using 400°C gas at the center of the cavity. The filling of melt into the thin rib was observed when using (i) a mold temperature controller with hot water flowing inside the cooling channel and (ii) Ex-GMTC. Based on the results, the following conclusions were obtained:

(i) With a length of 175 mm, the cavity surface of the melt flow length mold showed a relatively balanced heating process when using four hot gas gates, although there were some higher temperature regions near the gates. Heating efficiency was high at the beginning of the heating step; however, after 20 s, the temperature increase slowed. This result was because of heat convection between the hot gas and the mold surface. The highest heating rate achieved was 6.4°C/s with the 400°C gas.

(ii) Because of heat convection, the simulations and experiments showed that Ex-GMTC has a limitation in terms of heating efficiency. Nevertheless, with the melt flow length mold, the mold surface reached 158.4°C, at which temperature almost all of the melt could flow easily into the cavity.

(iii) By applying Ex-GMTC for the 0.6 mm flow thickness, the melt flow length could be improved by 23.5% with the PP material and 22.3% with the ABS material. With the 0.2-mm flow thickness, the flow length also increased from 37.85 to 41.32 mm with the PP material and from 14.54 to 15.8 mm with the ABS material.

(iv) With the thin rib mold, when the mold temperature increased from 45°C to 75°C, the rib height was increased from 2.8 to 4.2 mm. When the Ex-GMTC

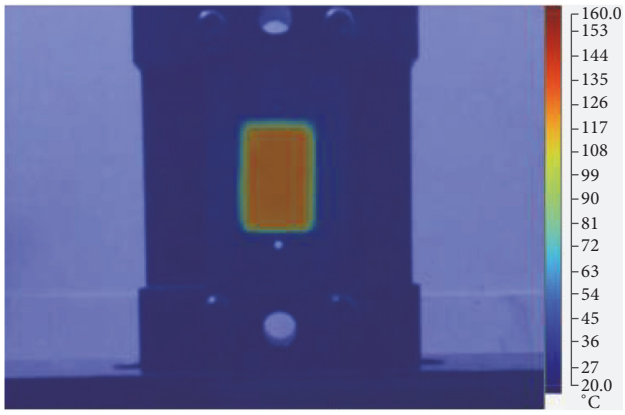

(a) Heating time: 4 s, Max Temperature: 112.0°C

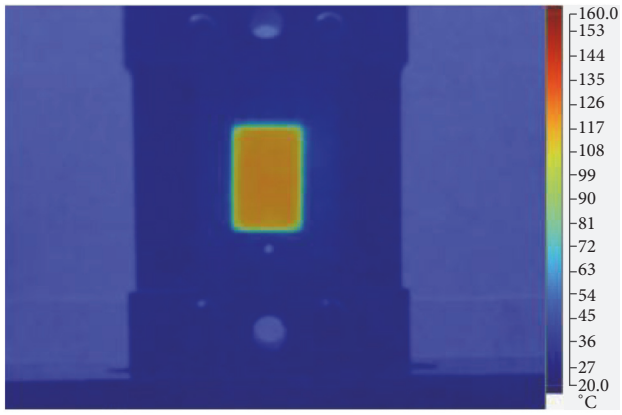

(b) Heating time: 6 s, Max Temperature: 121.3°C

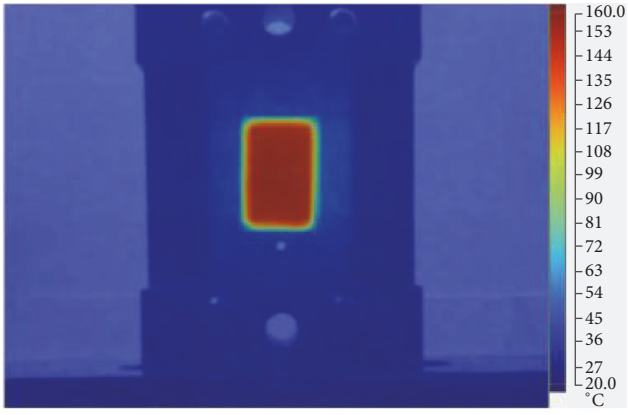

(c) Heating time: 8 s, Max Temperature: 132.5°C

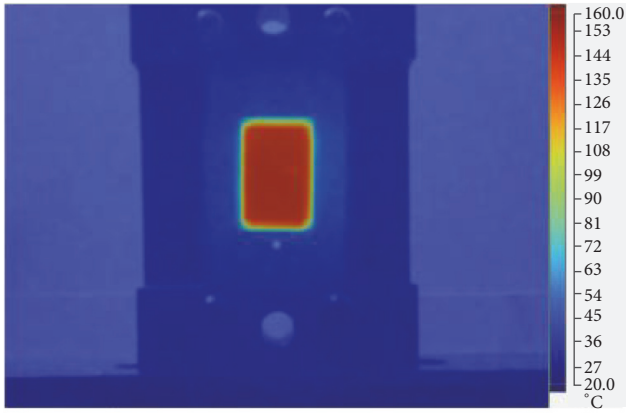

(d) Heating time: 10 s, Max Temperature: 140.8°C

Figure 20: Temperature distribution at the end of the heating step for the thin rib cavity at different heating times.

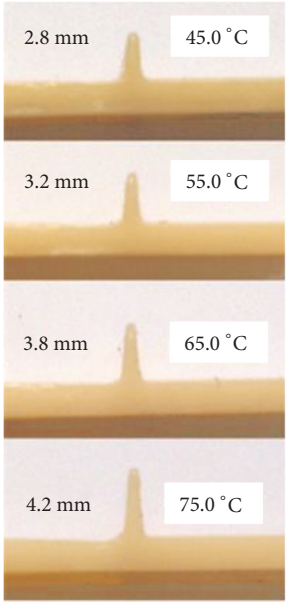

(a) Mold temperature control with the hot water

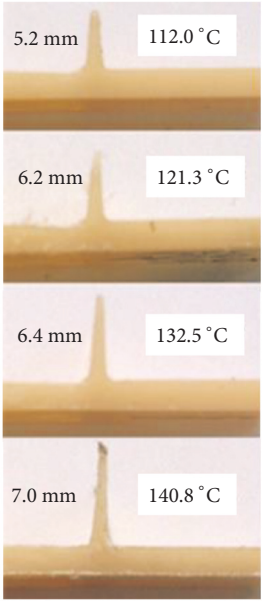

(b) Mold temperature control with Ex-GMTC

Figure 21: Measurement of thin rib height at different cavity temperatures.

Table 4: Experimental results for cavity temperature with the thin rib mold at different heating times.

Measuring point	Measuring time (s)	Heating time (s)			
		4	6	8	10
1	0	30	30	30	30
	2	99.2	100.2	101.2	102.2
	4	118.6	119.9	120.1	121.1
	6	116.4	123.4	124.2	125.6
	8	111.1	121.5	132.6	133.5
	10	107.0	118.0	129.5	142.3
	12		115.5	126.7	140.8
	14			122.0	137.2
	16				133.0
2	0	30	30	30	30
	2	101.2	102.1	103.3	104.2
	4	120.6	121.9	122.2	123.6
	6	118.5	125.5	126.6	127.2
	8	116.7	124.4	134.7	135.1
	10	112.1	121.9	132.4	145.8
	12		118.4	130.2	144.2
	14			125.1	141.6
	16				138.1
3	0	30	30	30	30
	2	99.2	100.3	101.2	102.3
	4	116.2	117.5	118.3	119.9
	6	114.1	122.4	123.4	124.8
	8	110.4	120.1	130.5	131.1
	10	105.6	117.2	128.9	141.4
	12		113.2	125.7	138.3
	14			121.1	134.5
	16				131.1
Heating time				Mold closing time	

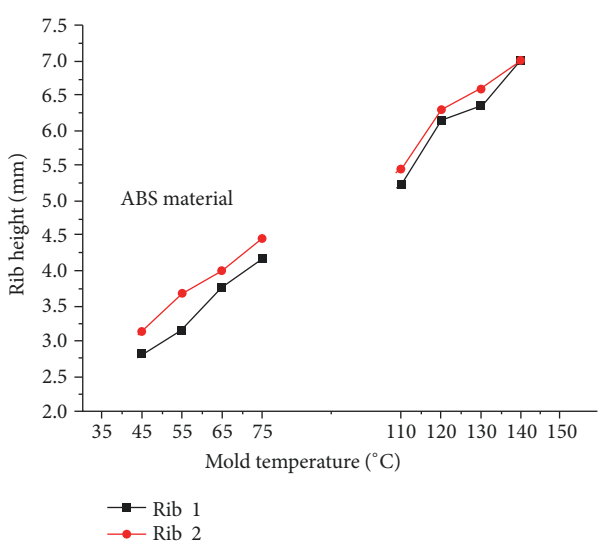

Figure 22: Improvement of thin rib height at different cavity temperatures.

was used, the mold temperature varied from 112.0°C to 140.8°C and the thin rib height reached 7.0 mm. Because the Ex-GMTC was not influenced by mold structure, the heating method supported a better temperature distribution than that of the hot water controller method; as a result, a better balance in melt flow could be achieved.

Data Availability

The data used to support the findings of this study are available from the corresponding author upon request.

Conflicts of Interest

The authors declare that they have no conflicts of interest.

Authors' Contributions

Phan The Nhan and Pham Son Minh conceived of the presented idea and developed the simulation and experimental methods. Phan The Nhan and Thanh Trung Do verified the simulation results. All authors discussed the results and contributed to the final manuscript.

Acknowledgments

This research was supported by the Ministry of Education and Training, Vietnam; the Ministry of Science and Technology, Vietnam; and HCMC University of Technology and Education, Hochiminh City, Vietnam. The authors are grateful to Mr. Nguyen Ho, Mr. Bui Huu Manh, Mr. Nguyen Thanh Nhan, Mr. Dang Ngoc Son, and Mr. Tran Van Tron for their help in conducting the study experiments.

References

[1] L. Zema, G. Loreti, A. Melocchi, A. Maroni, and A. Gazzaniga, "Injection molding and its application to drug delivery," *Journal of Controlled Release*, vol. 159, no. 3, pp. 324–331, 2012.

[2] M. Vázquez and B. Paull, "Review on recent and advanced applications of monoliths and related porous polymer gels in micro-fluidic devices," *Analytica Chimica Acta*, vol. 668, no. 2, pp. 100–113, 2010.

[3] M.-S. Huang and Y.-L. Huang, "Effect of multi-layered induction coils on efficiency and uniformity of surface heating," *International Journal of Heat and Mass Transfer*, vol. 53, no. 11-12, pp. 2414–2423, 2010.

[4] S.-C. Nian, C.-Y. Wu, and M.-S. Huang, "Warpage control of thin-walled injection molding using local mold temperatures," *International Communications in Heat and Mass Transfer*, vol. 61, no. 1, pp. 102–110, 2015.

[5] S. Meister and D. Drummer, "Affecting the ageing behaviour of injection-moulded microparts using variothermal mould tempering," *Advances in Mechanical Engineering*, vol. 2013, Article ID 407964, 7 pages, 2013.

[6] F. Baruffi, M. Calaon, and G. Tosello, "Effects of micro-injection moulding process parameters on accuracy and precision of thermoplastic elastomer micro rings," *Precision Engineering*, vol. 51, pp. 353–361, 2018.

[7] M.-C. Jeng, S.-C. Chen, P. S. Minh, J.-A. Chang, and C.-S. Chung, "Rapid mold temperature control in injection molding by using steam heating," *International Communications in Heat and Mass Transfer*, vol. 37, no. 9, pp. 1295–1304, 2010.

[8] W. Guilong, Z. Guoqun, L. Huiping, and G. Yanjin, "Analysis of thermal cycling efficiency and optimal design of heating/cooling systems for rapid heat cycle injection molding process," *Materials & Design*, vol. 31, no. 7, pp. 3426–3441, 2010.

[9] S. Liparoti, A. Sorrentino, and G. Titomanlio, "Fast cavity surface temperature evolution in injection molding: control of cooling stage and final morphology analysis," *RSC Advances*, vol. 6, pp. 99274–99281, 2016.

[10] P.-C. Chang and S.-J. Hwang, "Simulation of infrared rapid surface heating for injection molding," *International Journal of Heat and Mass Transfer*, vol. 49, no. 21-22, pp. 3846–3854, 2006.

[11] S.-C. Chen, W.-R. Jong, Y.-J. Chang, J.-A. Chang, and J.-C. Cin, "Rapid mold temperature variation for assisting the micro injection of high aspect ratio micro-feature parts using induction heating technology," *Journal of Micromechanics and Microengineering*, vol. 16, no. 9, pp. 1783–1791, 2006.

[12] D. Yao, T. E. Kimerling, and B. Kim, "High-frequency proximity heating for injection molding applications," *Polymer Engineering & Science*, vol. 46, no. 7, pp. 938–945, 2006.

[13] S.-C. Chen, P. S. Minh, J.-A. Chang, S.-W. Huang, and C.-H. Huang, "Mold temperature control using high-frequency proximity effect induced heating," *International Communications in Heat and Mass Transfer*, vol. 39, no. 2, pp. 216–223, 2012.

[14] H.-L. Lin, S.-C. Chen, M.-C. Jeng, P. S. Minh, J.-A. Chang, and J.-R. Hwang, "Induction heating with the ring effect for injection molding plates," *International Communications in Heat and Mass Transfer*, vol. 39, no. 4, pp. 514–522, 2012.

[15] S.-C. Chen, R.-D. Chien, S.-H. Lin, M.-C. Lin, and J.-A. Chang, "Feasibility evaluation of gas-assisted heating for mold surface temperature control during injection molding process," *International Communications in Heat and Mass Transfer*, vol. 36, no. 8, pp. 806–812, 2009.

[16] S.-C. Chen, C.-Y. Lin, J.-A. Chang, and P. S. Minh, "Gas-assisted heating technology for high aspect ratio microstructure injection molding," *Advances in Mechanical Engineering*, vol. 2013, Article ID 282906, 10 pages, 2013.

[17] S.-C. Chen, P. S. Minh, and J.-A. Chang, "Gas-assisted mold temperature control for improving the quality of injection molded parts with fiber additives," *International Communications in Heat and Mass Transfer*, vol. 38, no. 3, pp. 304–312, 2011.

[18] H. D. Baehr and K. Stephan, *Heat and Mass Transfer*, Springer, New York, 2nd edition, 2006.

Hindawi
Advances in Polymer Technology
Volume 2019, Article ID 4264701, 8 pages
https://doi.org/10.1155/2019/4264701

Research Article

Coating Performance of Water-Based Polyurethane-Acrylate Coating on Bamboo/Bamboo Scrimber Substrates

Jianfeng Xu,[1,2] Ru Liu,[2] Huagui Wu,[2] Hongyun Qiu,[2] Yanglun Yu,[2] and Ling Long [1,2]

[1] *Research Institute of Forestry New Technology, Chinese Academy of Forestry, Haidian 100091, Beijing, China*
[2] *Research Institute of Wood Industry, Chinese Academy of Forestry, Haidian 100091, Beijing, China*

Correspondence should be addressed to Ling Long; longling@caf.ac.cn

Received 14 December 2018; Accepted 13 February 2019; Published 21 March 2019

Guest Editor: Changlei Xia

In this paper, a kind of high solid content water-based polyurethane-acrylate (PUA) coating was synthesized in laboratory. Bamboo, bamboo scrimber, and heat-treated bamboo scrimber were selected as substrates and coated with the PUA coating. The coating properties of those materials were investigated. The results showed that PUA coating could well cover the surface of the three kinds of materials. However, the coating performances varied among these substrates due to their different chemical and morphological surfaces. Due to the densified structures, small pores, and improved hydrophobicity of bamboo scrimber, it was difficult for PUA coating to wet and penetrate into the substrate, where the smaller contact angle and penetration depth were obtained compared with bamboo. In contrast, heat-treated one had better hydrophilicity and smaller contact angle with PUA coating than pure bamboo scrimber. Therefore, the coating performance of heat-treated bamboo scrimber was better with lower average roughness value. However, the adhesion classification between the coating and all substrates was 2 (with 5-15% cross-cut area of flaking along the edges).

1. Introduction

Bamboo is considered as an abundantly available, biodegradable, and sustainable natural resource, which is widely used in papermaking, decking, flooring, building, and so on, because of its rapid growth, good flexibility, and short production period [1–5]. The bamboo elements are composed of bamboo fibers, parenchyma cells, and vessels. It is known that the strength and modulus of bamboo fibers are much higher than others. Therefore, when load applies, the weak constitute is easy to break [6]. The performance defects of bamboo had been effectively compensated by Yu et al. [7] with a novel composite, namely, the bamboo scrimber. Compared with other bamboo composites, the bamboo scrimber has comparatively higher raw material utilization rate because the bamboo core and bamboo yellow were all utilized. The bamboo scrimber has a desirable texture, high hardness, and longitudinal strength properties [8–11].

Coating can protect and beautify bamboo and bamboo products. It is generally considered that the whole coting process can be divided into several steps, wetting of substrate, leveling, infiltrating, and drying into film [12–14]. The hydrophilicity and porosity of substrate has great impact on the coating process and coating performance [15–17]. The bamboo scrimber is a kind of high strength bamboo product formed by changing the cell structure of bamboo under the dual action of pressure and resin, which led to the densification of material, less the hydrophilic groups, and the parenchyma and fiber filled by adhesive of bamboo. For heat-treat one, improved hydrophobicity is achieved. Therefore, the changes may affect the coating performance, especially the water-based coating.

Up to present, few research focus on the coating technology of bamboo scrimber, especially the water-based coating. Polyurethane-acrylate resin (PUA) contains acrylic functional groups and urethane bonds. And its coating has high abrasion resistance, adhesion, flexibility, and excellent optical properties and weather resistance. Therefore, in this paper, bamboo, bamboo scrimber, and heat-treated bamboo scrimber were chosen as substrates and coated with a self-made water-based PUA coating. The PUA made in laboratory has more hydrophilic groups in the molecular chains, such

Table 1: Reagents for water-based PUA coating.

Reagent	Type	Abbreviation	Manufacturer
Ammonium persulfate	Initiator	APS	Xilong Chemical Co. Ltd. (Guangzhou, China)
Acrylate acid	Monomer	AA	As above
Styrene	Monomer	ST	As above
Ethyl acrylate	Monomer	EA	As above
Hydroxyethyl acrylate	Monomer	HEA	As above
Toluene-2,4-diisocyanate	Monomer	TDI	As above
polyethylene glycol (M_n: 400)	Monomer	PEG-400	As above
Dibutyltin dilaurate	Catalyser	DBTD	As above
γ-aminopropyltriethoxysilane	Silane	KH550	Qufu Chengguang Chemical Co., Ltd (Shandong, China)
Polyether siloxane copolymer composition	Defoamer agent	/	Tianjin Jinke Fine Chemical Institute (Tianjin, China).
N-methyl-2-pyrrolidone	Solvent	–	As above
2-hydroxy-methylphenylpropan-1-one	Photoinitiator	/	As above

as carboxyl, and the PUA resin can dissolve well in water and different solid content PUA coatings can be obtained. The coating properties and the different mechanism among those materials were investigated, which aimed to get effective method for better process conditions of water-based coating for bamboo scrimber.

2. Materials and Methods

2.1. Materials. Moso bamboo (*Phyllostachys pubescens*), age 3-4 years, was taken from Jian'ou Forest Reserve, Fujian province, southeast of China. The reagents for water-based polyurethane-acrylate resin (PUA) coating are listed in Table 1.

2.2. Preparation of Water-Based PUA Coating. The monomers of 24 g AA, 4 g ST, and 7 g EA with 44 g distilled water were blended in a three-neck glass reactor at 150 r/min. Afterwards, the initiator of 8 g APS was added at 10 wt%. In the next 70–90 min, the rest of 96 g AA, 16 g ST, and 133 g EA were dripped into the reactor. Afterwards, the rest of 32 g APS and 36 g KH550 was dripped into the reactor within 90–110 min. The reactor was heated up to 85°C and kept for 4 h. The next step was to graft the prepolyurethane onto the prepolyarylate chain. 100 g TDI, 200 g PEG-400, and 8 g DBTD were dissolved in *N*-methyl-2-pyrrolidone solvent and blended into a three-neck glass reactor at 150 r/min. The reactor was heated to 40°C. During stirring, 66 g HEA was dripped into the reactor within 2 h. The prepolyurethane emulsion was obtained. Afterwards, both the prepolyarylate and prepolyurethane emulsions were mixed in the three-neck glass reactor and blended at 150·r/min. The reaction was heated up to 85°C and kept for 2 h. The PUA emulsion was obtained after cooling and filtration. 2% defoamer agent was added into the emulsion at 100 r/min for 10 min. The PUA waterborne coating was obtained with the solid content of 90 wt% and viscosity of 200 mPa·s. It was kept in a black bottle and protected against light.

2.3. Heat Treatment of Bamboo. According to actual industrial production and previous studies [18–20], the hot dry air treatment was employed on bamboo slivers. The details could be found in previous study [11], namely, the green bamboo was sawn into a bamboo tube with a length of 2600 mm and then split longitudinally into two semicircular tubes. The inner nodes were removed and the semicircular bamboo tubes were pushed into the fluffer as well as removed the wax siliceous surfaces parallel to the grain direction with a series of dotted and linear shaped cracks, thereby forming the net-structured bamboo bundles, where the diameter of bamboo fiber bundle was lower than 0.2 mm. The bamboo bundles were oven-dried at 103°C and weighed before the thermal treatment. The dried samples were placed in an iron bucket in an oven and heated at 180°C for 8 h. For fear of flame, the samples in the bucket were covered by sand as protecting medium. Afterwards, the samples were taken out and washed with water and oven-dried again.

2.4. Fabrication of Bamboo Scrimber. An impregnation process was employed to load phenol-formaldehyde (PF) resin. The target PF loading was 13 wt%. The bamboo bundles were immersed into the PF resin for 6 min at room temperature at PF concentration of 22 wt%. Afterwards, the bundles were taken out and leaked for about 6 min to remove excessive resin and weighed. As stated, the amounts of resin loading can be controlled by the solid content of resin and weight gains. The immersed bamboo bundles were dried in an oven at 70°C to moisture content of 12% for manufacturing. The manufacturing of bamboo scrimber was carried out by a cold-in and cold-out process. The bamboo bundles were weighed at desired density of 1.30 g/cm^3. They were assembled along the grain direction in the hot-pressing mold. When the temperature of the hot plate heated up to 60°C, the bamboo mat was sent into the press. The pressure was kept at 3.5-7.0 MPa according to relative density at 140°C for 30 min to cure the mat. Afterwards, cold water was introduced into the hot plate and cooled down to 60°C. The pressure was released and the cured mat was removed from the press. The nominal dimension of the bamboo scrimber was 2600 × 1300 × 16 mm^3. After then, all the mats were cut into required dimensions and conditioned in a room at 20°C and 65% RH for 2 weeks for further tests.

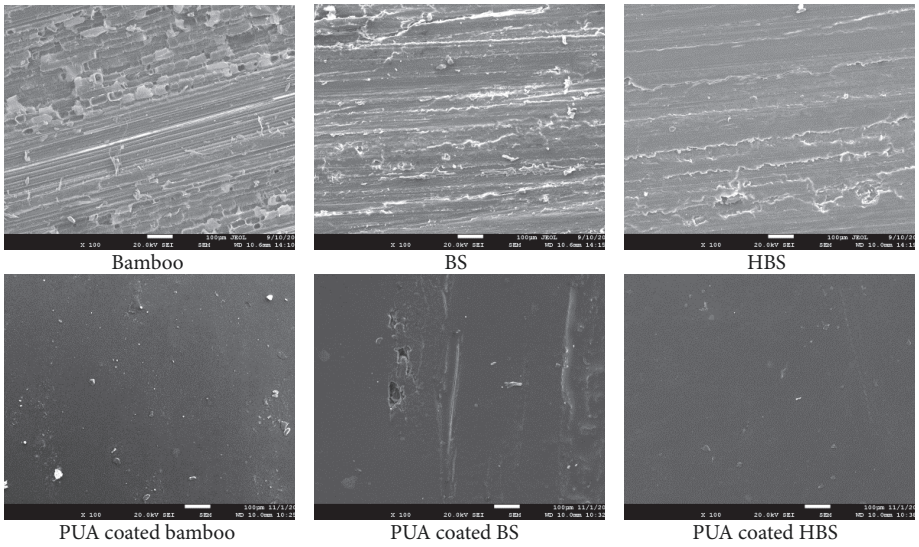

Figure 1: SEM of bamboo, BS, and HBS and their coated samples.

2.5. Coating of Bamboo and Bamboo Scrimber. The moso bamboo, bamboo scrimber (BS), and heat-treated bamboo scrimber (HBS) were coated by semiautomatic roll coater (BGD 218, BIUGED instruments, China) according to ISO standard 15528: 2011 and the relative film thickness requirement. In theory, the dry film thickness is 18 μm. The film sample was then dried in a cool, dry, dark environment for 1 week before use [21].

2.6. Characterizations and Tests. The characterizations of the samples were carried out by scanning electron microscope coupled with energy dispersed X-ray analysis, atomic force microscopy (AFM), Fourier transform infrared spectroscopy equipped with an attenuated total reflection (ATR-FTIR), and X-ray photoelectron spectra (XPS) analyses [21].

The microstructures of the above samples were observed by scanning electron microscope (JEOL JSM-6301F, Japan) with an acceleration voltage of 20 kV. The samples were sputter-coated with gold. Energy dispersed X-ray analysis (EDXA, Horiab 7021-H, Japan) was carried out in mapping mode. The images and distributions of elements N which were mainly from PUA resin were captured digitally to allow for further analysis of impregnation of PUA in each substrate.

The surface morphologies were captured by AFM and collected by a scanning probe microscope in contact mode.

The chemical groups of the samples were examined by ATR-FTIR (BRUKER Vertex 70v, Germany).

XPS analysis of the specimens were performed on Escalab 250Xi (Thermo Scientific, USA) to determine the number of functional groups present on the surface with a pass energy of 10 eV and nonmonochromatic MgKα and AlKα X-radiations (hγ=1253.7 eV and 1486.7 eV, respectively). A current of 10 mA and a voltage of 13 kV were used. The survey scans were collected from the binding energy range of 0 to 1350 eV. The layers were mounted onto a holder with double-sided adhesive tape and placed in vacuum ranging from 1.33 $\times 10^{-6}$ to 1.33 $\times 10^{-5}$ Pa. The test sample area was 10 $\times$ 10 mm^2 and the atomic percentages of the elements present were derived from the spectra in this area.

The contact angle of those specimens was measured according to ISO 15989: 2004 by contact angle meter (ISO, 2004; Krüss K11MK4, Germany), when the test solutions (polyurethane-acrylate coating) were diluted to 70 wt%.

The adhesion classification of coating films was measured according to ISO 2409: 2013 standard methods by a cross-cut test. Classification 0: the edges of the cuts are completely smooth; none of the squares of the lattice is detached. Classification 1: detachment of small flakes of the coating at the intersections of the cuts. A cross-cut area not greater than 5% is affected. Classification 2: the coating has flaked along the edges and/or at the intersections of the cuts. A cross-cut area greater than 5%, but not greater than 15%, is affected. Classification 3: the coating has flaked along the edges of the cuts partly or wholly in large ribbons, and/or it has flaked partly or wholly on different parts of the squares. A cross-cut area greater than 15%, but not greater than 35%, is affected. Classification 4: the coating has flaked along the edges of the cuts in large ribbons and/or some squares have detached partly or wholly. A cross-cut area greater than 35% but not greater than 65% is affected. Classification 5: any degree of flaking that cannot even be classified by classification 4.

3. Results and Discussion

3.1. Coating Morphologies. The surface morphologies of each sample before and after coating are shown in Figure 1. The figures showed that the microstructure of each substrate was clearly visible before coating, including dense fibrous tissue and looser parenchyma cells. After the recombinant processing, the parenchyma cells of bamboo were destroyed and the cell structure became dense. The surface of the HBS became flatter than BS, which indicated that the permeability and distribution uniformity of the phenolic resin in bamboo were improved by the heat treatment.

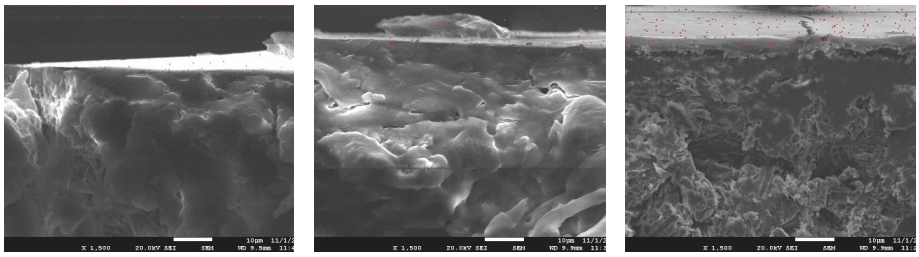

PUA coated bamboo PUA coated BS PUA coated HBS

Figure 2: N-element distributions in PUA coated samples.

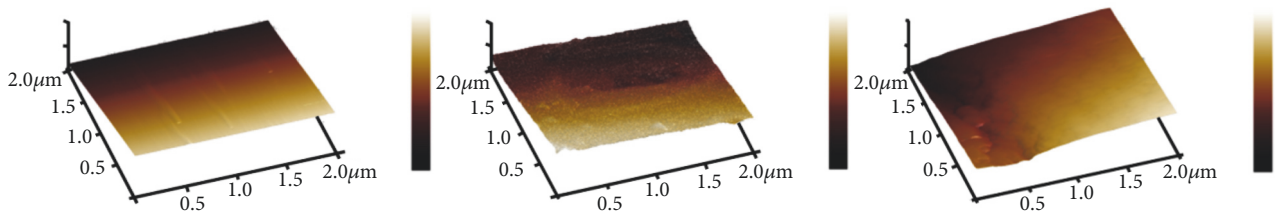

Rq:Ra = 1.35 Rq:Ra = 1.41 Rq:Ra = 1.24

PUA coated bamboo PUA coated BS PUA coated HBS

Figure 3: AFM images of PUA coated samples.

The surface of bamboo and HBS, both coated by polyurethane-acrylate, were well covered by the coatings and the flat coating film achieved, though there were a small amount of micronanoparticles. It might be the coating particles and bubbles, which were generated during the coating penetration into the interior of the substrate during the curing process of the coating film. In case of HS, some bamboo fibers were exposed on the surface, which led to some defects such as bottom leakage. Due to the high density of the BS, weak penetration into the interior of substrate occurred. On the other hand, the free energy of the BS surface was high, which made the coating not evenly spread out. Hence, an agglomeration of the coating film was got after curing.

In order to further analyze the permeability of the coating in bamboo, BS, and HBS, the coated samples were investigated by N-element spectrum scanning by EDXA. The results are shown in Figure 2. The figure showed that most PUA distributed on the surface of the substrate, and just a small amount penetrated into the substrate. On the surface of bamboo, the penetration depth of PUA was about 4 μm, while on the surface of BS, the penetration depth decreased to 2 μm, which indicated that it was difficult for the of PUA resin penetrating into the substrate. It was because that the cells tissue was compacted after the substrate was disintegrated and reorganized. Interestingly, the most penetration depth of PUA resin in HBS increased to 4-5 μm, with partly of 7 μm, which might because of the enlarged pores of HBS during the heat treatment.

The AFM 3D images of surface topography of coated samples are shown in Figure 3. It could be seen that the bamboo, BS, and HBS were well covered by the PUA coating. Smooth surface was obtained, with little defects. Very tiny flow marks, formed on bamboo during curing, were observed. The surface roughness value (Rq:Ra) of coated bamboo was 1.35. The coating film on the BS surface was rough and the average roughness value increased to 1.41. Compared with the others, the surface of the HBS was the smoothest with the lowest roughness value of 1.24, which indicated more uniform distribution of coating on the surface of the HBS was obtained.

3.2. Chemical Characterizations. The ATR-FTIR results of the specimens, including coated and uncoated bamboo, coated and uncoated BS, and coated and uncoated HBS are shown in Figure 4. In Figure 4(a), changes of chemical group peaks were found between raw substrates and coated samples, indicating that there were chemical reactions. However, the results between BS and HBS were not significant. Compared with bamboo, the absorption peaks of –OH at 3420 cm^{-1} of BS and HBS were both obviously weakened, which indicated that the hydrophilicity of BS and HBS decreased. The reason should be explained by the fact that the fiber surface of BS and HBS was well covered by phenolic resin (PF), which was hydrophobic than bamboo fibers [22].

The absorption peak of C=O at 1737 cm^{-1} was the characteristic peak of hemicellulose. And in case of BS and HBS, this peak almost disappeared, which indicated that the hemicellulose and polysaccharide of bamboo degraded during curing. In addition, the C-O absorption peak of BS and HBS at 1043 cm^{-1} increased, and the C-O vibration peak of ester bond at 1265 cm^{-1} shifted to 1240 cm^{-1}, which indicated that aromatic ester bonds and ether bonds formed between phenolic resin and cellulose. The skeleton stretching vibration

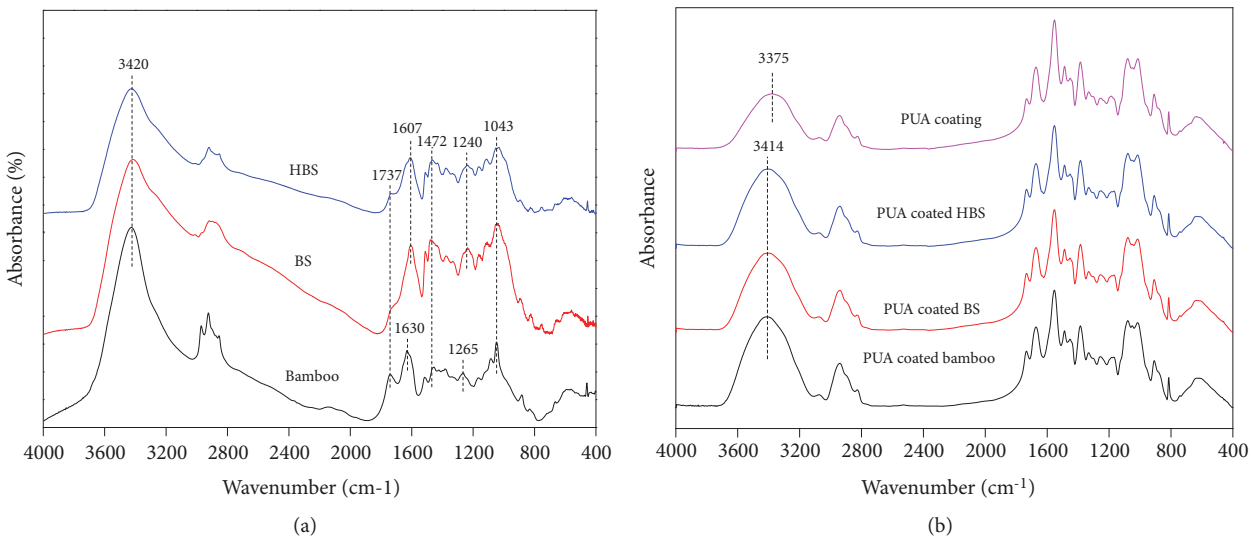

Figure 4: ATR-FTIR spectra of bamboo, BS, HBS (a), and their coated samples (b).

Table 2: Elements percentages of bamboo, BS, HBS, and their coated samples.

Sample	Percentage (%)		
	C	O	N
Bamboo	70.35	26.63	3.02
BS	78.37	19.01	2.62
HBS	81.91	15.88	2.22
PUA coated bamboo	73.47	20.43	4.81
PUA coated BS	74.21	17.61	8.18
PUA coated HBS	81.44	14.38	4.19

peak of lignin aromatic benzene ring C=C at 1630 cm^{-1} of BS and HBS shifted to 1607 cm^{-1}, which was due to the side chain substitution on the lignin benzene ring during heating. All these results suggested new chemical bond was formed in BS and HBS compared with neat bamboo.

Figure 4(b) shows the results of the PUA coated bamboo and BS/HBS samples. Compared with the pure polyurethane-acrylate sample directly dried on the glass plate, the spectrum was basically the same except for the stretching vibration peak of -OH at 3375 cm^{-1}, which was shifted to 3414 cm^{-1}. It was mainly due to the fact that the hydrogen bond formed between the PUA and the -OH of bamboo or BS/HBS, indicating that the PUA coating was well covered on the surface of bamboo, BS, and HBS.

To further analyze the surface chemical changes of these materials, the XPS analysis was carried out. Table 2 showed the percentage results of XPS elements of each sample before and after coated. The atomic percentages of C, O, and N in bamboo were 70.35%, 26.63%, and 3.02%, respectively. After fabricated into bamboo scrimber, the C element increased to 78.37%, while the O element decreased and the N content remained basically. The reason may be associated with the PF resin containing higher C which was added into the bamboo scrimber. The C content of the HBS further increased compared with the BS, and the O element further decreased. It was because heat treatment could degrade the -OH of bamboo, which led to a decrease in the bamboo hydrophilicity. Compared with uncoated bamboo, the quantity of C, O, and N element of coated samples changed, with the percentages of 73.47%, 20.43%, and 4.81%, respectively. Due to PUA coating containing much C and N elements, the content of C and N increased, and the content of O decreased, compared with uncoated sample. The C element of coated BS changed slightly while the N content significantly increased, compared to those of coated bamboo. It was because the PF resin in the reconstituted bamboo could react with the ester groups of the urethane-acrylate, so more amino groups were exposed on the surface of the sample.

In contrast, the C content of the coated HBS increased, while the O content decreased, and the N content changed little. It was because the heat-treatment process reduced the surface content of hydroxyl groups on the bamboo scrimber, simultaneously expanding the substrate porosity. Thus the PUA penetrated inside. Therefore, the PUA coating was well distributed on the substrate surface and was more likely to permeate into the substrate interior. Therefore, differences among each substrate were not significant. In general, HBS had better coating performance than that of BS.

In order to further analyze the binding of C_{1s} in each material, the four peaks were observed, including C1(C-C/C-H), C2(C-O/C-OH), C3(O-C-O/C=O), and C4(O-C=O) [23]. The results are shown in Figure 5 and Table 3. It could be seen from Table 2 that there was no C4 peak except the bamboo scrimber coated by PUA. Although PUA contained some ester bonds, it penetrated well into bamboo and HBS and evenly covered the surface of the substrate. Thus, C4 peak was not detected. On the contrary, it was difficult for PUA to penetrate into bamboo scrimber, which, aggregated on the surface, so C4 peak was detected. The proportions of C1, C2, and C3 of bamboo were 54.82%, 34.78% and 10.40%, respectively. In contrast, the proportion of C1 of BS increased

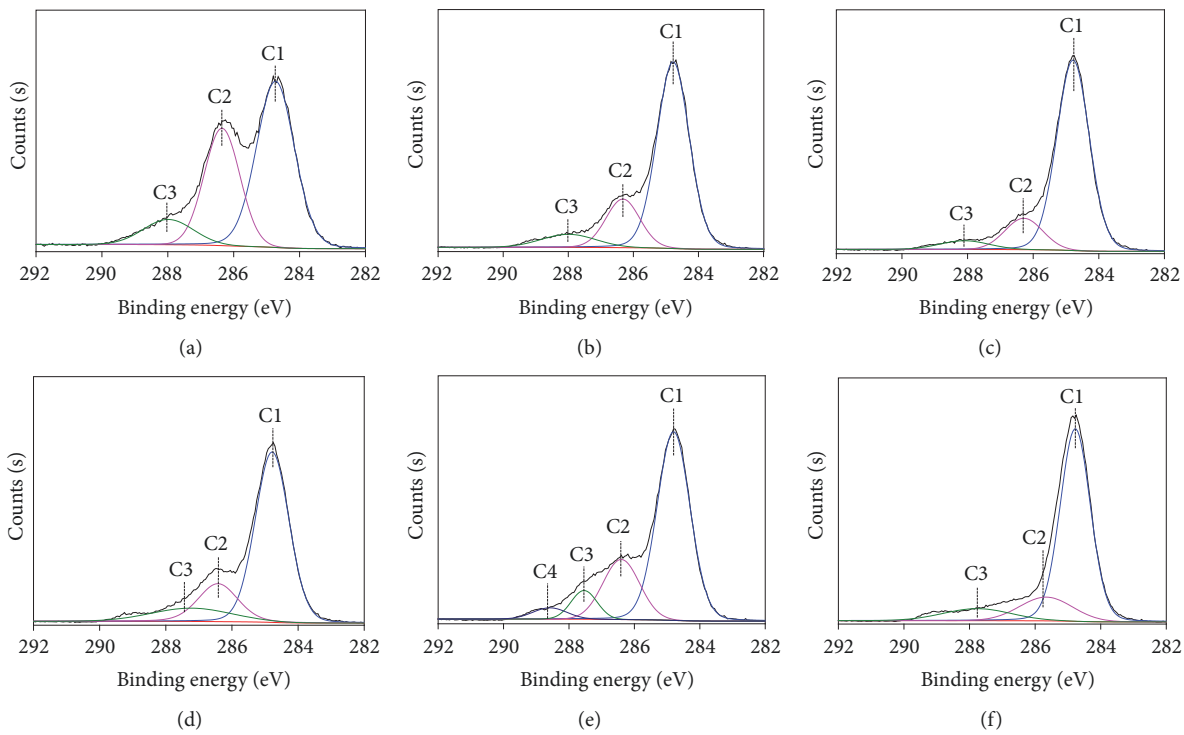

Figure 5: C_{1s} peak spectra of bamboo, BS, HBS, and their coated samples. (a) Bamboo; (b) BS; (c) HBS; (d) PUA coated bamboo; (e) PUA coated BS; (f) PUA coated HBS.

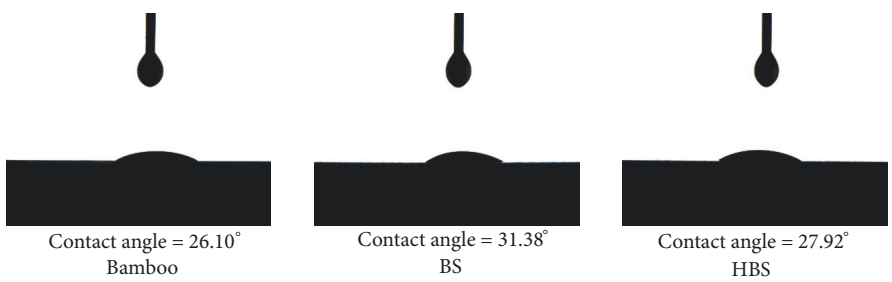

Figure 6: Contact angle of bamboo, BS, and HBS with 70% PUA drop.

significantly and the proportion of C2 decreased. The reason should be that the PF resin, which contained a large amount of C-H, was added into the BS, resulting in the increase of C1 ratio. After heat treatment, the C1 ratio of BS continued to increase, and the C2 ratio decreased, which was attributed to the degradation of the hydroxyl groups by heat treatment [24].

3.3. Contact Angle between PUA and the Substrates. It was known that the contact angle size depends on the hydrophilicity of the substrate and the distribution of the phenolic resin adhesive on the surface of the substrate when coated by the same PUA [25]. Figure 6 showed the contact angle of the PUA droplets (70 wt% solid) on the surface of the three kinds of materials, including bamboo, BS, and HBS. From the figures, the contact angle of PUA on the surface of the BS was the largest of 31.38°, which showed that the compatibility between PUA and BS was poor, and the droplets were difficult to spread on the BS surface. Therefore, the coating film, with poor surface quality, was obtained, due to the resin particle agglomeration and protrusions during the drying process. There was little difference of the contact

Table 3: Elements percentages of bamboo, BS, HBS, and their coated samples.

Sample	Percentage (%)			
	C1	C2	C3	C4
Bamboo	54.82	34.78	10.40	0
BS	72.51	19.35	8.14	0
HBS	80.04	14.63	5.33	0
PUA coated bamboo	68.81	18.96	12.23	0
PUA coated BS	66.09	22.42	7.58	3.91
PUA coated HBS	74.69	15.35	9.96	0

PUA coated bamboo PUA coated BS PUA coated HBS

Figure 7: Images of coated samples after cross-cut test.

angles of PUA droplets on the surface of bamboo and HBS. Therefore, the wetting effect of them was fairly good [26].

3.4. Adhesion of Coating Films. The images of PUA coated bamboo, BS, and HBS after cross-cut tests are shown in Figure 7. It can be seen that the adhesion classification of the PUA coating film of the three types of substrate was all 2. For each coating film, the coating had flaked along the edges and at the intersections of the cuts. A cross-cut area greater than 5%, but not greater than 15%, was affected. Thus, the PUA adhesion of the three types of materials needs to be improved. In the further research, the substrate surface needs to be modified to increase the adhesion of coating film.

4. Conclusions

The coating substrate affected the resulting coating performance of PUA resin due to the different physical and chemical surface properties of the substrate. Bamboo had the fairly good coating performance. However, because of the densified structures and impregnation of phenolic resin, the coating performance of bamboo scrimber by water-based PUA coating was poor. Heat treatment can improve the performance to a certain extent owing to the decreased hydrophilicity and enlarged micropores. The adhesion classifications of the PUA coating film on the three types of substrate were all classification 2. Therefore, the next step was to modify the surface of the substrate or develop a new kind of water-based coating to further improve the coating performance of bamboo scrimber.

Data Availability

The data used to support the findings of this study have not been made available because it is part of a research program of the National Key Research and Development Program of China, and it will be further studied.

Conflicts of Interest

The authors declare that they have no conflicts of interest.

Acknowledgments

This study was financially supported by the National Key Research and Development Program of China (no. 2016YFD0600704) and the National Natural Science Foundation of China (nos. 31870550; 31470591).

References

[1] Y. Xie, G. Xie, and Q. Yao, "Present situation and outlook of bamboo resource utilization in China," *Chinese Journal of Tropical Agriculture*, vol. 6, pp. 46–52, 2004.

[2] J. Cai, L. Zhang, J. Zhou et al., "Multifilament fibers based on dissolution of cellulose in NaOH/urea aqueous solution: structure and properties," *Advanced Materials*, vol. 19, no. 6, pp. 821–825, 2007.

[3] S. Kalia, B. S. Kaith, and I. Kaur, "Pretreatments of natural fibers and their application as reinforcing material in polymer composites—a review," *Polymer Engineering & Science*, vol. 49, no. 7, pp. 1253–1272, 2009.

[4] H. Li and Y. Zhang, "Analysis on ecological architectural material of bamboo," *Building Science*, vol. 8, no. 31, pp. 20–26, 2007.

[5] L. Zou, H. Jin, W. Lu, and X. Li, "Nanoscale structural and mechanical characterization of the cell wall of bamboo fibers," *Materials Science and Engineering C*, vol. 29, pp. 1375–1379, 2008.

[6] F. Meng, R. Liu, Y. Zhang, Y. Huang, Y. Yu, and W. Yu, "Improvement of the water repellency, dimensional stability, and biological resistance of bamboo-based fiber reinforced composites," *Polymer Composites*, vol. 40, no. 2, pp. 506–513, 2017.

[7] Y. Yu, X. Huang, and W. Yu, "A novel process to improve yield and mechanical performance of bamboo fiber reinforced composite via mechanical treatments," *Composites Part B: Engineering*, vol. 56, pp. 48–53, 2014.

[8] S. Amada, Y. Ichikawa, T. Munekata, Y. Nagase, and H. Shimizu, "Fiber texture and mechanical graded structure of bamboo," *Composites Part B: Engineering*, vol. 28, no. 1-2, pp. 13–20, 1997.

[9] I. M. Sulastiningsih and Nurwati, "Physical and mechanical properties of laminated bamboo board," *Journal of Tropical Forest Science*, vol. 21, no. 3, pp. 246–251, 2009.

[10] M. A. Tshabalala, P. Kingshott, M. R. VanLandingham, and D. Plackett, "Surface chemistry and moisture sorption properties of wood coated with multifunctional alkoxysilanes by sol-gel process," *Journal of Applied Polymer Science*, vol. 88, no. 12, pp. 2828–2841, 2003.

[11] Y. Yu, R. Liu, Y. Huang, F. Meng, and W. Yu, "Preparation, physical, mechanical, and interfacial morphological properties of engineered bamboo scrimber," *Construction and Building Materials*, vol. 157, pp. 1032–1039, 2017.

[12] C. Schaller and D. Rogez, "New approaches in wood coating stabilization," *Journal of Coatings Technology and Research (JCTR)*, vol. 4, no. 4, pp. 401–409, 2007.

[13] M. Frigione and M. Lettieri, "Novel attribute of organic-inorganic hybrid coatings for protection and preservation of materials (stone and wood) belonging to cultural heritage," *Coatings*, vol. 8, p. 319, 2018.

[14] C. Li, H. Xiao, X. Wang, and T. Zhao, "Development of green waterborne UV-curable vegetable oil-based urethane acrylate pigment prints adhesive: preparation and application," *Journal of Cleaner Production*, vol. 180, pp. 272–279, 2018.

[15] E. Liptáková, J. Kúdela, and J. Sarvaš, "Study of the system wood - coating material. I. Wood - liquid coating material," *Holzforschung*, vol. 2, pp. 189–196, 2000.

[16] L. Long, J. Xu, X. Wan, and L. Qian, "Surface modification of nano-alumina and its application in preparing polyacrylate water-based wood coating," *Journal of Polymer Engineering*, vol. 33, no. 8, pp. 767–774, 2013.

[17] C. Queant, P. Blanchet, V. Landry, and D. Schorr, "Effect of adding UV absorbers embedded in carbonate calcium templates covered with light responsive polymer into a clear wood coating," *Coatings*, vol. 8, p. 265, 2018.

[18] Y. Zhang, W. Yu, and Y. Zhang, "Effect of steam heating on the color and chemical properties of neosinocalamus affinis bamboo," *Journal of Wood Chemistry and Technology*, vol. 33, no. 4, pp. 235–246, 2013.

[19] Y. M. Zhang, Y. L. Yu, and W. J. Yu, "Effect of thermal treatment on the physical and mechanical properties of phyllostachys pubescen bamboo," *European Journal of Wood and Wood Products*, vol. 71, no. 1, pp. 61–67, 2013.

[20] Y. Yu, R. Zhu, B. Wu, Y. Hu, and W. Yu, "Fabrication, material properties, andapplication of bamboo scrimber," *Wood Science and Technology*, vol. 49, pp. 83–98, 2015.

[21] J. Xu, H. Wu, R. Liu, L. Long, and P. Lin, "Preparation and properties of light-resistant printing UV ink modified with nano-TiO_2 on wood substrate," *Surface Engineering*, pp. 1–8, 2018.

[22] M. Mahdavi, P. L. Clouston, and S. R. Arwade, "A low-technology approach toward fabrication of laminated bamboo lumber," *Construction and Building Materials*, vol. 29, pp. 257–262, 2012.

[23] J. Gironès, J. A. Méndez, S. Boufi, F. Vilaseca, and P. Mutjé, "Effect of silane coupling agents on the properties of pine fibers/polypropylene composites," *Journal of Applied Polymer Science*, vol. 103, no. 6, pp. 3706–3717, 2007.

[24] D. Kocaefe, X. Huang, Y. Kocaefe, and Y. Boluk, "Quantitative characterization of chemical degradation of heat-treated wood surfaces during artificial weathering using XPS," *Surface and Interface Analysis*, vol. 45, no. 2, pp. 639–649, 2013.

[25] S. Zhao, Z. Wang, and H. Kang, "Fully bio-based soybean adhesive in situ cross-linked by interactive network skeleton from plant oil-anchored fiber," *Industrial Crops and Products*, vol. 122, pp. 366–374, 2018.

[26] M. Scheikl and M. Dunky, "Measurement of dynamic and staue contact angles on wood for the determination of its surface tension and the penetration of liquids into the wood surface," *Holzforschung*, vol. 52, no. 1, pp. 89–94, 1998.

Hindawi
Advances in Polymer Technology
Volume 2019, Article ID 8698746, 8 pages
https://doi.org/10.1155/2019/8698746

Research Article

Effect of Iron Oxide on the Protective Photochromism of African Padauk

Chen Wang, Ye Qin, Fang Wang, Zhiping Wang, and Anmin Huang

Research Institute of Wood Industry, Chinese Academy of Forestry, Xiangshan Road 2, Haidian 100091, Beijing, China

Correspondence should be addressed to Anmin Huang; hbham2000@sina.com

Received 10 December 2018; Revised 3 January 2019; Accepted 17 January 2019; Published 3 March 2019

Guest Editor: Changlei Xia

African padauk is a tree whose wood is an excellent material for producing decorative items. The wood is susceptible to sunlight exposure and degrades severely, even after short exposures, which leads to discoloration. Ultraviolet irradiation is the main factor that produces discoloration. In this study, chemical changes occurring on the wood surfaces were analyzed by Fourier transform infrared spectroscopy. The discoloration of the African padauk was mainly because of the photodegradation of lignin and extractives by ultraviolet radiation. Additionally, the inhibitory effect of different concentrations of red iron oxide coating was investigated. The results revealed that the chromatism $\Delta E*$ was considerably reduced with the protection of iron oxide. However, the inhibition of the discoloration rate of the specimens covered with a film of red iron oxide increased with values reaching approximately 80%. The red iron oxide coating had a strong inhibitory effect on the discoloration of the African padauk.

1. Introduction

Wood color is an important quality indicator for end users, especially for interior items, such as flooring and furniture. However, the wood color tends to change when exposed to the environment. Usually, wood discoloration is caused by a variety of environmental factors, including sunlight, moisture, and temperature. Among these factors, ultraviolet (UV) light, a component of sunlight, plays the most important role in the discoloration process by inducing photodegradation in wood [1–3]. Because of the decrease in aromatic structures and increase in carbonyl groups, photodegradation of wood eventually results in discoloration on the wood surface [4–6].

African padauk is a hardwood tree species of the genus *Pterocarpus* in the Fabaceae family and is native to tropical areas in Africa. It has a relatively high extractives content and mainly contains homopterocarpin, pterocarpin, and 4-t-butyl-2-(4-nitrophenyl) phenol [7]. These compounds give the African padauk its appealing color. In general, this wood is both stable and durable, which makes it a suitable raw material for interior decoration applications. With the decrease in rosewood resources, the value of African padauk is increasing. Previous studies have shown that African padauk is more prone to degradation under sunlight exposure [8, 9]. Photodegradation causes the color to change initially to red and eventually to brown. Uneven discoloration greatly reduces the reliability and value of African padauk in practical applications. Although many researchers have studied the wood photodiscoloration process [10], studies on the discoloration of African padauk are scarce. A better understanding of the discoloration mechanism of African padauk is needed to determine the appropriate measures for its protection.

The cell wall of wood consists mainly of cellulose, hemicellulose, lignin, and extractive components. Lignin and extractives are more susceptible to light than the other two major components [11, 12]. When lignin is irradiated, the carbonyl, phenolic hydroxyl, and methoxy groups in the lignin with benzene rings form free radicals. The free radicals undergo a photooxidation reaction and generate chromophoric carbonyl and carboxyl groups, which are responsible for wood discoloration. Photooxidative degradation of lignin only occurs in the surface layer of wood. Extractives also play a critical role in the photodegradation of wood. Some researchers believe that extractives are involved in wood discoloration, such as the photodegradation of

polyphenolic substances [13, 14], while others maintain that extractives act as antioxidants to protect the wood against photodegradation [15–17]. Earlier results have indicated that the formation of chromophoric groups, such as C=C and C=O, during the photooxidation process is a major cause of wood discoloration. Variations in the chemical characteristics of the wood surface after irradiation can be detected by means of Fourier transform infrared (FT-IR) spectroscopic analysis [18–20].

Wood photochromism usually occurs on the surface. Different techniques have been developed to address this problem and reduce the photodegradation of wood, including chemical modification, surface coatings, and other methods [21, 22]. Surface coatings are the most convenient and commonly used method, which can form a protective layer by adding the right amount of UV screeners in the coating [23]. Coating systems for protecting the wood from discoloration, including organic UV absorbers and hindered amine light stabilizers, have traditionally not been used for long-term protection. In recent years, inorganic UV absorbers have attracted attention as an alternative treatment for protecting wood surfaces against UV radiation [24, 25]. Adding the nanoparticles TiO_2, ZnO, and SiO_2 to acrylic resin coatings can also have an effect on the shielding of UV radiation [26–28]. However, nanoparticles easily aggregate and weaken the ability to scatter UV light. Additionally, the cost of a nanocoating is higher and the process still remains in the research stage.

Iron oxide pigments as an inorganic UV absorber can prevent light irradiation from reaching wood surfaces and the initiation of free radical reactions, thus providing protection against discoloration. Schauwecker's research shows that particle size of iron oxide and protective effect of wood present the correlation [29]. Moreover, low concentrations of iron oxides have also shown promise as wood surface protection agents, reducing lignin loss and discoloration [30]. Zhang et al. added four kinds of iron oxide pigments into wood-fiber/high-density-polyethylene composites; the experimental results show that the iron oxide red and black performed better than the other two pigments in protection of wood color and mechanical properties [31]

In general, because of similar color of African padauk, the red iron oxide is suitable for surface finishing of African padauk. This study investigated the mechanism of discoloration and the effect of red iron oxide on the discoloration of African padauk. As a tropical hardwood, it is conceivable that the extractives of African padauk may play an important role in discoloration. Fourier transform infrared spectroscopy was used to analyze the variation in the chemical characteristics of the specimen surfaces after irradiation. Different concentrations of red iron oxide were used to examine the color change after irradiation.

2. Experimental

2.1. Materials. The logs of African padauk were purchased from Power Dekor (Danyang, China); details are listed in Table 1. The logs were obtained from mature wood above breast height without any cracking, decay, discoloration, or other defects. The red iron oxide was purchased from Tianjin North Coating Co., Ltd. (Tianjin, China), and the basic pieces of information are showed in Table 2.

Table 1: Essential parameters of African padauk.

Wood	African padauk
Scientific name	*Pterocarpus soyauxii*
Density	0.79 g cm^{-3}
Place of origin	Republic of Congo
Water content	8 %
Sample size	75 mm(L) × 50 mm(R) × 4 mm(T)

Table 2: Basic information of the red iron oxide.

Property	Transparent Red Iron Oxide
Molecular formula	α-Fe_2O_3
Molecular weight	159.69 g/mol
Appearance	Red powder
Melting point	1565°C
Boiling point	3414°C
Iron content	≥ 95% (m/m)
105°C Volatiles	≤ 1% (m/m)
Hydrotrope	≤ 0.3% (m/m)
Paste content	50%
Particle size	0.4 μm ~ 20 μm

2.2. Methods

2.2.1. Specimen Coating. The oxide was provided with a special megilp solvent. All of the specimens were polished with sandpaper (400 P) prior to the experiment and stored in a dark environment. To determine the influence on the original color of the African padauk, 3%, 6%, 9%, 12%, and 15% red iron oxide solutions were prepared and tested. The red iron oxide concentration was calculated according to

$$\mathscr{W} = \frac{m_1}{m_1 + m_2} \times 100\% \quad (1)$$

where W, m_1, and m_2 are the concentration of the red iron oxide (%), a mass of the red iron oxide (g), and mass of the megilp (g), respectively.

The specimens were coated using a brushing method and then air-dried. The coating weight was 0.2 g ± 0.01g, which was calculated according to

$$\Delta m = m_4 - m_3 \quad (2)$$

where m_3 is the mass of the specimens before coating with red iron oxide (g) and m_4 is the mass after coating with red iron oxide (g).

2.2.2. Color Measurement. There are three samples in each group. The specimens were separately exposed to natural and artificial UV light. Half of each specimen surface was covered with aluminium foil prior to exposure so that the difference between the exposed and original surface was clearly visible.

Natural weathering was achieved in the absence of wind and rain. Artificial weathering was conducted in an accelerated UV radiation chamber (LX-8509, Dongguan Lixin Instruments Co. Ltd., Dongguan, China) equipped with two UVA-340 lamps with a radiation intensity of 30 W/m^2, which provided a simulation of sunlight radiation in the short wavelength region of 290 nm to 400 nm.

The L∗, a∗, b∗, and ΔE∗ parameters were measured by a chromatic aberration meter (CR-300, Minolta Co., Osaka, Japan) at five places on each specimen. The average values were subsequently calculated. Each specimen was tested three times and the average of those values was recorded. The initial color measurement was determined prior to any light irradiation. The intermediary color measurements were performed after 2 d, 4 d, 8 d, 12 d, 20 d, 40 d, 60 d, and 80 d of natural sunlight exposure and 8 h, 16 h, 32 h, 56 h, 80 h, 104 h, and 128 h of UV light exposure.

The overall discoloration of the surface was established by the color deviation ΔE∗, which was calculated using the following formula:

$$\Delta E^* = \sqrt{\left[(\Delta L^*)^2 + (\Delta a^*)^2 + (\Delta b^*)^2\right]} \quad (3)$$

where $\Delta L*$, $\Delta a*$, and $\Delta b*$ are the differences between the original and final coordinates (before and after exposure).

2.2.3. FT-IR Spectroscopic Analysis. The specimens were exposed to natural sunlight and artificial UV light until their color stabilized. The powder was obtained using a crusher (BJ-300A, Deqing BaiJie Electrical Appliance Co. Ltd., Deqing, China). The discolored powder was obtained by scraping the wood surface with a knife. For extraction of the solid wood, the specimens were soaked in a mixture of ethanol-benzene (1:2 ratio) for 6 h in a Soxhlet apparatus, followed by extraction in pure ethanol for 4 h. The specimens were then oven-dried at 103°C until the weight was constant. Two milligrams of each specimen were blended with 100 mg of KBr powder, ground again, and pressed into tablets. FTIR analyses were carried out at room temperature according to the methodology described by NICOLET 6700, using a Spectrum 2000 FTIR (Thermo Fisher Scientific, Massachusetts, USA) with a universal attenuated total reflectance (UATR) accessory. Potassium bromide (KBr) was used to collect background spectra. Air-dried sample powders were mixed with KBr at a weight ratio of 1:100 before spectrum collection. Ten scans were carried out for each sample in a spectral range from 400 to 4000 cm^{-1} at a resolution of 4 cm^{-1}.

3. Results and Discussion

3.1. FT-IR Analysis. The FT-IR spectra of the African padauk before and after irradiation are presented in Figure 1. The spectra showed that the intensity of the absorption peak at 1731 cm^{-1}, assigned to carbonyl group stretching [32, 33], increased after irradiation, whereas the intensities of the lignin absorption peaks at 1510 cm^{-1}, 1462 cm^{-1}, 1267 cm^{-1}, and 1230 cm^{-1} decreased after irradiation [34]. These results indicated the generation of chromophoric carbonyl groups and degradation of lignin on the wood surface after irradiation. As was demonstrated by previous research results, carbonyl and phenoxyl free radicals in the lignin underwent demethoxylation by absorbing the UV light and formed chromophoric groups. As a result, the intensity of the absorbance by lignin at 1510 cm^{-1} decreased, while the carbonyl group intensity at 1731 cm^{-1} increased because of lignin photodegradation.

To gain a better insight into the wood photodegradation process after irradiation, the relative peak height ratios were compared between the extracted and nonextracted African padauk specimens. The results are shown in Figure 2. The peaks at 1370 cm^{-1}, 1158 cm^{-1}, and 898 cm^{-1} were mainly from cellulose and had no remarkable effect on the photodegradation of wood. The 1510 cm^{-1}/1370 cm^{-1} and 1731 cm^{-1}/1370 cm^{-1} ratios were calculated for all of the extracted and nonextracted wood specimens.

The 1510 cm^{-1}/1370 cm^{-1} ratios (absorption by lignin) for the nonextracted and extracted African padauk specimens before irradiation also exhibited some differences. The ratio of the extracted African padauk specimen was 0.98, which was lower than that of the nonextracted specimen (1.23). The reason for this was that the main components of the extractives were phenolic compounds, and thus the ratio decreased when the extractives were removed.

Regardless of whether it was a nonextracted or extracted African padauk specimen, the 1510 cm^{-1}/1370 cm^{-1} ratio (absorption by lignin) was reduced after irradiation, which indicated that lignin underwent photodegradation during irradiation. Also, the 1510 cm^{-1}/1370 cm^{-1} ratio of the nonextracted African padauk specimens was higher than that of the extracted specimens. Thus, the presence of extractives accelerated the photodegradation process of lignin when exposed to sunlight.

The 1731 cm^{-1}/1370 cm^{-1} ratio (carbonyl groups) of the nonextracted and extracted African padauk specimens increased after irradiation. This indicated that the photodegradation of lignin produced carbonyl groups. Furthermore, the carbonyl groups formation rate in the 1731 cm^{-1}/1370 cm^{-1} ratio of the nonextracted African padauk was higher than that of the extracted specimens. Accordingly, the presence of extractives might have led to the formation of more carbonyl groups after irradiation. This phenomenon was explained by the presence of phenolic extractives. Extractives can absorb light and undergo a photochemical change. Photodegradation of the phenolic compounds in the extractives may also have generated carbonyl groups because of the degradation of lignin.

3.2. Color Change during Exposure. The overall color difference (ΔE∗) of the specimens after exposure to natural sunlight is shown in Figure 3. The specimens S1-SU, S2-SU, and S3-SU were three duplicate African padauk that were exposed to sunlight. The results in Figure 3 revealed that the change trend of the overall ΔE∗ was consistent as the irradiation time increased. Rapid discoloration was observed at the beginning of sunlight irradiation and then discoloration slowed down. During the first 20 d of sunlight irradiation, the ΔE∗ value of the African padauk exhibited a

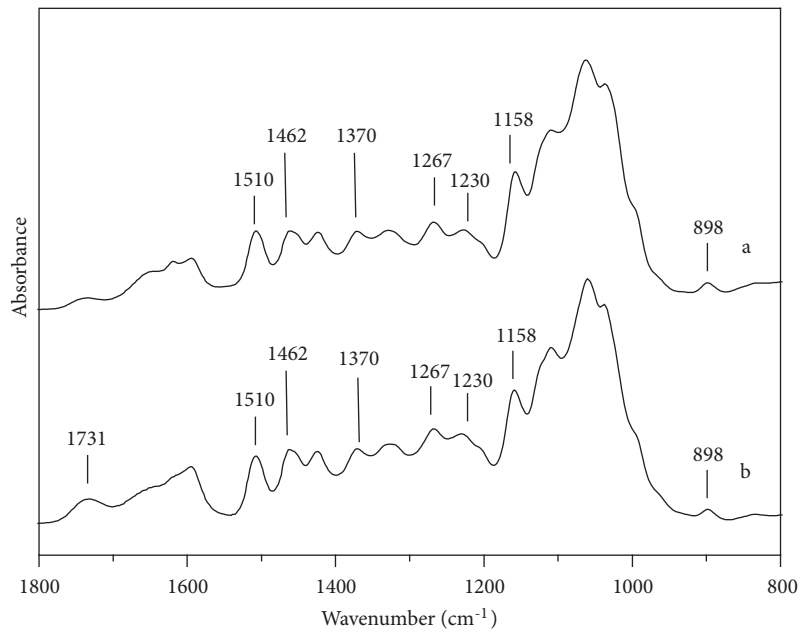

Figure 1: FT-IR spectra of the African padauk (a) before and (b) after irradiation.

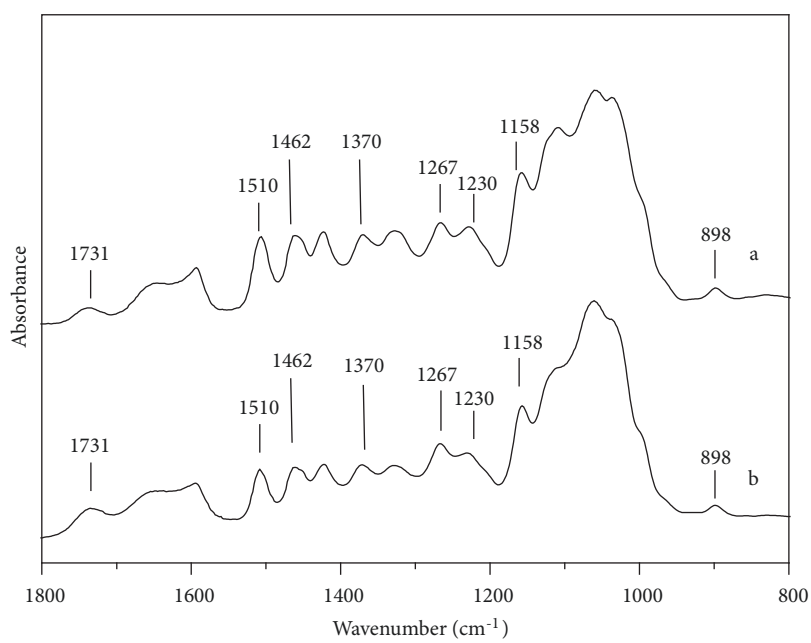

Figure 2: FT-IR spectra of the wood powder after extraction of African padauk (a) before and (b) after natural sunlight exposure.

great and remarkable color difference and soon reached 28. With an increased irradiation time, the ΔE∗ value increased a little and remained at approximately 30 after 80 d.

Because of uncontrollable factors in natural sunlight, an accelerated lightfastness test was performed. The ΔE∗ values of the specimens during the UV radiation process were calculated and are shown in Figure 4. The specimens S1-UV, S2-UV, and S3-UV were three duplicate specimens of African padauk that underwent UV irradiation. With an increase in the irradiation time, the overall ΔE∗ values of S1-UV, S2-UV, and S3-UV increased gradually with a similar trend. During the first 32 h of UV irradiation, the ΔE∗ values increased rapidly and soon reached approximately 25. After 32 h of UV irradiation, the value of ΔE∗ tended to level off and ultimately remained at approximately 30 after 128 h of UV irradiation. This confirmed that UV radiation is one of the most important environmental factors that cause severe wood surface discoloration.

3.3. Inhibitory Effect of the Red Iron Oxide Coating on Wood Discoloration. The discoloration of the African padauk was mainly caused by UV light degradation. To investigate the

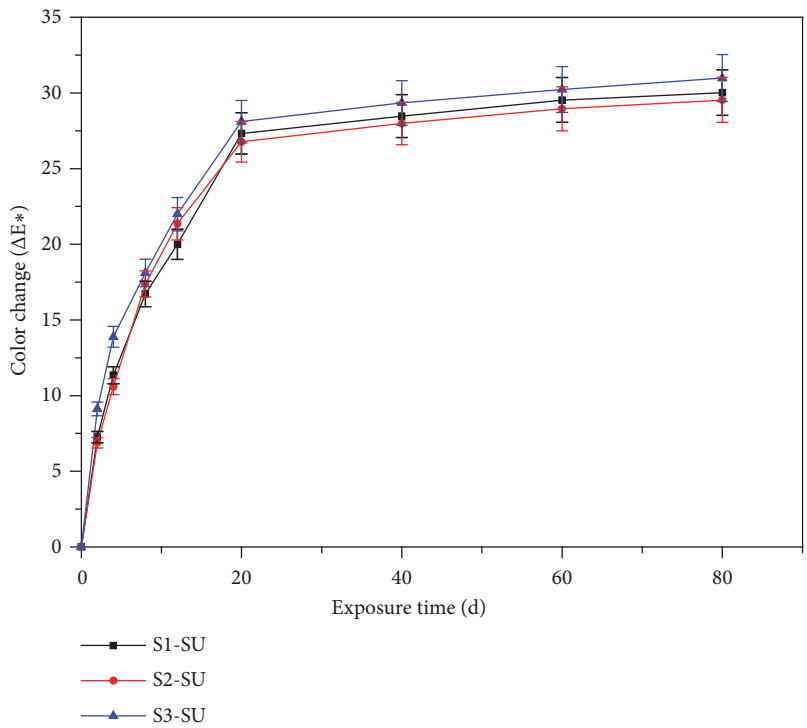

Figure 3: Color change of the African padauk after being exposed to natural sunlight.

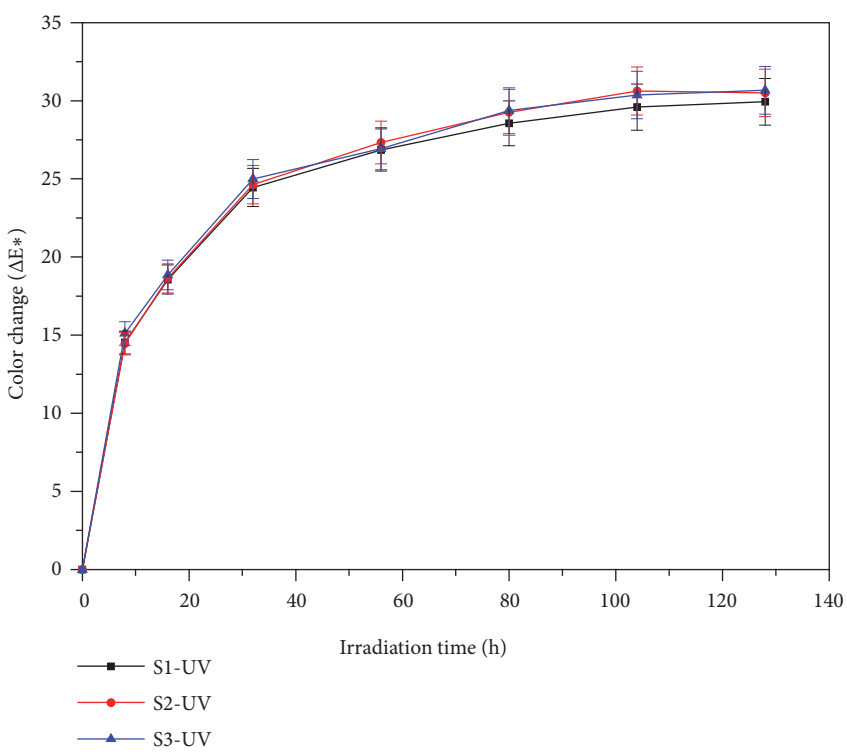

Figure 4: Color change of the African padauk after being exposed to UV radiation.

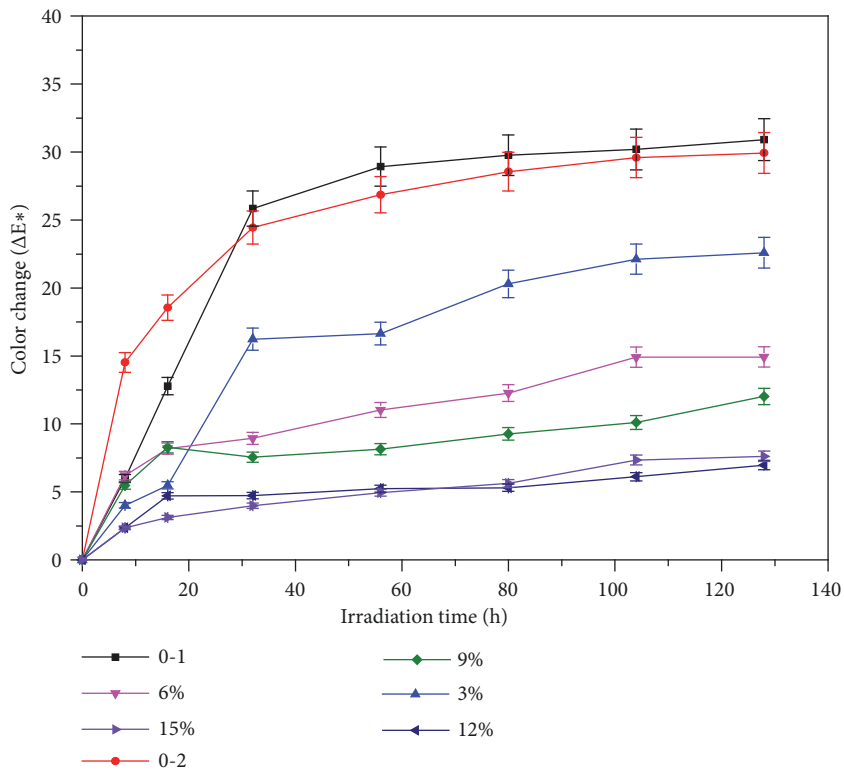

Figure 5: ΔE∗ changes of 3% to 15% concentration of red iron oxide coated specimens in the UV exposure condition.

influence of the red iron oxide coating on the color change of the African padauk, different red iron oxide concentrations were evaluated. The extensive experiments showed that a concentration of red iron oxide less than 15% had little effect on the initial color change of the African padauk. The results in Figure 5 revealed that all of the different red iron oxide concentrations had varying degrees of protective effect. The 0-1 group represented the untreated African padauk and the 0-2 group represented the African padauk with 0.2 g of megilp. With an increase in the irradiation time, all of the overall ΔE∗ values exhibited an increasing trend. In the 0-1 and 0-2 groups, the color change trend was almost the same. The ΔE∗ values increased rapidly to approximately 25 during the first 32 h of UV irradiation and then reached approximately 30 after 132 h of UV irradiation, which revealed that the solvent had no effect on preventing surface discoloration of the African padauk caused by UV light. However, as the red iron oxide concentration increased, the ΔE∗ values decreased gradually. These results showed that when the red iron oxide concentration was higher, the ΔE∗ values were lower. Compared with the 3%, 6%, and 9% red iron oxide concentrations, the ΔE∗ appeared to be smaller and more stable with the 12% and 15% concentrations. The ΔE∗ values were approximately 7 after 132 h of UV irradiation. Thus, these results showed that red iron oxide has a positive effect on preventing discoloration of African padauk.

To more clearly show the effect of red iron oxide on preventing UV light-induced discoloration, the inhibition ratio parameter was introduced. The results that are presented in Figure 6 revealed that all of the different red iron oxide concentrations showed some degree of inhibitory effect on discoloration. Specifically, when the red iron oxide concentration was 3%, the inhibition ratio sharply declined and remained at approximately 30%. When the red iron oxide concentration was 6% to 15%, the trend remained consistent. The photochromic inhibition rate remained relatively stable during the first 32 h of exposure to UV radiation and slightly decreased after that point. Moreover, when the red iron oxide concentrations were 12% and 15%, the inhibition ratio was higher than that of the other concentrations and reached approximately 80. These findings demonstrated that the photochromic inhibitory effect was superior when the concentration of red iron oxide was 12% to 15%, which was consistent with the results that are shown in Figure 5.

4. Conclusions

Ultraviolet light is the main cause of wood discoloration. Rapid color changes in the samples took place in the beginning of radiation exposure and the ΔE∗ value ultimately reached approximately 30 for both natural and artificial UV light. Discoloration occurred along with fading of the African padauk and degradation of the wood compositions. The FT-IR spectroscopic analysis of the African padauk demonstrated that the changes in the chemical characteristics occurred after irradiation. The photodegradation of the lignin and extractives resulted in the formation of chromophoric carbonyl groups. As the extractives contain large amounts of

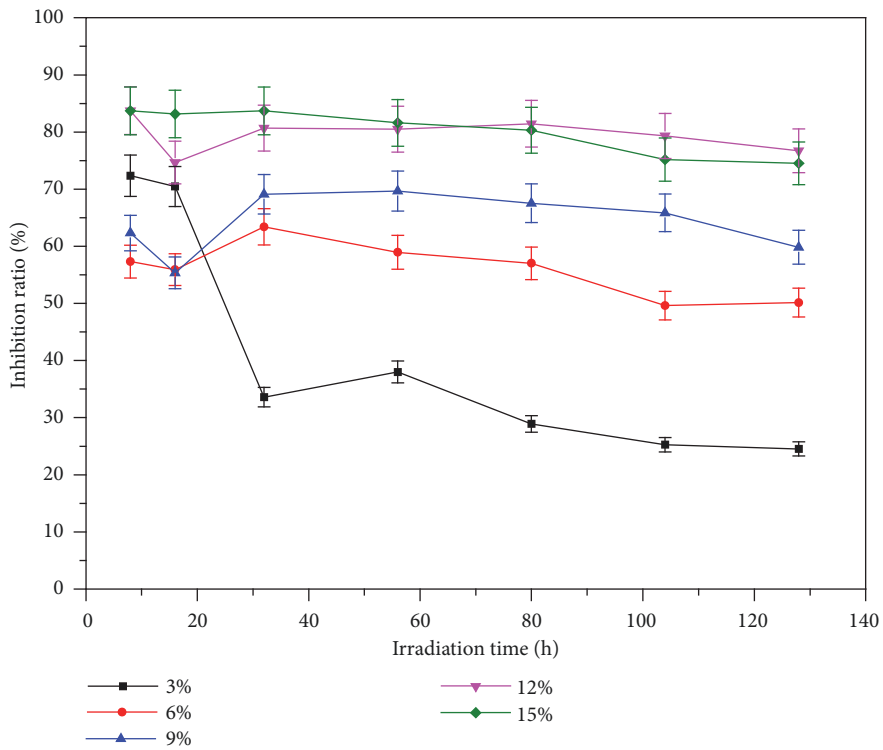

Figure 6: Inhibition ratio changes of 3% to 15% concentrations of red iron oxide coated specimens in the UV exposure condition.

phenolic compounds, the presence of extractives accelerated the photodegradation of lignin. The degree of discoloration of the African padauk was greatly influenced by the red iron oxide concentration.

The $\Delta E*$ remained at approximately 7 after 128 h of UV irradiation with the tested red iron oxide concentrations of 12% and 15%. The inhibition ratio in the specimens was also higher with the tested concentrations of 12% and 15% than the concentrations of 3% to 9%. The highest inhibition ratio in the specimens reached approximately 80% when the red iron oxide concentration was 12% and 15%. This was sufficient to prevent discoloration of the African padauk by covering them with a film of red iron oxide and showed an excellent light inhibitory performance.

However, because of the low price and outstanding property of photoprotection, red iron oxide has great potential in wood protection. Until now iron oxide properties have not been fully investigated in conjunction with wood surfaces and this will become a focus of future study.

Data Availability

The datasets used or analyzed during the current study are available from the corresponding author on reasonable request.

Conflicts of Interest

The authors declare no conflicts of interest.

Authors' Contributions

Chen Wang and Ye Qin performed the experiments, analyzed the data, and wrote the manuscript; Fang Wang and Anmin Huang conceived and designed the experiments; Zhiping Wang contributed to the materials and analysis tools.

Acknowledgments

This research was funded by National Natural Science Foundation of China (Grant no. 31670564) and Technological Innovation Strategic Alliance–Based on the Wood and Bamboo Industry (Grant no. TIAWBI201809).

References

[1] J. Baar and G. Vladimír, "The Analysis of Tropical Wood Discoloration Caused by Simulated Sunlight," *European Journal of Wood and Wood Products*, vol. 70, no. 1-3, pp. 263–269, 2012.

[2] Y. Liu, L. Shao, J. Gao et al., "Surface Photo-Discoloration And Degradation of Dyed Wood Veneer Exposed to Different Wavelengths of Artificial Light," *Applied Surface Science*, vol. 331, pp. 353–361, 2015.

[3] Y. Ouadou, D. Aliouche, M.-F. Thevenon et al., "Characterization and Photodegradation Mechanism of Three Algerian Wood Species," *Journal of Wood Science*, vol. 63, no. 1938, pp. 1–7, 2017.

[4] Y. Wu, C. Xia, L. Cai et al., "Development of Natural Fiber-Reinforced Composite with Comparable Mechanical Properties And Reduced Energy Consumption And Environmental

Impacts for Replacing Automotive Glass-Fiber Sheet Molding Compound," *Journal of Cleaner Production*, vol. 184, pp. 92–100, 2018.

[5] F. Ishiguri, S. Maruyama, K. Takahashi et al., "Extractives Relating to Heartwood Color Changes in Sugi (Cryptomeria Japonica) by A Combination of Smoke-Heating And UV Radiation Exposure," *Journal of Wood Science*, vol. 49, no. 2, pp. 135–139, 2003.

[6] L. Oltean, A. Teischinger, and C. Hansmann, "Wood Surface Discolouration Due to Simulated Indoor Sunlight Exposure," *Holz als Roh - und Werkstoff*, vol. 66, no. 1, pp. 51–56, 2007.

[7] J.-B. T. Saha, D. Abia, S. Dumarçay et al., "Antioxidant Activities, Total Phenolic Contents And Chemical Compositions of Extracts from Four Cameroonian Woods: Padouk (Pterocarpus Soyauxii Taubb), Tali (Erythrophleum Suaveolens), Moabi (Baillonella Toxisperma), And Movingui (Distemonanthus Benthamianus)," *Industrial Crops and Products*, vol. 41, no. 1, pp. 71–77, 2013.

[8] J. Baar, R. Wimmer, and S. D'Amico, "Dependence of Colour And Discolouration on Total Extractive Content of African Padauk And Jatoba," *Wood and Science Technology*, vol. 48, no. 6, pp. 1155–1165, 2014.

[9] J. Baar, S. D'Amico, and R. Wimmer, "Color and Light-Induced Discoloration of Wood from the Tropical Species Jatoba and African Padauk," *ProLigno*, vol. 9, no. 4, pp. 581–586, 2013.

[10] B. Iris, N. Amusant, K. Minato, and et al., "Effect of Extractives on Vibrational Properties of African Padauk (Pterocarpus Soyauxii Taub.)," *Wood and Science Technology*, vol. 45, no. 3, pp. 461–472, 2011.

[11] C. Xia, J. Yu, S. Q. Shi et al., "Natural Fiber And Aluminum Sheet Hybrid Composites for High Electromagnetic Interference Shielding Performance," *Composites Part B: Engineering*, vol. 114, pp. 121–127, 2017.

[12] Y. Peng, R. Liu, J. Cao, and Y. Chen, "Effects of UV Weathering on Surface Properties of Polypropylene Composites Reinforced with Wood Flour, Lignin, And Cellulose," *Applied Surface Science*, vol. 317, pp. 385–392, 2014.

[13] P. Nzokou and D. P. Kamdem, "Influence of Wood Extractives on The Photo-Discoloration of Wood Surfaces Exposed to Artificial Weathering," *Color Research & Application*, vol. 31, no. 5, pp. 425–434, 2010.

[14] T.-C. Chang, H.-T. Chang, C.-L. Wu et al., "Influences of Extractives on The Photodegradation of Wood," *Polymer Degradation and Stability*, vol. 95, no. 4, pp. 516–521, 2010.

[15] N. Gierlinger, D. Jacques, M. Grabner et al., "Colour of Larch Heartwood And Relationships to Extractives And Brown-Rot Decay Resistance," *Trees - Structure and Function*, vol. 18, no. 1, pp. 102–108, 2004.

[16] K. K. Pandey, "A Note on The Influence of Extractives on The Photo-Discoloration And Photo-Degradation of Wood," *Polymer Degradation and Stability*, vol. 87, no. 2, pp. 375–379, 2005.

[17] T.-C. Chang, H.-T. Chang, C.-L. Wu et al., "Stabilizing Effect of Extractives on The Photo-Oxidation of Acacia Confusa Wood," *Polymer Degradation and Stability*, vol. 95, no. 9, pp. 1518–1522, 2010.

[18] B. A. Horn, J. Qiu, N. L. Owen, and W. C. Feist, "FT-IR Studies of Weathering Effects in Western Redcedar and Southern Pine," *Applied Spectroscopy*, vol. 48, no. 6, pp. 662–668, 1994.

[19] M. Uwe, R. Manfred, M. Schwanninger et al., "Yellowing and IR-Changes of Spruce Wood as Result of UV-Irradiation," *Journal of Photochemistry & Photobiology*, vol. 69, no. 2, pp. 97–105, 2003.

[20] T. C. M. Pastore, K. O. Santos, and J. C. Rubim, "A Spectrocolorimetric Study on The Effect of Ultraviolet Irradiation of Four Tropical Hardwoods," *Bioresource Technology*, vol. 93, no. 1, pp. 37–42, 2004.

[21] P. D. Evans, A. J. Michell, and K. J. Schmalzl, "Studies of The Degradation And Protection of Wood Surfaces," *Wood and Science Technology*, vol. 26, no. 2, pp. 151–163, 1992.

[22] J. Liu and T. Furuno, "The Fractal Estimation of Wood Color Variation by The Triangular Prism Surface Area Method," *Wood and Science Technology*, vol. 36, no. 5, pp. 385–397, 2002.

[23] P.-L. Chou, H.-T. Chang, T.-F. Yeh, and S.-T. Chang, "Characterizing The Conservation Effect of Clear Coatings on Photodegradation of Wood," *Bioresource Technology*, vol. 99, no. 5, pp. 1073–1079, 2008.

[24] P. Hayoz, W. Peter, and D. Rogez, "A New Innovative Stabilization Method for The Protection of Natural Wood," *Progress in Organic Coatings*, vol. 48, no. 2, pp. 297–309, 2003.

[25] B. Forsthuber, C. Schaller, and G. Grüll, "Evaluation of The Photo Stabilising Efficiency of Clear Coatings Comprising Organic UV Absorbers And Mineral UV Screeners on Wood Surfaces," *Wood and Science Technology*, vol. 47, no. 2, pp. 281–297, 2013.

[26] N. Auclair, B. Riedl, V. Blanchard, and P. Blanchet, "Improvement of Photoprotection of Wood Coatings by Using Inorganic Nanoparticles as Ultraviolet Absorbers," *Forest Products Journal*, vol. 61, no. 1, pp. 20–27, 2011.

[27] Y. Fu, W. Fu, Y. Liu et al., "Comparison of ZnO Nanorod Array Coatings on Wood And Their UV Prevention Effects Obtained by Microwave-Assisted Hydrothermal And Conventional Hydrothermal Synthesis," *Holzforschung*, vol. 69, no. 8, 2015.

[28] H. Guo, P. Fuchs, E. Cabane et al., "UV-Protection of Wood Surfaces by Controlled Morphology Fine-Tuning of ZnO Nanostructures," *Holzforschung*, vol. 70, no. 8, 2016.

[29] C. F. Schauwecker, A. G. McDonald, A. F. Preston et al., "Use of Iron Oxides to Influence The Weathering Characteristics of Wood Surfaces: A Systematic Survey of Particle Size, Crystal Shape And Concentration," *European Journal of Wood and Wood Products*, vol. 72, no. 5, pp. 669–680, 2014.

[30] F. Christoph, G. Armando, and J. Jeff, "Performance of Wood Treated with Prospective Organic Surface Protectants upon Outdoor Exposure: FTIR Spectroscopic Analysis of Weathered Surfaces," *Holzforschung*, vol. 67, no. 2, pp. 227–235, 2013.

[31] Z.-M. Zhang, H. Du, W.-H. Wang et al., "Property Changes of Wood-Fiber/HDPE Composites Colored by Iron Oxide Pigments after Accelerated UV Weathering," *Journal of Forestry Research*, vol. 21, no. 1, pp. 59–62, 2010.

[32] S. Zhao, Z. Wang, H. Kang et al., "Fully Bio-Based Soybean Adhesive in Situ Cross-Linked by Interactive Network Skeleton from Plant Oil-Anchored Fiber," *Industrial Crops and Products*, vol. 122, pp. 366–374, 2018.

[33] S. Zhao, Z. Wang, H. Kang et al., "Construction of bioinspired organic-inorganic hybrid composite by cellulose-induced interfacial gelation assisted with Pickering emulsion template," *Chemical Engineering Journal*, vol. 359, pp. 275–284, 2019.

[34] Z. Wang, S. Zhao, H. Kang et al., "Reduction of Energy Consumption of Green Plywood Production by Implementing High-Efficiency Thermal Conductive Bio-Adhesive: Assessment from Pilot-Scaled Application," *Journal of Cleaner Production*, vol. 210, pp. 1366–1375, 2019.